RIJKSUNIVERSITEIT GRONINGEN

Sensitive Polarimetry in a Search for the Deuteron Electric Dipole Moment

Proefschrift

ter verkrijging van het doctoraat in de
Wiskunde en Natuurwetenschappen
aan de Rijksuniversiteit Groningen
op gezag van de
Rector Magnificus, dr. F. Zwarts,
in het openbaar te verdedigen op
vrijdag 19 februari 2010
om 13:15 uur

door

Marléne da Silva e Silva

geboren op 3 mei 1982
te Porto, Portugal

Promotor:	Prof. dr. K. Jungmann
Copromotor:	Dr. Ir. C.J.G. Onderwater
Beoordelingscommissie:	Prof. dr. B.L. Roberts Prof. dr. O. Naviliat-Cuncic Prof. dr. Y. Kuno

rijksuniversiteit
groningen

This work has been performed as part of the research program of the "Stichting voor Fundamenteel Onderzoek der Materie" (FOM) through program 48 (TRIμP), which is financially supported by the "Nederlandse Organisatie voor Wetenschappelijk Onderzoek" (NWO) under VIDI grant 680.47.203.

Cover photography: LSS Water Splash by YR Miami Digital Studio
Printed by: Van Denderen BV, Groningen, the Netherlands

ISBN:
ISBN:

Contents

Chapter 1

Introduction

The Standard Model (SM) [1] is a remarkable theory that describes all observations in particle physics. However, it lacks in many aspects a deeper explanation, although very accurate predictions can be made within this model that has some 30 free parameters. A number of models beyond the SM have been suggested in order to explain some of its not well understood features such as the number of particle generations, the origin of discrete symmetry violations or the asymmetry of matter and antimatter in the universe. The search for answers to such questions is the driving force behind present particle physics activities at the highest energies available at accelerators and complementary in high precision measurements.

Among the different approaches to search for new physics beyond the SM are searches for permanent electric dipole moments (EDMs) of fundamental particles or systems. The values of such EDMs is predicted within the SM to be many orders of magnitude below present established limits as well as the prospected sensitivity of ongoing EDM searches [2]. Since many of the models beyond the SM predict much larger values, there exists a very large window for discovery of new physics in sensitive searches for EDMs. The discovery of an EDM could be around the corner, because in several speculative models values are predicted just below the present limits for several particles. This thesis concerns work towards a sensitive EDM experiment on the deuteron, in particular the development of a sensitive deuteron spin polarimeter which is a key element in such an experiment.

An overview of EDMs within the Standard Model and some of its extensions is given in chapter 2. The physical similarities and differences between various mechanisms responsible for the creation of an EDM are introduced. The deuteron is brought forward as a promising candidate from both a theoretical and experimental perspective. Basic concepts are presented of a new technique making use of a magnetic storage ring to measure EDMs of charged particles.
The deuteron EDM (dEDM) experiment, as any EDM experiment comprises three different stages. The first step is the *Preparation of a spin polarized beam* which is injected into the storage ring where it will *Interact with the motional electric field* generated by passage through the magnetic field of the ring bending magnets. The interaction between this electric field and the EDM causes the spin to precess. This precession will be detectable in the evolution of the spin which has to be monitored continuously and with high efficiency through *Polarimetry*.
The main polarimetry concepts are introduced in Chapter 3. A possible formalism to describe particle polarization is introduced. An overview on nuclear scattering polarimeters and the implications for the dEDM polarimeter are provided.
The development and optimization of a highly efficient dEDM polarimeter concept constitutes the main subject of this dissertation.

In the design of a sensitive polarimeter analyzing power, efficiency of the detector and the interaction with the beam need to be considered. At the same time, robustness against systematic errors must be taken into account.
The developed concept (presented in Chapter 4) relies on the strong spin dependence of large angle deuteron on carbon elastic scattering. It consists of a three-stage detector comprising an extraction mechanism (to remove the deuterons from the storage ring), a thick target (where the deuterons scatter) and a segmented detector. The extraction mechanism was evaluated for two different methods: extraction via gas interaction and stochastic slow extraction. Different thick targets were considered. The need for the thickness arises from making sure that the efficiency is as high as possible. The optimal location, geometry and material of the target were analyzed. The dEDM detector must be able to reconstruct as many (nuclear) reactions as possible. At the same time it will have to deal with extremely high rates, expected for the dEDM experiment. The configuration and

composition of the target and detection system will determine the sensitivity (the ability to detect small signals) and selectivity (the ability to avoid false signals). Chapter 5 is dedicated to the polarimeter sensitivity. Its optimization is discussed through the optimization of the detector efficiency, reaction analyzing power and figure of merit. This optimization was performed by building a phenomenological deuteron induced reactions scattering model and using it to find the ideal operating point of the dEDM polarimeter. Experimental confirmation of its behavior was performed at COSY. The experimental studies are presented and discussed. The polarimeter selectivity is treated in Chapter 6. Analytical and Monte Carlo models were built that describe the evolution of the polarimeter signal in the presence of systematic effects (beam displacements and rotations). These models enable three different analysis approaches. Experimental studies, performed at KVI and COSY, and the application of the different analysis methods are described and discussed.
The main conclusions of this work are presented in Chapter7. The developed polarimetry concept appears to be well suited for e deuteron EDM experiment with a sensitivity level of 10^{-29} e cm. We therefore give a brief outlook on future research direction towards either establishing a tight upper bound on the deuteron EDM value or its discovery.

Chapter 2

Motivation

2.1 Discrete Symmetries in the Standard Model

The search for violations of fundamental symmetries has played an important role in the development of particle physics in the 20th century. The behavior of a physics observable under a transformation is related to a corresponding symmetry. For a true symmetry, physics observables do not depend on the transformation. Consequently, if a physics observable does change when applying one or more transformations, the corresponding (joined) symmetry must be broken. In particular, tests of the discrete symmetries, charge conjugation C, parity P and time reversal T, have been essential to establish the structure of the SM [3–5]. Parity P is the symmetry related to the reversal of all spatial coordinates, $\vec{r} \rightarrow -\vec{r}$, whereas T is related to the reversal of the time coordinate, $t \rightarrow -t$. Charge conjugation C is the transformation exchanging all particles with antiparticles and vice versa.

Directly associated with the existence of the mentioned symmetries is the CPT theorem [6, 7] that states that any relativistic (Lorentz-invariant) quantum field theory must be invariant under CPT, the combination of C, P and T [6, 7]. As a consequence of this assumed invariance, probing one of these three symmetries is equivalent to probing the combination of the remaining two. For example, probing some process for T invariance is equivalent to probing it for CP invariance.

Tests of the discrete symmetries have provided essential information in the formulation of the SM in its present form [8]:

- The electromagnetic and strong interaction have not yet been shown to violate C, P or T, or any combination of them.
- The discovery of parity violation in the weak interactions [4, 5] indicated that matter fields should be combined into asymmetric left and right handed chiral multiplets, which constitutes one of the indispensable features of the Standard Model.
- The observation of CP violation in the decay of K^0 mesons [3] provided strong evidence for the presence of three quark generations, through the Kobayashi-Maskawa mechanism [9], before experimental indications for the third family had been found.

The search for permanent electric dipole moments (EDMs), which violate both parity and time reversal invariance, is among the most sensitive tests of discrete symmetries. Prior to the observation of parity violation, Purcell and Ramsey proposed considering the EDM of the neutron as a probe for new physics, at that time parity violation. The non-observation of a neutron EDM has, by now, ruled out more speculative models beyond standard theory than any other experimental approach, and established severe constraints on others.

2.2 Electric Dipole Moments

2.2.1 Theoretical Considerations

For a particle in an electric $\vec{E}$ and magnetic $\vec{B}$ fields, the field dependent part of the Hamiltonian is

$$H = -2(\vec{\mu} \cdot \vec{B} + \vec{d} \cdot \vec{E}) = -2(\mu\vec{B} + d\vec{E}) \cdot \hat{S} \tag{2.1}$$

where $\vec{S}$ stands for the spin vector of the particle, the only direction defining vector in the rest frame of the particle, and μ and d are the magnetic and electric dipole moments defined, respectively, as

$$\mu = g(e/2mc) \tag{2.2}$$

and

$$d = \eta(e/2m). \tag{2.3}$$

Under a P transformation, $\vec{E}$ reverses while $\vec{B}$ and $\hat{S}$ remain unchanged. Similarly, under a T transformation, $\vec{B}$ and $\hat{S}$ reverse while $\vec{E}$ remains unchanged. In both situations, the Hamiltonian is modified by the transformation, violating both P and T symmetries, unless $d = 0$. A graphic illustration of these transformations is given in figure 2.1. Under the assumption of CPT invariance, the

Figure 2.1: Symmetry violation for a non-zero EDM. The darker pattern indicates the charge distribution giving rise to an electric dipole moment and the arrows represent the spin. Under a parity transformation the electric dipole moment changes sign (dark pattern inverted vertically) but the spin does not. Similarly, under a time reversal transformation the electric dipole moment does not change but the spin does (change of direction of the black arrow).

T and combined CP symmetries are equivalent. In the current Standard Model, quark mixing leads to CP violation in the weak interaction, which also maximally violates P by itself. The SM thus predicts non-zero EDMs.
Such EDMs arise because of radiative corrections, i.e. the interaction with virtual particles. As all three quark generations need to be involved, only weak interaction corrections of third and higher order (or fourth in the case of leptons) contribute. The resulting Standard Model induced EDMs are at the level of 10^{-36} e.cm for the electron and 10^{-32} e.cm for the neutron. These are far below the sensitivity of current and planned experiments.
With the maturing of Quantum Chromo Dynamics (QCD), it became clear that also the strong interaction Lagrangian may contain a CP violating term. The strength of this term is characterized by the dimensionless parameter $\bar{\theta}$. In the

framework of $SU(3)$ symmetry within the Standard Model, the resulting EDM of the neutron can be calculated to be $d_n = 5 \times 10^{-16}\bar{\theta}$ e.cm.
The current upper limit on the neutron EDM leads to the apparent limit $\bar{\theta} < 10^{-10}$. The not yet understood fine-tuning of the θ-term, which might even be zero, constitutes the so-called strong CP problem of the SM.
Several possible explanations have been proposed for the smallness of $\bar{\theta}$. Some of them involve the existence of a new particle, the axion, which has so far evaded experimental observation [10].
In the Standard Model there is a description of QCD and the electroweak interactions in one single framework. The fine-tuning of θ can be interpreted as the absence of flavor-conserving CP-violation[8]. This is a totally different situation compared to the flavor-changing weak sector to which all the observed CP-violating effects belong. In this case, the incorporation of CP-violation through the Kobayashi-Maskawa mechanism [9] has been supported by experiments using neutral K^0 and B^0 mesons[11, 12]. Another difference is the fact that the phase in the CKM mixing matrix does not require any fine-tuning. The predictions for any CP-violating effect in the flavor-conserving channel, such as EDMs, induced by CKM mixing are very small. This makes it hard to detect experimentally.
Searches for other sources of CP-violation, than the CKM mechanisms, constitute a unique probe for physics beyond the SM. Since the first suggestion by Ramsey and Purcell to search for an EDM of a neutron, such measurements have become some of the most sensitive probes to look for new sources of CP-violation. In case no EDM is found, this constrains new speculative models down to a particular level of sensitivity (see Figure(2.2)). Until now, dedicated searches have not revealed any intrinsic EDM of a fundamental particle or system. With the achieved experimental precision they constitute some of the most stringent tests of the SM.
Looking for new sources of CP-violation is further motivated by the observed matter-antimatter inequality in the Universe. According to Sakharov, this asymmetry could be explained through a combination of C, CP and baryon number violation in an universe out of thermal equilibrium [13]. However, the level of CP-violation in the SM, through the CKM phase or the $\bar{\theta}$ parameter, is insufficient to explain this crucial asymmetry. This constitutes a strong hint that there

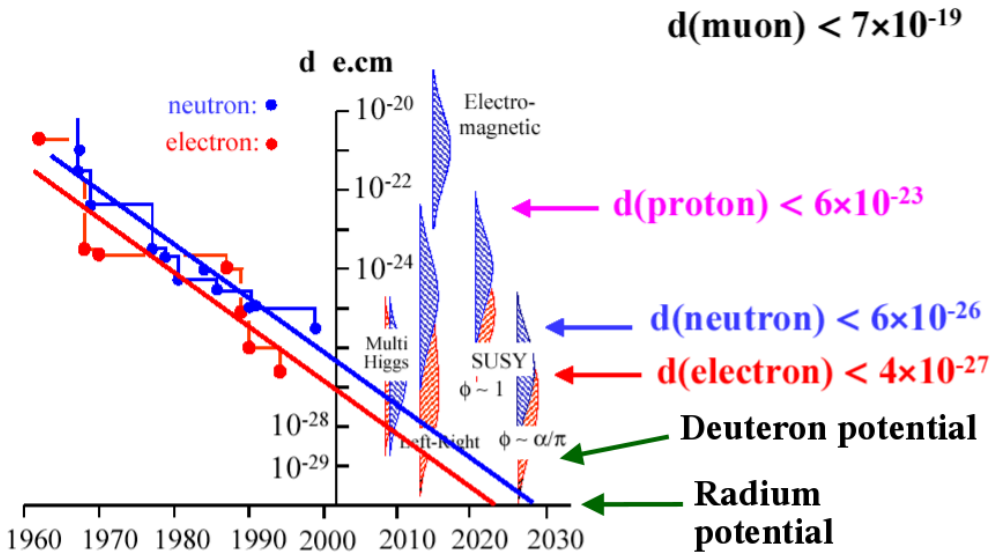

Figure 2.2: EDM searches and SM model extension that can be constrained by them.

could be additional sources of *CP* violation at play. These would give rise to EDMs considerably bigger than those predicted by the SM.
Without knowing the new source for CP violation, no "best" system to look for an EDM can be identified *a priori*. A new *CP*-violating fundamental interaction manifests itself by giving the quarks and leptons an EDM and by modifying the properties of the other interactions. QCD, nuclear, atomic and molecular theory must be applied to obtain the resulting hadronic, nuclear, atomic and molecular EDMs, respectively. A hypothetical new interaction thus gives rise to a distinct pattern of EDMs of different magnitude in some collection of systems and vice versa. The observation of a single non-zero EDM thus suffices to confirm the presence of physics not contained in the SM. To discriminate between various possible forms of this new physics requires the observation of the aforementioned pattern (assumed to give a characteristic "fingerprint"). Different mechanisms responsible for EDMs are shown in picture 2.3.

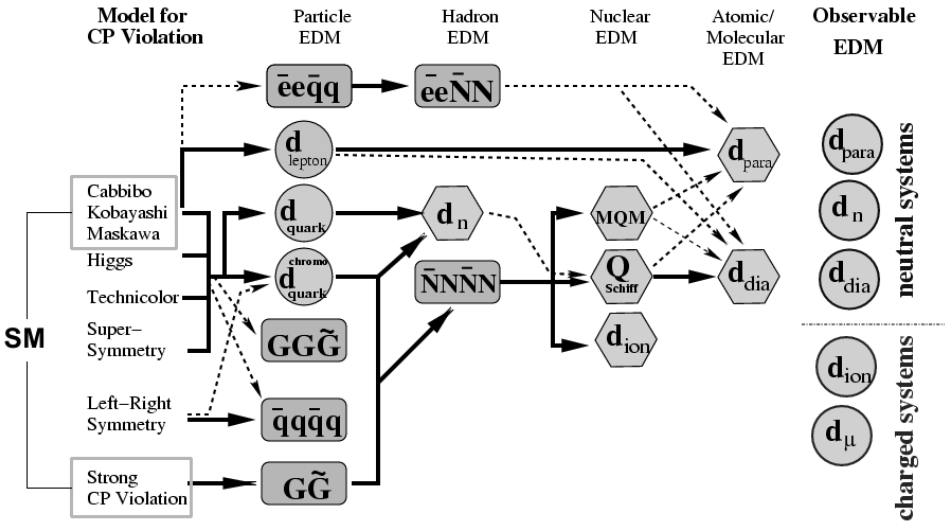

Figure 2.3: Mechanisms responsible for the existence of EDMs [14].

As an example, an EDM arising from P and T-odd pion-nucleon couplings g_i can be expressed as

$$d = A_0 g_0 + A_1 g_1 + A_2 g_2. \tag{2.4}$$

The A_i parameters take different values for different systems. Table 2.1 lists their values for some possible systems.

Table 2.1: Sensitivity to CP-violation for different systems [15].

System	A_0 [e.fm]	A_1 [e.fm]	A_2 [e.fm]
n	0.14		-0.14
D	0.10	0.23	0.00
^{129}Xe	6×10^{-5}	6×10^{-5}	12×10^{-5}
^{199}Hg	2×10^{-6}	2×10^{-4}	-3×10^{-5}
^{225}Ra	-0.06	-0.12	0.11

EDM searches comprise several different approaches and systems which can be distinguished as follows:

1. Searches for EDMs of hadrons, nucleons in particular
2. Searches for EDMs in diamagnetic atoms
3. Searches for EDMs in paramagnetic atoms and molecules.
4. Searches for EDMs in leptons

For each of them the most sensitive experiments to date are on the neutron, mercury and thallium. The electron EDM is calculated from the atomic one. The present limits for each of them are presented in table 2.2. These limits for the different EDMs are comparable despite their apparently different size. They play complementary roles in constraining fundamental *CP*-violation sources.

Table 2.2: Current limits for different EDM types.

Type	System	EDM Limit [e.cm]
Nucleon	n	$\|d_n\| < 2.9 \times 10^{-26}$ (90 % C.L.) [16]
Diamagnetic	^{199}Hg	$\|d_{Hg}\| < 3.1 \times 10^{-29}$ (95 % C.L.) [17]
Paramagnetic	^{205}Tl	$\|d_{Tl}\| < 9 \times 10^{-25}$ (90 % C.L.) [18]
Electron	^{205}Tl	$\|d_e\| < 1.6 \times 10^{-27}$ (90 % C.L.) [18]

The following sections consider each of the cases in more detail.

2.2.2 Experimental Searches

In all EDM experiments, three stages can be recognized.

1. Polarization: an ensemble of spin polarized particles is prepared;
2. Interaction : this ensemble interacts with an electric field;
3. Polarimetry : the evolution of the spin due to the electric field is measured.

2.2.2.1 Neutron

Historically, the neutron was the first particle to be considered as a candidate for an EDM experiment [19]. The first experiment, that set the pace for the EDM studies that followed, was performed at the Oak Ridge reactor in 1949 by Smith, Purcell and Ramsey. It set an example for experimental concepts of future EDM experiments, making use of the change in Larmor precession frequency of the particles in a transverse applied electric field $\vec{E}$ [20]. A scheme of the experimental apparatus is depicted in figure 2.4.

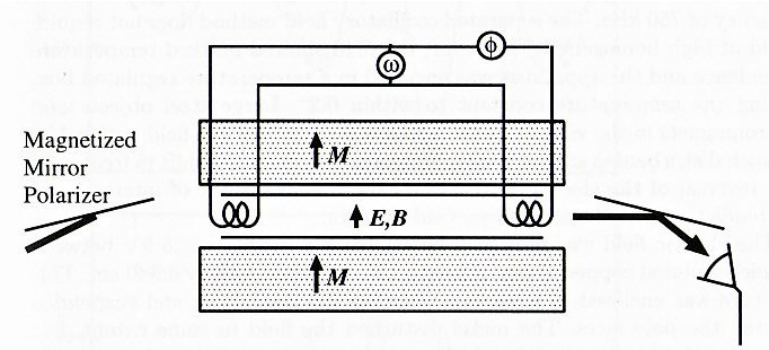

Figure 2.4: Experimental apparatus for the neutron EDM [2]. The neutron beam is polarized by total reflection from a magnetized mirror before entering a region of homogeneous magnetic field from the left side.

A beam of slow neutrons ($E \sim 0.4$ eV) is spin-polarized by reflecting it of a magnetized mirror. Next, they enter a region with collinear electric field E and magnetic field B, oriented perpendicular to the beam. In this field, the neutrons will undergo Larmor precession with frequency $\omega = (2\mu B \pm 2dE)/\hbar$, where the $\pm$ sign corresponds to parallel and anti-parallel E and B fields. An EDM reveals itself through a E-dependent shift in ω. The frequency difference $\Delta\omega = \omega(E^+) - \omega(E^-)$ for E parallel and anti-parallel to B is then given by

$$\Delta\omega = \frac{4d_n E}{\hbar} \tag{2.5}$$

The precession frequency was measured using Ramsey's method of magnetic resonance with spatially separated oscillating fields, implemented as a set of coils placed at the entrance and exit of the field region [21]. The polarization of the

outgoing neutrons is determined by measuring the neutron flux reflected of a magnetized foil.
More recent experiments [22] make use of ultra-cold neutrons (UCNs), which have a typical energy of 100 meV or less. At these energies and for suitable materials, neutrons undergo total internal reflection at any angle of incidence, so that they can be trapped in closed vessels without any appreciable loss for a long time (100's of seconds). The vessel is placed in a collinear electric and magnetic field and the oscillating fields are separated in time, rather than spatially.
The most recent and precise experiment was performed at the Institute Laue-Langevin (ILL) in Grenoble [16], where the result quoted in table 2.2 was obtained. The precision of this result was mainly determined by the limited number of produced and stored ultra cold neutrons. Several efforts, exploring new methods, are underway to improve this precision [23, 24].

2.2.2.2 Schiff's Theorem

It has long been consider impracticable to search for an EDM on charged particles. When placed in a strong electric field such a particle would accelerate and quickly leave the measurement region. It was pointed out by Ramsey and Purcell that applying an external electric field on a neutral atom (or molecule) containing a nucleus or unpaired electron with an EDM is also mostly useless [19]. The charged constituents rearrange themselves such that the force exerted by the external electric force is balanced by the internal forces. In the non-relativistic point-charge limit, the only forces are electrostatic. Hence, the net electric field on each charge is zero. This is commonly referred to as Schiff's theorem. Schiff also pointed out several ways to evade (complete) shielding, making it possible to search for both nuclear and electron EDM using selected atoms.

2.2.2.3 Diamagnetic Atoms : Nuclear EDMs

In diamagnetic atoms shielding of an external electric field is reduced if the nuclear charge and EDM distributions are not the same. In this case, a small residual EDM effect remains in the electron's potential, proportional to the nuclear EDM. This effect is parameterized via the Schiff moment , which is a vector proportional

to the nuclear EDM and which depends on the difference between the normalized charge and EDM distributions. Generally speaking, the Schiff moment is largest for heavy nuclei. It may be further enhanced by one or two orders of magnitude in octupole-deformed nuclei such as ^{225}Ra [25].

The most stringent EDM limit to date was obtained for the spin-1/2 ^{199}Hg nucleus[17]. A quartz cell containing isotopically enriched ^{199}Hg vapor was placed in collinear electric and magnetic fields. The sample is polarized by optical pumping. The subsequent precession frequency of the nuclear spin is determined by observing the modulation rate of the absorption of circularly polarized light. Rather than flipping the orientation of the electric field with respect to the magnetic field, the modulation frequency is measured simultaneously in two cells with oppositely oriented electric fields, but with the same magnetic field. The observed frequency difference is then related to the EDM, as given in equation 2.5. The experimental setup is shown schematically in figure 2.5.

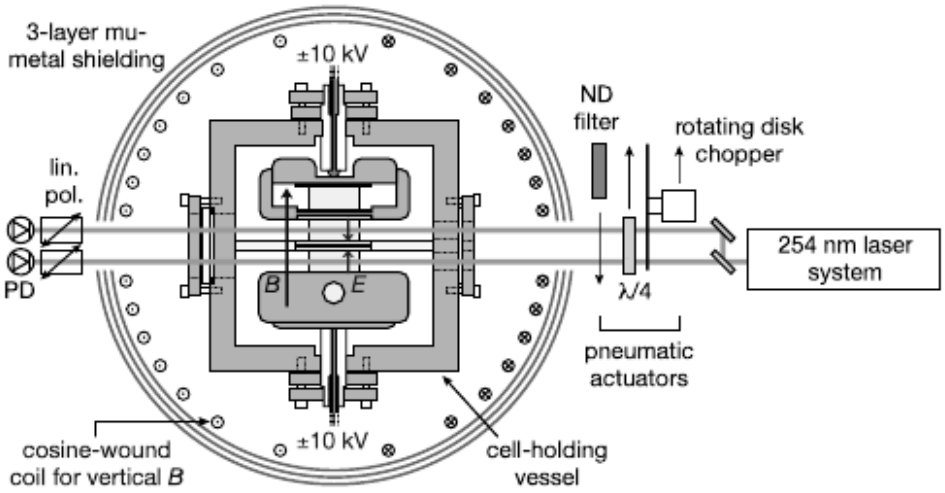

Figure 2.5: Simplified diagram of the ^{199}Hg EDM apparatus showing details of the vapor cell holding vessel and middle cell light beams. The topmost cell is shown inside a cutaway view of the top electrode, while the bottom electrode shows a light access hole for the enclosed cell.

measurement [17]

To reach the current precision, great care had to be taken to eliminate or reduce systematic errors. Some examples include the following. The vapor cells are made out of quartz glass with a high resistance to reduce leakage currents that correlate with the reversal of the electric field and thus mimic an EDM. These cells were placed inside a three-layer magnetic shield. Inside this shield a magnetic field of 15 mG was maintained being stable to 25 ppb on a time scale of 100 s. Fluctuations and a gradient in the magnetic field, which would lead to an EDM-like difference in the precession frequency observed by the two vapor cells, was monitored by placing two additional cells above and below the central ones. These cells are not exposed to electric fields and thus allow precise measurements of the magnetic field. The electric and magnetic field reversals and changes were frequently carried out in order to check for systematic effects.
The largest contribution to the ^{199}Hg nuclear EDM is estimated to arise from P,T-odd nucleon-nucleon interaction. However, calculations show there is also a contribution from the intrinsic EDM of the proton. Thus, besides setting a stringent limit on the ^{199}Hg nuclear EDM, the experimental result can also be related to a limit on the proton EDM [26].
New developments are being pursued in exotic nuclei possessing an octopole moment [27] believed to have enhanced CP-violating effects. Among these is the Radium atom experiment being carried out at KVI [28–30].

2.2.2.4 Paramagnetic Atoms : the Electron EDM

It was shown by Sandars that Schiff's theorem is also evaded when considering relativistic effects on unpaired electrons in paramagnetic atoms [31]. He showed that the atomic EDM induced by the electronic EDM may actually be *enhanced* rather than suppressed. For the ground state of alkali atoms or select other atoms, such as thallium, one finds for the ratio of the EDM of an atom d^{atom} and the EDM of an electron d_e [31–34]

$$|R| = \left|\frac{\mathrm{d}^{atom}}{\mathrm{d_e}}\right| \sim 10\frac{Z^3\alpha^2}{J(J+\frac{1}{2})(J+1^2)}\mathrm{d_e}, \tag{2.6}$$

where J stands for the angular momentum of the electron, Z for the atomic number and α for the fine structure constant.

For a system with large atomic number Z, R may become very large; for thallium, one has calculated $R = -585$ [34]. Atomic paramagnetic systems thus constitute powerful probes to search for an electron EDM. Similar arguments apply to heavy polar diatomic paramagnetic molecules, such as YbF in its ground state or PbO^* in one of its metastable states.

The experimental limit on the atomic or molecular EDM can thus be interpreted as a limit on the electron EDM. This assumes that R is known and that there is no contribution from P,T-odd nuclear-electron interactions. The ^{205}Tl atomic beam magnetic resonance experiments [35] have provided the most precise limit on d_e. The experimental setup is shown in figure 2.6. The experiment makes use of laser optical pumping to polarize the atomic beam and to perform polarimetry through fluorescence.

As in the mercury experiment, two experiments are performed at once in which two beams are exposed to oppositely oriented E and B fields. When moving through a strong transverse electric field $\vec{E}_\perp$ a motional magnetic field $\vec{B}_\perp = -\gamma\frac{1}{c^2}\vec{v} \times \vec{E}_\perp$ appears in the rest-frame of the particles, where $\vec{v}$ is the velocity of the particles and $\gamma = \sqrt{1 - \frac{v^2}{c^2}}$. Due to the interaction with the magnetic moment of the particle, the spin precession frequency will change. This change reverses when the electric field orientation is reversed and thus mimics a non-zero EDM. Therefore, the direction in which the beams travel, meaning the sign of $\vec{v}$, is altered every few second to expose and correct for this effect.

There are many new electron EDM searches in preparation, using a variety of systems, including: atomic cesium, francium or radium; molecular YbF, PbO^*; the molecular ion HfF^+; paramagnetic solids like gadolinium gallium garnet (GGG) or ferri magnetic gadolinium iron garnet (GdIG). It is thus likely that the limit on the electron EDM will be improved considerably in the near future. [2, 31–34, 36–38].

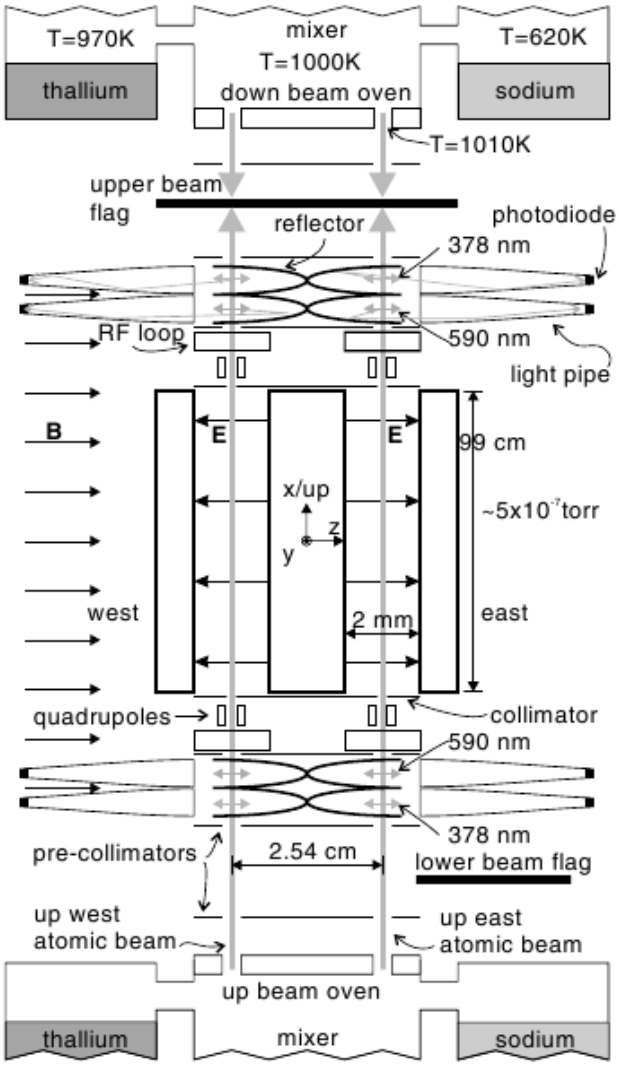

Figure 2.6: Schematic experimental setup used for the ^{205}Tl EDM measurement. Atoms leave the trichamber oven thermally distributed among the ground state hyperfine levels. After some collimation they enter the quantizing magnetic field B. Laser beams then depopulate the states with nonzero magnetic quantum numbers. The atoms then move into the electric field, nominally parallel or antiparallel to B [39].

2.2.2.5 Charged Particles : Muon EDM

All of the EDM experimental approaches presented so far involve the study of neutral particles. To enhance an EDM related signal as much as possible, the system under study must be placed in an electric field that is as strong as possible. In such a field an isolated charged particle experiences a strong force, which is not balanced by internal forces as was the case when the particle was embedded in an atom or molecule. It will thus accelerate and quickly leave the observation region, precluding precise measurement of the precession frequency.
As pointed out by Schiff, this argument does not hold when other than electrostatic forces are present. This is, for example, the case for fast charged particles stored in a magnetic storage ring, where the particles are contained using the Lorentz force. The magnetic field in the laboratory frame gives rise to an electric field in the rest frame of the particle, $\vec{E}_\perp = \gamma\vec{v} \times \vec{B}$. This gives rise to an additional term in the spin precession rate proportional to the EDM, in addition to the terms related to the magnetic moment.
The most stringent EDM limit measured directly on a charged particle has been reported for the muon, $|d_\mu| < 1.9 \times 10^{-19}$ e.cm (95% C.L.) [40, 41]. This limit was obtained in experiment E821 at Brookhaven National Laboratory, which was aimed at measuring the muon anomalous magnetic moment a_μ. A highly uniform magnetic dipole field of 1.45 T, combined with an electric quadrupole field, were used to store polarized muons with a momentum of 3.1 GeV/c. At this so-called "magic" momentum, which satisfies $\beta^2\gamma^2 = 1/a$ with $\beta = \frac{v}{c}$, the spin is insensitive to the electric field. The spin precession, relative to the particle momentum, is then given by

$$\vec{\omega} = \vec{\omega}_a + \vec{\omega}_e = -\frac{e}{m}\left[a\vec{B} + \frac{\eta}{2}\vec{\beta} \times \vec{B}\right], \tag{2.7}$$

with a the magnetic moment anomaly $a = (g-2)/2$ for $\mu = g\frac{e}{2mc}$ and similarly $d = \frac{\eta}{2}\frac{e}{2m}$. The precession frequency is

$$\omega = \omega_a\sqrt{1 + (\eta\beta/2a)^2} \simeq \omega_a\left[1 + \frac{1}{2}\left(\frac{\eta\beta}{2a}\right)^2\right], \tag{2.8}$$

The frequency *shift* is second order in η and thus immeasurably small. The radial component of $\vec{\omega}$, which is *proportional* to the EDM, gives rise to an oscillatory

vertical spin component that is out of phase with the magnetic dipole precession. It is from the limit on the magnitude of this component, that the quoted limit on the muon EDM was derived. Because of the magnetic moment, the spin rapidly

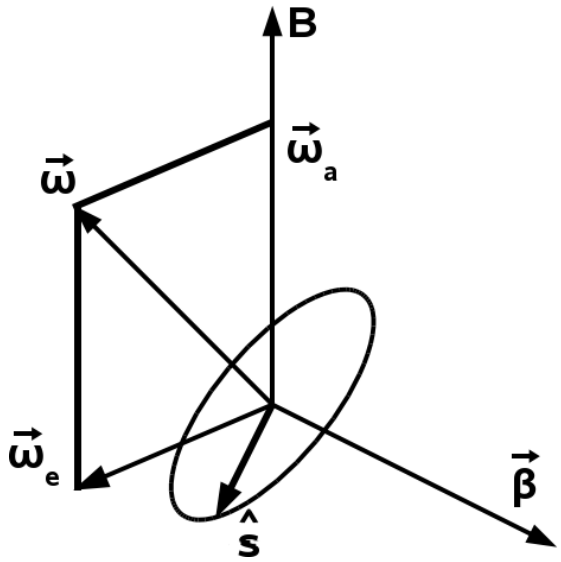

Figure 2.7: Scheme of the orientation of the vectors in the storage ring search for a muon EDM. The angular velocity ω_a is collinear with B, while ω_e is normal to the $\beta \cdot B$ plane. The unit vector $\hat{s}$ represents the spin quantization axis of the muon and its precession is shown. It precesses in the plane perpendicular to $\omega = \omega_a + \omega_e$ resulting in an oscillating vertical component in the laboratory frame [42]

precesses. Therefore, the interaction between the EDM and the electric field cannot build up a large vertical spin component with storage time.
In most theoretical models, including the Standard Model, the electron, muon and tau EDMs are approximately proportional to their masses [42]. From the existing electron EDM limit, one would then predict $d_\mu < 3 \times 10^{-25}$ e.cm, many orders of magnitude below the direct limit. However, plausible models exist in which the mass scaling is quadratic or even cubic, giving rise to a several orders of magnitude larger muon EDM [43, 44]. This possibility motivates d_μ searches at the 10^{-24} e.cm. level [45].

2.3 Storage Ring Techniques for Charged Particle EDM Searches

In the muon EDM experiment described above it was apparent that the effect of an EDM on the spin precession of a particle stored in an ordinary electromagnetic storage ring is extremely small compared to the effect of the magnetic dipole moment. The fast spin precession caused by the magnetic moment prevents the buildup of an EDM induced signal. Several possible schemes have been proposed to overcome this limitation.

2.3.1 Thomas-BMT Equation

In a frame rotating with a particle moving in an electric field E and magnetic field B, the spin precession, including only a magnetic moment, is given by [46]

$$\frac{d\vec{S}}{dt} = \frac{e}{m}\vec{S} \times \left[a\vec{B} - \frac{a\gamma}{\gamma+1}(\vec{\beta}\cdot\vec{B})\vec{\beta} + \left(\frac{1}{\gamma^2-1} - a\right)\vec{\beta}\times\vec{E}\right]. \tag{2.9}$$

This expression is usually referred to as the Thomas-BMT equation, where BMT stands for Bargman-Michel-Telegdi and can be written as

$$\frac{d\vec{S}}{dt} = \vec{\Omega}_{T-BMT} \times \vec{S} \tag{2.10}$$

with

$$\vec{\Omega}_{T-BMT} = -\frac{e}{m}\left[a\vec{B} - \frac{a\gamma}{\gamma+1}(\vec{\beta}\cdot\vec{B})\vec{\beta} + \left(\frac{1}{\gamma^2-1} - a\right)\vec{\beta}\times\vec{E}\right]. \tag{2.11}$$

Including a non-zero EDM results in [47]

$$\begin{aligned} \vec{\Omega} &= \vec{\Omega}_{T-BMT} + \vec{\Omega}_{EDM} \\ &= \vec{\Omega}_{T-BMT} - \frac{e\eta}{2m}\left[\vec{E} - \tfrac{\gamma}{\gamma+1}(\vec{\beta}\cdot\vec{E})\vec{\beta} + \vec{\beta}\times\vec{B}\right] \end{aligned} \tag{2.12}$$

Based on the classical description of the spin motion in combined electric and magnetic fields several experimental methods can be derived to measure or limit a possible EDM of a charged particle moving in those fields.

2.3.2 Parasitic Method

In the aforementioned muon g-2 experiment, a homogeneous magnetic dipole field was used. At the "magic" momentum the effect of the interaction between the electric field and the magnetic moment $(1/(\gamma^2-1)-a=0)$ is canceled and the muon polarization is perpendicular to the magnetic field $(\vec{\beta}\cdot\vec{B}=0)$. In this case, equation. 2.12 reduces to

$$\vec{\Omega} = -\frac{e}{m}\left[a\vec{B} + \frac{\eta}{2}\vec{\beta}\times\vec{B}\right]. \tag{2.13}$$

As was already discussed in some detail above, a non-zero EDM $(\eta \neq 0)$ will lead to an vertical spin component that oscillates with frequency Ω and relative amplitude $\eta\beta/2a$.

2.3.3 Frozen Spin Method

In [48], it is proposed to apply a radially oriented electric field, in addition to a vertical magnetic field. In the proper combination, this eliminates the spin precession caused by the magnetic moment, given by

$$\vec{\Omega}_{T-BMT} = -\frac{e}{m}\left[a\vec{B} + \left(\frac{1}{\gamma^2-1} - a\right)\vec{\beta}\times\vec{E}\right]. \tag{2.14}$$

This term is zero for

$$E_r = \frac{aB_z\beta}{1-(1+a)\beta^2}. \tag{2.15}$$

In the absence of an EDM, the spin will no longer precess. Hence the name "frozen spin". For a non-zero EDM, the remaining spin precession is

$$\vec{\Omega} = -\frac{e\eta}{2m}\left[\vec{E} + \vec{\beta}\times\vec{B}\right] \tag{2.16}$$

Both $\vec{E}$ and $\vec{\beta}\times\vec{B}$ are oriented radially. Spin precession about $\vec{\Omega}$ will cause the polarization to oscillate between longitudinal and vertical.
The (relative) strengths of the magnetic and electric fields needed to freeze the spin depend on the velocity and anomalous magnetic moment of the particle being studied. In most cases the maximum attainable E will be the limiting

factor. Using equation. 2.15 for a completely frozen spin, the spin precession rate can be rewritten as

$$\Omega = \frac{e\eta}{2m} E \frac{a+1}{a\gamma^2} \tag{2.17}$$

Ω is proportional to the EDM and will thus be extremely small. Therefore, in an experiment only a small fraction of a precession cycle can be observed. For a beam with originally longitudinally polarization P_0, the vertical polarization component P_z will evolve as

$$P_z = P_0 \sin \Omega t \simeq P_0 \Omega t = P_0 \frac{e\eta}{2m} E \frac{a+1}{a\gamma^2} t. \tag{2.18}$$

In this approximation, the vertical growth of the polarization component is proportional to the EDM. The strength of the electric field necessary to freeze the spin is proportional to the anomalous magnetic moment. As this strength is usually the limiting factor, this method is only suitable for a particle with a small magnetic anomaly. Furthermore, the effective electric field is inversely proportional to γ^2. The experiment should thus be done at modest energy to avoid reducing the sensitivity.

2.3.4 Electrostatic Method

In the muon g-2 experiment, the fact that at the magic momentum the spin precession is insensitive to the electric field was used to measure the anomalous magnetic moment with great precision. This suggests a third possibility to search for an EDM, namely the use of a purely electrostatic storage ring operating at the magic momentum. For $a > 0$, the magic momentum is determined as

$$\gamma_{magic} = \sqrt{\frac{a+1}{a}}. \tag{2.19}$$

In this case,

$$\vec{\Omega} = -\frac{e\eta}{2m} \vec{E}. \tag{2.20}$$

In the absence of a magnetic field, the particles need to be contained solely by the electric field, which must thus be oriented radially inward. This method therefore only works for positive values of a. Furthermore, no amplification of the electric field occurs. Other than that, this method is equivalent to the frozen spin method.

2.3.5 Resonance Method

The drawback of the parasitic method is the lack of accumulation of the EDM induced spin precession. This is caused by the fact that the torque causing this precession, proportional to

$$\vec{S} \times (\vec{\beta} \times \vec{B}), \tag{2.21}$$

is zero on average because the spin rapidly precesses due to the magnetic moment. However, E need not be static. In [49] a method, reminiscent of the magnetic resonance method, was proposed in which the velocity of a particle (β) moving in a static magnetic dipole field is modulated at the spin precession frequency ($\omega = e/maB$), hence the name "resonance method". In this case,

$$\left\langle \vec{S} \times (\vec{\beta} \times \vec{B}) \right\rangle = S \cdot \delta\beta \cdot B \cdot \cos\phi, \tag{2.22}$$

with $\delta\beta$ the modulation amplitude of β and ϕ the phase between the spin precession and velocity modulation. This will cause a steadily growing vertical polarization component given by

$$P_z = P\frac{e\eta}{2m}\delta\beta Bt\cos\phi, \tag{2.23}$$

in addition to the oscillating vertical spin component, which is proportional to β as in the parasitic method.

This method is in principle applicable to all particles. However, modulation of the particle velocity, also known as synchrotron oscillations, requires a phase-locked accelerating cavity placed in the storage ring. To obtain a large modulation depth $\delta\beta$, the electric field in this cavity must be as strong as possible. The frequency at which the cavity operates is dictated by the spin precession frequency. For a practical cavity, this frequency must be as small as possible. This limits this method to particles with small anomaly, possibly combined with a modest magnetic field strength. The latter reduces the sensitivity.

2.3.6 Rehash

The methods described only address techniques to enhance the interaction between the EDM and an electric field. Further criteria for a sensitive EDM experiment include the availability of an intense source of highly polarized particles.

This drastically limits the number of possible candidates for either of these methods. Finally, a method must exist to track the evolution of the spin, i.e. to perform sensitive polarimetry.
The parasitic method will be exploited again in the planned muon g-2 experiment in preparation at Fermilab [50]. The frozen spin method is being studied as a method to search for an EDM on the positron [51], muon [52] or deuteron [53]. The exploitation of an electrostatic ring is studied for an EDM search on the proton [54]. Of these particles, the deuteron is a unique system, as it is the only nucleus, adding CP-odd parts in the nucleon-nucleon interaction as a possible source for a nuclear EDM in addition to intrinsic EDMs of free particles [55].

2.4 The Deuteron EDM

2.4.1 Origin

Until now, the most stringent bounds on flavor-diagonal CP-violation in the hadronic sector have been established by the EDM limits on the neutron, mercury atom and electron. The sensitivity of each system for existing or new sources of *CP* violation depends on the details and the dynamics of the constituents. The deuteron falls, in terms of complexity, in between the neutron and heavy atoms. It is the simplest system in which the P-odd, T-odd nucleon-nucleon interaction contributes to the EDM. Finding or establishing a limit for its EDM would provide important complementary information to the neutron and atomic systems. It was found that at the level of 10^{-29} e.cm, the deuteron EDM is one to two orders of magnitude more sensitive than any present EDM limit and within the predictions of specific SUSY models[56, 57]. Besides the improvement on sensitivity the deuteron has the advantage of having smaller theoretical uncertainties [58]. At the nuclear level the deuteron EDM can be a result of a combination of the proton and neutron EDMs and also of meson exchange between the nucleons with *CP* odd couplings such that,

$$d_D = d_n + d_n + d_D^{\pi NN}. \tag{2.24}$$

It has been shown that the error for the calculation of $d_D^{\pi NN}$ can be systematically reduced using realistic wave functions for the deuteron [58]. In more complex nuclei, such as ^{199}Hg, large uncertainties are possible because of the complex nuclear structure.

2.4.1.1 Strong CP Violation

The calculation of d_D as a function of the strong *CP*-violating $\bar{\theta}$ parameter, has, for example, been calculated using QCD sum-rules [59]. Numerically, the dependence can be written as

$$d_D \simeq -\left[(7.0 \pm 2.8) + (2.8 \pm 0.8)\right] \times 10^{-17}\,\bar{\theta} e.\text{cm}. \tag{2.25}$$

For the neutron,

$$d_n = 1.2 \times 10^{-16}\,\bar{\theta} e.\text{cm} \tag{2.26}$$

These results evaluated for the predicted sensitivity of the neutron EDM of 10^{-28} e.cm and the deuteron EDM of 10^{-29} e.cm leads to a limit for $\bar{\theta}$ of

$$|\bar{\theta}| < 8 \times 10^{-12}, \tag{2.27}$$

for the neutron and

$$|\bar{\theta}| < 3 \times 10^{-13}, \tag{2.28}$$

for the deuteron case. This seems to indicate that the projected EDM limit on the deuteron is at least one order on magnitude more constraining on $\bar{\theta}$ than the one projected for a future neutron EDM.

2.4.1.2 Quark Chromo EDMs

An example of a New Physics contribution, EDMs induced by color EDMs at the quark level are considered. Chromo EDMs (or quark-color EDMs) can arise from SUSY loops and give rise to regular quark EDMs. A comparison can be established between the neutron and the deuteron, in terms of sensitivities [56–58].

$$d_n \approx 1.4(d_d - 0.25 d_u) + 0.83 e(d_d^c + d_u^c) + 0.27 e(d_d^c - d_u^c) \tag{2.29}$$

$$d_D \approx (d_d + d_u) + 6 e(d_d^c - d_u^c) - 0.2 e(d_d^c + d_u^c) \tag{2.30}$$

where d_q stand for the regular electromagnetic quark EDMs and d_q^c for the chromo EDMs of a quark of q flavor. Rewriting the previous expressions, only as a function of the chromo EDMs it comes [56] [58],

$$d_n \approx -0.01 d_d^c + 0.49 d_u^c, \tag{2.31}$$

$$d_D \approx -4.67 d_d^c + 5.22 d_u^c. \tag{2.32}$$

These two EDMs probe different linear combinations of the up and down quark contributions, signaling once more the complementarity between possible future experiments. Using a comparative approach, the simple numerical comparison between the coefficients for the different quark contributions for the neutron and the deuteron, the latest appears to be more sensitive by one to two orders of magnitude, at least in this case.

2.4.1.3 Dimensional Analysis

An estimate can be made of the scale of new physics that EDM experiments are sensitive to. Defining the EDM of a particle as [60]

$$d_i \approx \frac{m_i}{\Lambda^2} e \sin\phi \tag{2.33}$$

where m_i is the mass of the particle, $\sin\phi$ corresponds to the CP-violating phase and Λ the new physics energy scale. For a quark mass of ~ 10 MeV and $\sin\phi$ of order $1/2$ it becomes [60]

$$d_D = 10^{-22} \left(\frac{1|TeV|}{\Lambda} \right)^2 e.\text{cm}. \tag{2.34}$$

This means that for $d_D = 10^{-29}$ e.cm the new physics scale is probed at $\Lambda \sim$ 3000 TeV. The competitiveness in terms of sensitivity, together with the relative theoretical simplicity of its wave function and consequent physical interpretation, the experimental availability of polarized samples and its small anomalous magnetic moment, establishes the deuteron as the ideal candidate for an EDM search on charged particles in a storage ring.

2.4.2 Proposed Experiment

For the proposed deuteron EDM experiment presented to the Brookhaven National Laboratory in 2008 [60] each of the three distinct steps introduced in section 2.2.2 are addressed.

2.4.2.1 Polarization

Polarization is the initial stage of the experiment and it consists of preparing an ensemble of spin polarized particles. This is achieved by using polarized ion sources which are widely available and well understood. Examples of such sources are the POLIS at KVI [61] and the polarized H^- source at BNL [62] which provide very high polarizations at the level of 70-90%.

2.4.2.2 Interaction

The polarized sample, delivered by the ion source, interacts with an electric field in a storage ring. The method found most suitable is the frozen spin method. For its application, a conceptual EDM ring was designed [63]. The ring parameters of relevance for this study are the choice of deuteron momentum acceptable for efficient deuteron polarimetry, $p_D = 0.7$ GeV/c, the magnitude of the electric field determines the precession frequency and horizontal emittance at the chosen 5 cm distance between electrodes $E_R = 3.5$ MV/m and the free space available between lattice determines the size and numbers of polarimeters.

2.4.2.3 Polarimetry

Monitoring of the spin behavior under the effect of the applied electric field needs to be performed in a continuous and highly efficient manner. Deuteron polarimetry in storage rings has previously been carried out attaining efficiencies of the order of 10^{-6} [64].
The success of the experiment depends on the combination of all three stages described here. The development and research of a new highly efficient deuteron polarimeter concept constitute the main subject of this dissertation.

Chapter 3

Polarimetry

In this section a brief description of a possible polarization formalism is provided, followed by an overview of polarimetry techniques and their implementation.

3.1 Particle Polarization Formalism

The spin part of the quantum mechanical state of a particle with spin-1/2 can be described by a Pauli spinor [65],

$$\chi = \begin{pmatrix} a_1 \\ a_2 \end{pmatrix} = a_1 \begin{pmatrix} 1 \\ 0 \end{pmatrix} + a_2 \begin{pmatrix} 0 \\ 1 \end{pmatrix} \tag{3.1}$$

with complex amplitudes a_1 and a_2, where $|a_1|^2 + |a_2|^2 = 1$. The expectation value of a spin operator A is given by

$$\langle A \rangle = \langle \chi | A | \chi \rangle = \chi^\dagger A \chi \tag{3.2}$$

The expectation values for the spin three-vector can be obtained using the Pauli operators

$$\sigma_x = \begin{pmatrix} 0 & 1 \\ 1 & 0 \end{pmatrix}, \ \sigma_y = \begin{pmatrix} 0 & -i \\ i & 0 \end{pmatrix}, \text{ and } \sigma_z = \begin{pmatrix} 1 & 0 \\ 0 & -1 \end{pmatrix}. \tag{3.3}$$

This yields

$$\vec{S} = \frac{\hbar}{2} \begin{pmatrix} \langle \sigma_x \rangle \\ \langle \sigma_y \rangle \\ \langle \sigma_z \rangle \end{pmatrix} = \frac{\hbar}{2} \begin{pmatrix} a_1^* a_2 + a_2^* a_1 \\ -i a_1^* a_2 + i a_2^* a_1 \\ a_1^* a_1 + a_2^* a_2 \end{pmatrix} \tag{3.4}$$

In the description of spin precession, this spin three-vector can be treated as a classical vector.
For an ensemble of N particles a set of Pauli spinors can be defined,

$$\chi^{(n)} = \begin{pmatrix} a_1^{(n)} \\ a_2^{(n)} \end{pmatrix}, \tag{3.5}$$

where n runs from 1 to N covering all involved particles. Considering the *average* spin and not the order of the different spins, a beam of particles can be described through the density matrix [66]:

$$\rho = \frac{1}{N} \begin{pmatrix} \sum_{n=1}^{N} \left| a_1^{(n)} \right|^2 & \sum_{n=1}^{N} a_1^{(n)} a_2^{(n)*} \\ \sum_{n=1}^{N} a_2^{(n)} a_1^{(n)*} & \sum_{n=1}^{N} \left| a_2^{(n)} \right|^2 \end{pmatrix}. \tag{3.6}$$

This matrix fully describes the magnitude and direction of the expectation of the spin of the particle beam and can be expanded into a combination of Pauli spin operators

$$\rho = \frac{1}{2} \left(I + \sum_{j=x,y,z}^{3} p_j \sigma_j \right). \tag{3.7}$$

The p_j coefficients represent the spatial components in the x, y and z directions of a chosen coordinate system and I is the unit matrix

$$I = \begin{pmatrix} 1 & 0 \\ 0 & 1 \end{pmatrix} \tag{3.8}$$

The vector $\vec{p} = (p_x, p_y, p_z)$ can be interpreted as a classical vector representing the polarization of the beam.
Spin-1 particles can be described in analogy with the spin-1/2 ones. Such a particle can be characterized by a three-component spinor

$$\chi = \begin{pmatrix} a_1 \\ a_2 \\ a_3 \end{pmatrix}. \tag{3.9}$$

The basic angular momentum operators for a spin-1 particle are

$$S_x = \frac{\hbar}{\sqrt{2}} \begin{pmatrix} 0 & 1 & 0 \\ 1 & 0 & 1 \\ 0 & 1 & 0 \end{pmatrix}, S_y = \frac{\hbar}{\sqrt{2}} \begin{pmatrix} 0 & -i & 0 \\ i & 0 & i \\ 0 & i & 0 \end{pmatrix}, S_z = \begin{pmatrix} 1 & 0 & 0 \\ 0 & 0 & 0 \\ 0 & 0 & -1 \end{pmatrix}. \tag{3.10}$$

These three operators together with the 3×3 identity matrix are not sufficient to describe the state of a spin-1 particle completely. Five other Hermitian operators are still necessary [66].
A second-rank tensor can be constructed from nine operator products of the spin component operators S_x, S_y and S_z.

$$T = \begin{pmatrix} S_x \\ S_y \\ S_y \end{pmatrix} \begin{pmatrix} S_x & S_y & S_y \end{pmatrix} = \begin{pmatrix} S_xS_x & S_xS_y & S_xS_z \\ S_yS_x & S_yS_y & S_yS_z \\ S_zS_x & S_zS_y & S_zS_z \end{pmatrix}, \tag{3.11}$$

In standard Cartesian notation a set of ten operator can be constructed.

$$I = \begin{pmatrix} 1 & 0 & 0 \\ 0 & 1 & 0 \\ 0 & 0 & 1 \end{pmatrix}. \tag{3.12}$$

$$S_x; S_y; S_z. \tag{3.13}$$

$$T_{xy} = 3S_xS_y; T_{xz} = 3S_xS_z; T_{yz} = 3S_yS_z. \tag{3.14}$$

$$T_{xx} = 3S_xS_x - 2I; T_{yy} = 3S_yS_y - 2I; T_{zz} = 3S_zS_z - 2I. \tag{3.15}$$

From these ten operators only nine can be independent. Considering the relation

$$T_{xx} + T_{yy} + T_{zz} = \begin{pmatrix} 0 & 0 & 0 \\ 0 & 0 & 0 \\ 0 & 0 & 0 \end{pmatrix}, \tag{3.16}$$

the operators T_{xx}, T_{yy} and T_{zz} can be replaced by either of the pairs

$$T_{xx} - T_{yy}, T_{zz} \tag{3.17}$$

$$T_{yy} - T_{zz}, T_{xx} \tag{3.18}$$

$$T_{zz} - T_{xx}, T_{yy} \tag{3.19}$$

which results in a complete set of orthogonal operators. These can be used to expand the density matrix for an ensemble of spin-1 particles as

$$\rho = \frac{1}{3}\left[I + \sum_i p_i S_i + \sum_{i,j} p_{ij} T_{ij}\right] \tag{3.20}$$

where the p_i and p_{ij} stand for the polarizations associated with each operator [67].
Typical polarized beam sources that may be used for the deuteron EDM search posses axial symmetry [67]. In that case all off-diagonal elements of ρ are zero. Assuming the z axis as the symmetry axis equation 3.20 can be simplified to

$$\rho = \frac{1}{3}\left(I + p_z S_z + \frac{1}{2} p_{zz} T_{zz}\right). \tag{3.21}$$

The vector polarization P_V and tensor polarization P_T are then both fully defined by the population densities only,

$$P_V = p_z = \frac{\rho^+ - \rho^-}{\rho^+ + \rho^0 + \rho^-} \tag{3.22}$$

$$P_T = p_{zz} = \frac{\rho^+ + \rho^- - 2\rho^0}{\rho^+ + \rho^0 + \rho^-}, \tag{3.23}$$

where $\rho^+ = \sum \left|a_1^{(n)}\right|$, $\rho^0 = \sum \left|a_2^{(n)}\right|$ and $\rho^- = \sum \left|a_3^{(n)}\right|$.

3.2 Polarization in Nuclear Scattering

For spin-1 bosons the magnetic dipole moment and the electric quadrupole moment are oriented in the direction of the only vector of the system, the spin of the particle. The spin orientation thus manifests itself in the electromagnetic interactions of this particle with its environment. For example, the hyperfine state of the atom includes the orientation of the nuclear spin. In the strong interaction similar phenomena occur. For example, the relative orientation of the proton and neutron spins plays a crucial role in the description of the ground state of the deuteron [68].

Also in nucleus-nucleus scattering the interaction between the two nuclei depends in general on their respective spins. The nuclear potential can be expressed as [69]

$$V = V_0(r) + V_s(r)\vec{s_1} \cdot \vec{s_2} + V_{SL}(r)\vec{S} \cdot \vec{L} + V_T(r) \left[\frac{3}{r^2}(\vec{s_1} \cdot \vec{r})(\vec{s_2} \cdot \vec{r}) - \vec{s_1} \cdot \vec{s_2} \right]. \quad (3.24)$$

Each term represents a distinguishable contribution. $V_0(r)$ is the central potential, $V_s(r)$ is the spin-spin interaction,$V_{SL}(r)$ is the spin-orbit coupling and $V_T(r)$ is the tensor part.

Of particular interest is the spin-orbit term, which arises from the interaction between the total spin of the two nuclei and the angular momentum arising from their relative motion. For a target nucleus with spin-0, the contribution of this term is completely determined by the spin of the incoming nucleus. Furthermore, the spin-spin and tensor terms vanish.

If the polarization of the particles in the final state is not measured, all configurations with the same total angular momentum in the initial and final state contribute to the reaction amplitude because of angular momentum conservation. In that way the spin in the initial state couples to the orbital angular momentum in the final state. The manifestation of the latter in the scattering cross section can be used to extract the polarization of the incoming particle.

The scattering of a polarized beam is commonly analyzed using the nomenclature defined in the Madison convention [67] (shown in figure 3.1). A Cartesian coordinate system is assumed in which the z-axis points along the incident beam momentum $\vec{p}_{in}$. The y-axis y points along $\vec{p}_{in} \times \vec{p}_{out}$, where $\vec{p}_{out}$ stands for the scattered particle momentum. The x-axis x is defined in such a way to obtain a right-handed system. The unit vectors associated with the x, y and z axis are $\hat{x}$, $\hat{y}$ and $\hat{z}$, respectively. The unit vector pointing along the spin quantization axis is $\hat{s}$. Its direction is defined through the angles β and ϕ. The angle β is enclosed between the quantization axis and the beam direction and is derived from $\cos\beta = \hat{z} \cdot \hat{s}$. The angle ϕ spans between the projection of the quantization axis in the $x - y$ plane and the y axis. The orientation of ϕ is essential in the definition of the Madison convention and is defined between the scattering plane and the spin quantization plane.

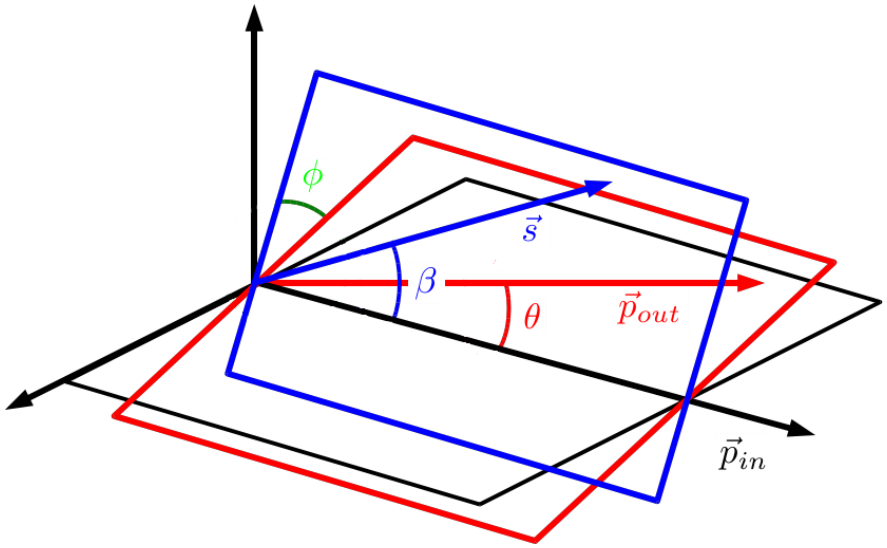

Figure 3.1: Coordinate planes for the deuteron on carbon scattering interaction. The black plane (ground plane) contains the incoming beam $\vec{p}_{in}$. The red plane (scattering plane) contains the incoming and outgoing beams $\vec{p}_{in}$ and $\vec{p}_{out}$. The blue plane (spin quantization plane) contains the spin quantization axis $\vec{s}$. The angle θ is defined as the angle between the scattering plane and the ground plane. The angle β is defined as the angle between the spin quantization axis and the ground plane. The angle ϕ is defined as the angle between the spin quantization plane and the scattering plane.

.

In this coordinate system, the differential cross section $\frac{d\sigma}{d\Omega}$ for detecting a single particle at angle θ and φ when scattering a polarized spin-1 particle off an unpolarized target can be written as

$$\frac{d\sigma}{d\Omega}(\theta,\phi) = \frac{d\sigma}{d\Omega}_{unp}(\theta)\left[1+\frac{3}{2}p_y A_y(\theta) + \frac{2}{3}p_{xz}A_{xz}(\theta)+\frac{1}{3}p_{xx}A_{xx}(\theta)+\frac{1}{3}p_{yy}A_{yy}(\theta)+\frac{1}{3}p_{zz}A_{zz}(\theta)\right]. \quad (3.25)$$

The various p_{ij} coefficients with $i,j = x,y,z$ stand for the different polarization components of the incident beam and contain the φ dependence. The A_{ij} coefficients with $i,j = x,y,z$ represent the associated reaction analyzing powers. These analyzing powers measure the sensitivity of the system to the occurrence

of a certain reaction. The double lower indexing means a tensor component in opposition to the single index for a vector component. This parameterization holds for either elastic or quasi-elastic scattering to discrete states or inclusive reactions in which the energy of the reaction product is not measured.
Note that the reaction is only sensitive to the vector polarization component *perpendicular* to the scattering plane defined by $\vec{p}_{in}$ and $\vec{p}_{out}$. This is a consequence of parity conservation in the strong and electromagnetic interaction. For the same reason, there is only sensitivity to p_{xx}, p_{yy}, p_{zz} and p_{xz}.
The differential cross section can also be written in spherical coordinates as

$$\frac{d\sigma}{d\Omega}(\theta,\phi) = \frac{d\sigma}{d\Omega}_{unp}(\theta)\,[1 + 2\ it_{11}\ iT_{11}(\theta) + t_{20}\ T_{20}(\theta) + 2\ t_{21}\ T_{21}(\theta) + 2\ t_{22}\ T_{22}(\theta)] \tag{3.26}$$

where the $T_{kq}(\theta)$ are the analyzing powers of rank k ($k = 1$ is vector, $k = 2$ is tensor) and the t_{kq} are the corresponding beam polarizations.
In the (Carthesian) reference frame of the source the beam usually has only non-zero p_V and p_T, meaning a vector and tensor polarization along some axis. The orientation of this axis with respect to the reaction plane is defined by β and ϕ. The corresponding spherical polarizations are then given by

$$\begin{array}{rclrcl} it_{11} &=& \frac{\sqrt{3}}{2}\ p_V\ \sin\beta\ \sin(\phi), & t_{21} &=& -\sqrt{\frac{3}{2}}\ p_T\ \sin\beta\ \cos\beta\ \cos(\phi), \\ t_{20} &=& \frac{1}{2\sqrt{2}}\ p_T\ (3\cos^2\beta - 1), & t_{22} &=& \frac{\sqrt{3}}{4}\ p_T\ \sin^2\beta\ \cos 2(\phi). \end{array} \tag{3.27}$$

with p_z and p_{zz} the vector and tensor polarizations as defined in equations 3.22 and 3.23.
For a purely vector polarized beam ($p_T = 0$) the cross section exhibits a maximum or minimum for $\phi = \pm 90°$. The difference between this maximum and minimum reaches its maximum for $\beta = 90°$, i.e, when the polarization is perpendicular to the reaction plane. In a similar way the tensor polarization reflects primarily the azimuthal dependence of the cross section. If the analyzing powers are known it is possible to reconstruct the beam polarization.
Based on this elementary description various polarimeters that have been developed in the past are described briefly in the remainder of this chapter.

3.3 Nuclear Scattering Polarimeter

The cross section and analyzing power given in equations. 3.25 and 3.26 determine the sensitivity with which the beam polarization can be measured. Both depend on the species and energy of the incoming beam and the type of nuclei in the scattering target. For a given beam, the target can be chosen to optimize the sensitivity.

For example, nuclear rainbow scattering exhibits a large spin dependence in large angle scattering for protons and deuterons scattered off medium sized nuclei, due to the combination of the size of the nucleus, the de Broglie wavelength of the incoming particles and angular momentum conservation [70]. As a second example, the interference between electromagnetic and nuclear scattering, also produces sizable analyzing powers [71].

Various polarimeter setups have been used in the past to determine vector and tensor polarizations, of which three are described: the POMME polarimeter at Saturne National Laboratory, from which the concept for the proposed dEDM polarimeter is derived, the IBP polarimeter and the EDDA polarimeter which were employed in the measurements performed at KVI and at COSY in the course of the dEDM polarimeter development.

3.3.1 POMME Polarimeter at Saturne

The POMME polarimeter is a proton and deuteron polarimeter at Saturne[64, 72] that has been calibrated for deuteron energies between 150 and 700 MeV. It is based on the inclusive reaction $d + C \rightarrow$ one charged particle $+ X$ on a thick carbon target. POMME has been designed as a compact, movable, independent detection system placed at the end of a beamline.

The geometry of the polarimeter is shown in figure 3.2. The position sensitive multiwire proportional chambers C1, C2, C3 and C4, C5, C6 enables the trajectory reconstruction of the particles upstream and downstream of the carbon target, from which the scattering angle and vertex can be reconstructed. The redundancy of the localization of each track provides a good control of the alignment. Misalignment is the main source for systematic errors, which are thus also well controlled. The performance of the polarimeter is optimized by selecting

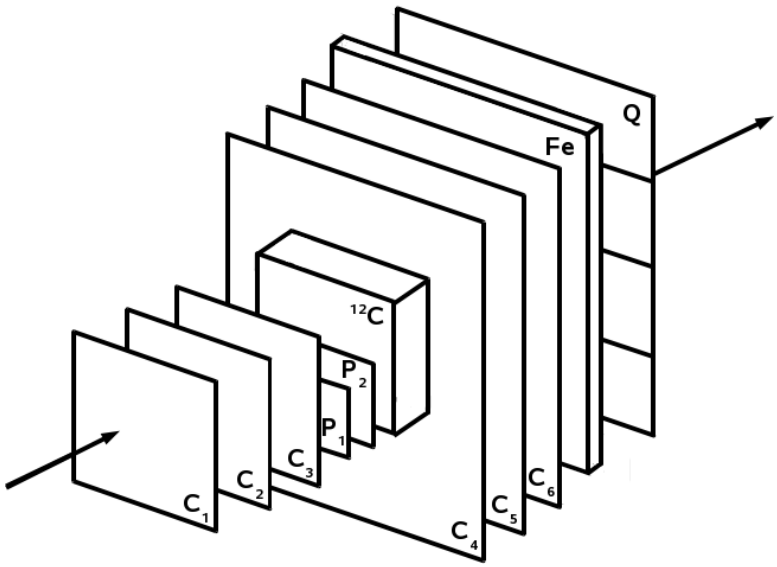

Figure 3.2: Schematic view of the POMME polarimeter at Saturne [64]. The arrow represent the beam direction. The detector is composed of several position sensitive multiwire proportional chambers C1, C2, C3 and C4, C5, C6 that make possible the reconstruction of the trajectory of the particles. To select high energy particles it possesses an iron absorber labelled Fe just upstream of the scintillator detectors P_1, P_2 and Q that trigger the system.

high energy particles. This is accomplished by requiring a hit in the scintillator detectors P_1 and P_2 placed just upstream of the target and Q just behind an iron absorber labeled Fe.
The target thickness is chosen to improve the efficiency. The probability for a nuclear scattering reaction to occur is (to first order) proportional to that thickness. The scattering target is therefore rather thick and consists of layers 1.2 or 2.4 cm thick carbon slabs with a density of 1.7 g/cm^3. Depending on the beam energy these layers can be assembled together to obtain a particular thickness up to a maximum of 15 cm.
The incoming particles loose energy in the target. Furthermore, several reactions contribute to the production of charged particles. As a consequence, the rate distribution of these particles is determined by a combination of several cross sections and analyzing powers. Note that also multiple Coulomb scattering (MCS) will

contribute. MCS is strongly forward peaked and has little sensitivity to the spin of the incoming particle leading to modest deterioration of the angular resolution of the detector.
The number of particles detected at (θ, ϕ) is given by

$$N(\theta,\phi) = C\frac{d\sigma}{d\Omega}(\theta)D(\theta,\phi)\left(1+\sqrt{2}p_z iT_{11}(\theta)\cos(\phi)\right. \\ \left. -\frac{1}{2}p_{zz}T_{20}(\theta) - \sqrt{\frac{3}{2}}p_{zz}T_{22}(\theta)\cos 2\phi\right), \quad (3.28)$$

where C is a constant, $\frac{d\sigma}{d\Omega}$ the cross section for unpolarized beam, $D(\theta, \phi)$ is the detection efficiency, p is the beam polarization and T_{ij} represents the different analyzing powers in spherical coordinates. At Saturne, the polarization axis was always vertical, meaning $\beta = 90°$. These parameters can be determined using several known polarization states. For an angular range of $4.5° < \theta < 22.5°$ the polarimeter efficiency was found to be $4 - 10\%$ for an average analyzing power of 0.2-0.3 for different energies. This value for efficiency is larger than the typical 10^{-6} level obtained for typical polarimeters found in storage rings.
POMME constitutes at this moment the polarimeter type closest to the one being developed for the search of a deuteron EDM on a storage ring, a highly efficient counting polarimeter with extremely good systematic error control and wide angle coverage.

3.3.2 In-Beam Polarimeter at KVI

The main goal of the In-Beam Polarimeter (IBP) [73] is to provide a fast on-line determination of the beam polarization. Its operation is based on elastic scattering of polarized protons or deuterons from a thin proton target. The use of a thin target (100mg/cm^2) enables the operation the polarimeter in parallel to downstream scattering experiments. The IBP is located upstream of the two main beam lines where experiments with polarized particles are generally carried out (see Figure 3.3).

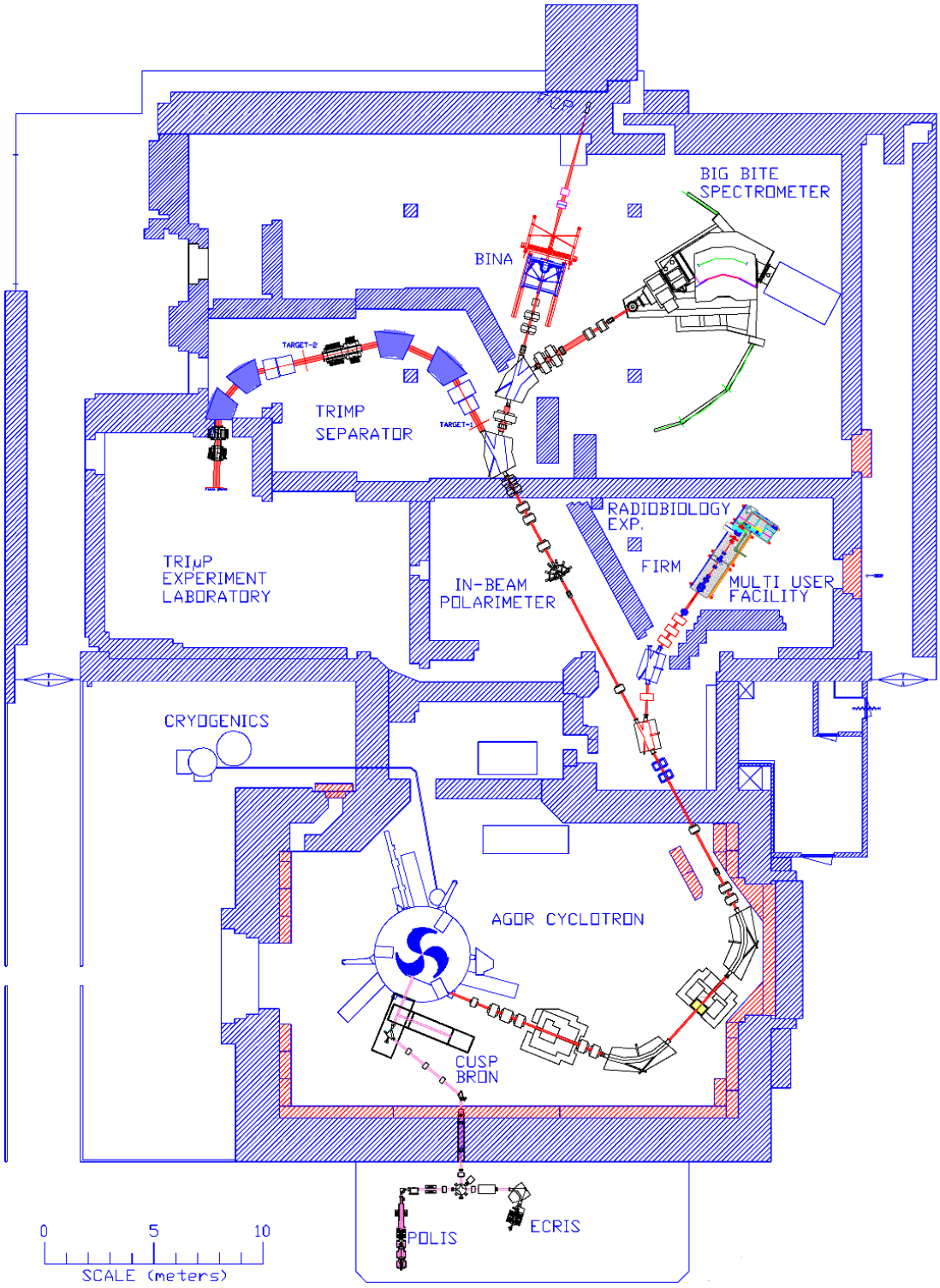

Figure 3.3: The KVI facilities fed by beams of the AGOR cyclotron (bending limit of 600 MeV). The In-Beam Polarimeter is located in the main beamline in the center of the experimental hall.

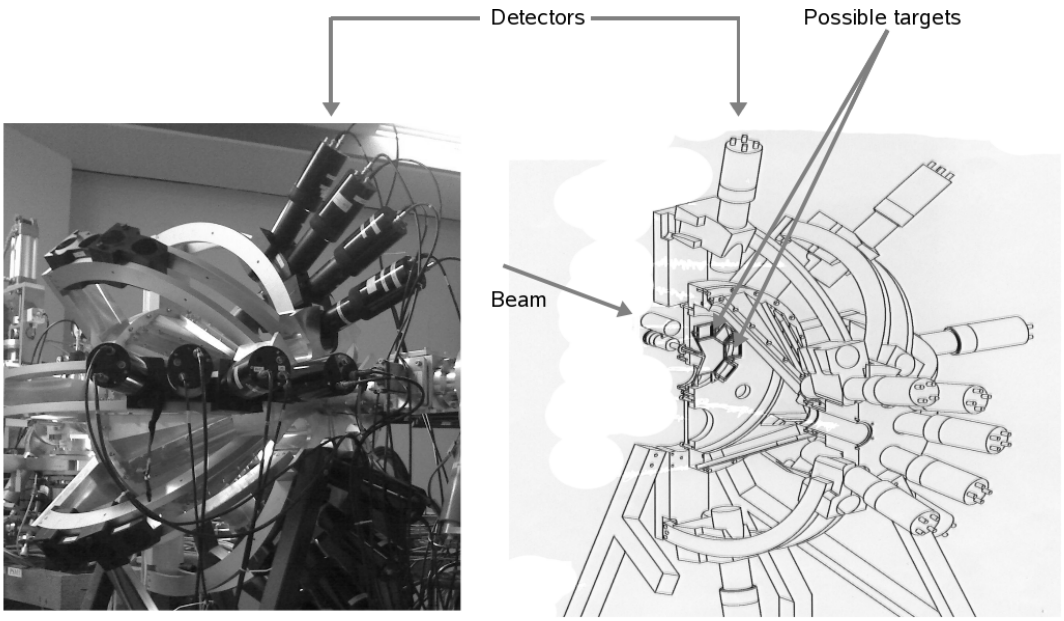

Figure 3.4: Photograph (left) and scheme (right) of the IBP detector at KVI. In both representations the detector arms supporting photomultipliers are visible. On the scheme on the right side, the target area of the detector is shown.

Eight different targets can be mounted on a wheel. The target wheel can be rotated by a stepping motor with a step-size of 0.0243 degrees. Given the dimension of the target wheel, one step corresponds to about 0.03 mm target movement. The target wheel is placed in a conical vacuum chamber with thin exit windows. Detectors are mounted outside these windows. Usually two detectors are positioned on each of eight arms resulting in a total of 16 detectors (see Figure 3.4). This enables the measurement of kinematic coincidences in four independent planes, 45 degrees apart in azimuthal angle. The spin axis is perpendicular to the beam line. The available range in polar angle is 15 to 90 degrees in each arc. The solid angle covered by each detector is approximately 7 msr.
The detectors are phoswich constructions in order to facilitate particle identification. They consist of two plastic scintillator layers: a thin NE102A3 scintillator with a fast decay constant of 2.4 ns combined with a thicker NE115 scintillator with a slow decay constant of 320 ns [73]. The total thickness of the detectors is sufficient to stop 190 MeV protons scattering at 18 degrees. Although the targets are very thin, they still perturb the passing beam via multiple Coulomb scattering (MCS). In high precision experiments conducted downstream of the IBP this effect was noticed [74].

3.3.3 EDDA detector at COSY

The EDDA detector is a multi-purpose detector located at the COSY storage ring of the Forschungszentrum Jülich. An overview of the COSY facility is depicted in figure 3.5.
This detector was originally designed for high precision measurements of proton-proton elastic scattering excitation functions ranging from 0.5 to 2.5 GeV in excitation energy. Today, EDDA is used as a polarimeter during accelerator setup [75] and for dedicated spin manipulation measurements [76]. The EDDA detector comprises (from the inside outwards) three distinct layers: a fiber array, a layer of scintillator bar detectors and a layer of scintillator ring detectors. A figure and a schematic view of the detector are shown in figure 3.6.

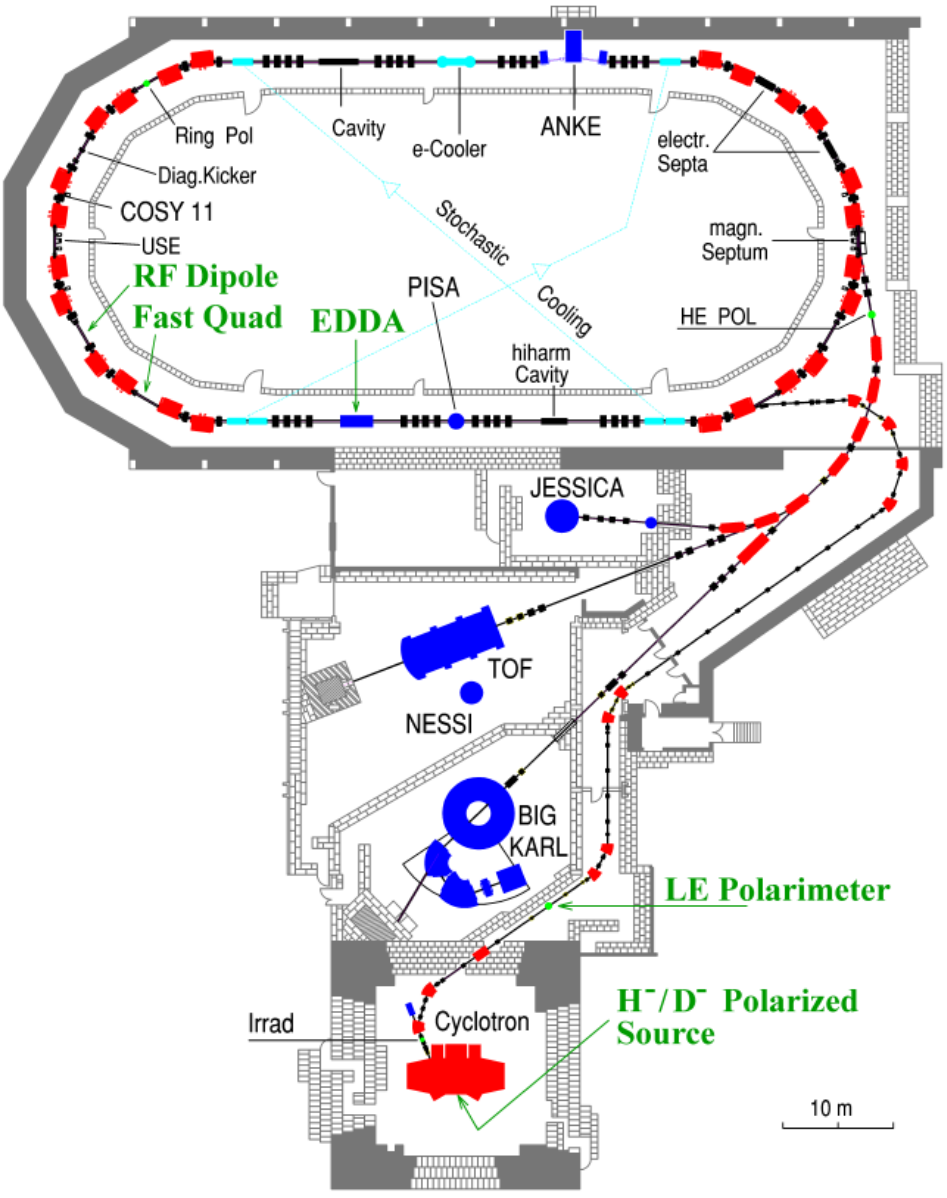

Figure 3.5: The COSY accelerator facility, with the location of various experiments and setups indicated. The EDDA detector is located in the second half of the bottom straight section [77].

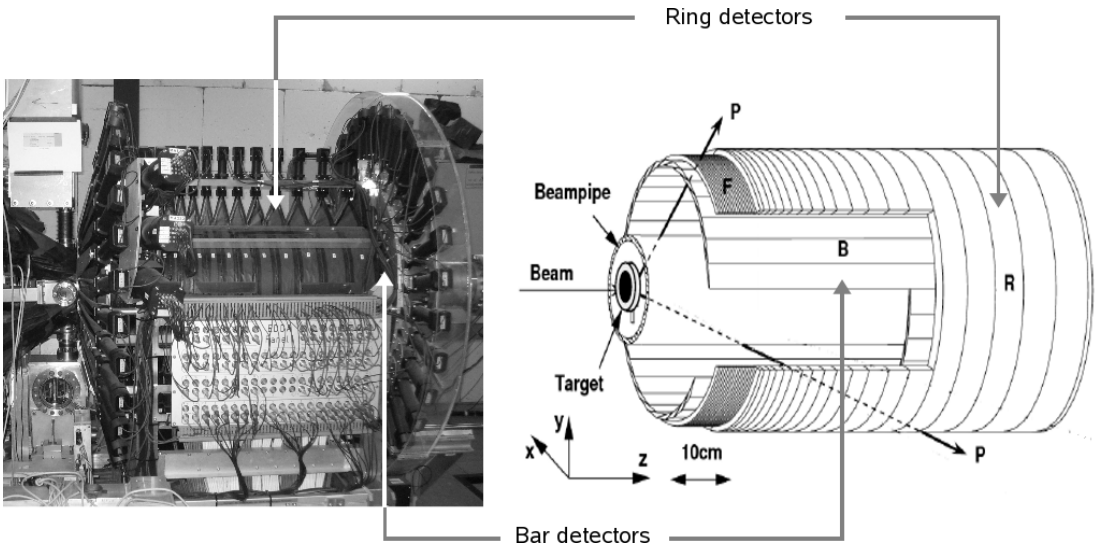

Figure 3.6: Photograph (left) and scheme (right) of the EDDA detector at COSY. The PMT scintillator detectors are visible in the photograph. The scheme on the right shows the three different layers that compose the detector: a fiber array, scintillator bar detectors and scintillator ring detectors.

Using EDDA as a polarimeter involves producing a reaction in its target with a known analyzing power. From the count rates in the scintillators the polarization can then be reconstructed. The EDDA target system consists of a carousel where six targets can be mounted and chosen from. For polarimetry, a thin carbon fiber with a thickness of a few μm is usually used. This fiber is rapidly inserted into the circulating beam. Because of the small geometrical cross section, a circulating beam can pass the detector many times without hitting the fiber. When it eventually hits it, the particle will scatters and be lost from the acceptance of the ring. As a consequence, the beam is extinguished in a few ms. Only very rarely a particle undergoes large angle nuclear scattering useful for polarimetry. The efficiency for this process is of the order of 10^{-6}.

3.4 Implications for a dEDM Polarimeter

From a survey of existing polarimeters and the physics processes involved it was concluded that a sensitive deuteron polarimeter for the dEDM experiment must be based on nuclear scattering. Existing polarimeters generally have a very low efficiency. Specially the ones used in storage rings measurements because very thin and small targets must be used. Single pass polarimeters occasionally display high efficiency due to the use of thick targets. These have the disadvantage of performing single-shot type measurements rather than a continuous monitoring, necessary for the dEDM experiment.

Continuous polarimetry of a stored beam is possible by slowly extracting the beam into a polarization analyzing detector. The extracted particles are lost from the experiment and can only be used to determine the beam polarization. The efficiency of the analyzer thus determines the overall efficiency of the system and should hence be as large as possible. High efficiency, meaning a high probability for nuclear scattering, can be obtained through the use of a thick target. The geometry of the setup used to measure the reaction products determines which part of the reaction space phase is probed and can be used to great effect in optimizing the efficiency.

Chapter 4

Novel Polarimeter Concept

The measurement of the deuteron EDM requires a polarimeter that can continuously track the evolution of the spin. It may not affect the spin evolution. The EDM signal is very small. Therefore the polarimeter must have great statistical sensitivity and little systematic sensitivity. In this chapter we present a novel concept for a highly efficient continuous polarimeter that meets these criteria. It merges the strengths of several existing polarimeter concepts. A schematic view of such a polarimeter is given in figure 4.

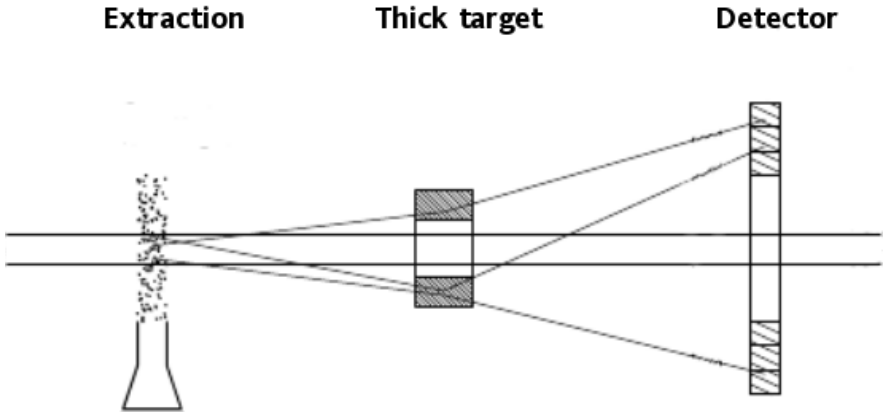

Figure 4.1: Scheme of a continuously monitoring dEDM polarimeter. The circulating deuteron beam passes a gas target where Coulomb scattering increases the beam emittance. The edge of the beam is intercepted at a thick analyzer target. Particles scattered over a large angle are registered in a segmented detector. [78]

Deuterons that are stored in the ring interact with a thin gas target. Due to the Coulomb interaction the average amplitude of the beam oscillations about the equilibrium orbit will increase. Those particles that have the largest oscillation amplitudes will be intercepted by the analyzer target. This target is designed to be the limiting aperture in the storage ring. The deuterons that miss the analyzer target thus stay in the ring. The probability for nuclear scattering in this target is enhanced by making it very thick. The spin dependence in nuclear scattering will result in an asymmetry in the reaction products. These products are detected in a segmented detection system that is able to resolve this asymmetry.
In the next sections, the three main elements of this concept, namely extraction method, analyzer target and particle detector will be discussed.

4.1 Extraction Method

Slow extraction from circular accelerators or stretcher rings is generally realized by resonant excitation of the horizontal and vertical oscillations about the stable orbit (betatron oscillations) [79, 80]. At resonance the displacement of a particle from the beam center slowly grows. The affected particles are further separated from the remaining beam by an electrostatic deflector or septum magnet. Long spill times are obtained by exciting non-linear resonances.
The displacement growth is fully determined by the layout of the magnetic elements of the storage ring. The original particle properties, i.e. its location in six dimensional beam phase space, can thus be strongly correlated with the time at which the particle will reach the extraction point. In a practical storage ring it is unavoidable that there is a correlation between the spin and beam evolution. This connection between time and beam phase-space may lead to a false EDM signal because the EDM signal is a time-dependent growth of the vertical polarization component. For the same reason scraping the outer edge of the beam by slowly steering the beam into an analyzer target is undesirable. A less deterministic sampling mechanism should be employed to probe the beam phase space more uniformly.
Two possible routes for random, i.e. non-deterministic, emittance growth were identified. The first is based on the interaction between the beam and residual

gas in the storage ring. The second employs random kicks. Both mechanisms were studied at COSY-Jülich and are presented below.

4.1.1 Extraction via Gas Interaction

Particles in a ring are naturally displaced from their equilibrium orbit due to the interaction with residual gas. By controlling the amount of residual gas in a ring, the emittance growth and thus the beam lifetime can be controlled. For this reason the background pressure in experimental storage rings is usually kept very low. Beam lifetimes of hours have been obtained for background pressures of 10^{-7} mbar [81]. In the dEDM experiment the goal is to extract the beam in 100 to 1000 s. Much higher gas pressure is then necessary. This can be accomplished in a controlled way using a gas jet.

Gas targets are frequently used for continuous polarization experiments in storage rings. Such targets have densities of the order of 10^{15} particles/cm^3 [82]. At such densities only a few particles will interact in a single pass of the beam. The predominant process affecting the interacting particles is Coulomb scattering of the atomic electrons which has a cross section of the order of hundreds of barns and is strongly peaked at small scattering angles below 5 degrees [83].

The deflection in a single pass through the gas target is randomly distributed. It is on average considerably smaller than the typical acceptance of the storage ring [84]. A particle may thus stay in the ring for many revolutions and interact many times with the gas target. Over time, a particle will perform a random walk in the (x, x', y, y') beam phase space. Here, x (y) represents the horizontal (vertical) spatial deviation and x' (y') the horizontal (vertical) angular deviation of the trajectory with respect to the equilibrium orbit. Eventually the particle will be intercepted by an aperture, in our case the analyzing target.[1]. If that happens, the particle is lost from the storage ring.

A gas target provides a uniform sampling method. Coulomb scattering only depends on the energy of the incoming particle. In the dEDM experiment the circulating deuteron beam is expected to have a momentum spread below one per mill. This energy dependence is therefore of no consequence. To obtain a

[1] This is a variant of the classical problem in statistics known as "the Gambler's ruin".

large deviation from the average beam position many interactions are necessary. The random walk also largely decouples the initial particle conditions from the moment it hits the analyzer target.

Exploratory studies of this extraction method have been performed at COSY-Jülich. A square aperture of 1.5 cm length was inserted at the location of EDDA (see figure 3.5). The opening of 20 by 15 mm of this aperture is much smaller than other apertures in the ring and thus defines the acceptance of the ring. Its dimensions were chosen to accommodate typical beam motion during injection and acceleration in COSY. The beam was carefully centered with respect to the aperture. For this the stored beam intensity was measured as a function of beam displacement. In normal operation of COSY the beam lifetime can be larger than one hour [80]. Placing the aperture into COSY did not noticeably change this.

The WASA pellet target was used to slowly heat the beam (see figure 3.5) [82]. The pellets are produced by breaking up a liquid jet into equally sized and spaced droplets, which are frozen by the injection into vacuum. The pellets have a diameter of 30 μm, a speed of about 60 m/s, and are produced at a rate of about 7×10^4 per second [82]. The density of frozen hydrogen or deuterium is 5×10^{15} atoms/cm^2.

For this study the gas target thickness was increased up to its maximum of 10^{14} nuclei/cm^3. During the observation time of several minutes no difference in beam lifetime was observed. Only when the beam would be initially positioned within a few mm of one of the carbon surfaces a decrease in beam lifetime could be observed. This indicates that the initial beam size is considerably smaller than the aperture. No beam losses will occur as long as the beam does not touch the aperture. How long this takes depends not only on the magnitude of the average angular deflection, but also on the distance between the edge of the injected beam and the aperture.

For further studies an extraction time of the order of 60 seconds was needed. For the used setup, with the beam centered at the analyzer target, the cluster gas target was too thin to introduce a visible difference. It is expected that the extraction time does not only depend on position of the beam with respect to the aperture, but also on the shape of the beam. Both are still unknown for the

dEDM experiment. This method of slow extraction was therefore not investigated in more detail.

4.1.2 Stochastic Slow Extraction

The interaction of the circulating beam and residual gas in the storage ring leads to a random walk through particle phase space. This desirable feature can also be accomplished in a more controlled way by using a kicker system fed with a noise signal. This method is known as stochastic slow extraction and was proposed by Simon van der Meer in 1978 [85]. It was first used to extract anti-protons from the Low Energy Anti-proton Ring (LEAR) at CERN in Geneva, Switzerland. More recent applications can be found at COSY [86] and the 70 GeV proton synchrotron at the IHEP in Protvino, Russia[87].
In essence, this method works the same as the one described before. In each passage of the kicker device the beam will experience a small random deflection. The accumulation of many such deflections will increase the betatron oscillation amplitude. An important difference compared to gas extraction is that all particles will experience the same kicker field and thus the same deflection. This can introduce a coherence in the betatron oscillations. Whether this coherence is important requires detailed beam simulations, which are outside of the scope of this thesis.
Also stochastic extraction has been tested at COSY. As in the gas extraction test, the beam was centered at the same square aperture. The electric corrector kicker that is part of the stochastic cooling setup was used to supply random kicks [88]. The device contains electrodes both in the horizontal and vertical direction. The voltage on the horizontal and vertical plates can be controlled independently. This makes it possible to set up horizontal, vertical or combined emittance growth.
A digital signal generator was used to create a band-width limited white noise spectrum (centered at 1.2 MHz with a 160 kHz bandwidth). This spectrum overlaps with the beat-nodes of the revolution frequency of COSY and the horizontal and vertical betatron frequencies (approximately 3.5 times the COSY revolution frequency of 880 kHz). The amplified signal can then be send to either the hor-

Table 4.1: Time and rate of maximum extraction and decay constant for $t = [30, 40]$ s for varying horizontal beam displacements at a fixed noise power of 1.4% on the horizontal kicker plates.

Δx [mm]	T_{max} [s]	R_{max} [kHz]	Decay Constant [s]
-4	0	8.65	6.9
-2	9	1.83	37.0
-1	16	1.23	46.5
1	19	1.12	48.7
2	19	1.17	55.9
4	7.5	1.95	29.5
6	0	4.76	14.4

izontal, the vertical or both pairs of electrodes without changing the settings of the signal generator.

By adjusting the gain of the amplifier the extraction time was varied. At 4% of the maximum power output 80% of the beam was lost during a 62 second beam store. For this test the vertical plates were connected. Similar results were obtained for the horizontal plates around 14% of the maximum power output.

In the gas extraction test it was found that the positioning of the beam had a large effect on the extraction rate. The effect of the positioning was studied in more detail using horizontal stochastic extraction. After injection and acceleration at the nominally centered position, the beam was moved sideways. The extraction rate was determined using the EDDA detector and by monitoring the circulating beam current. A detailed discussion of the experimental setup can be found in the next chapter. Data taking started 5 seconds after injection to avoid flashes in the counting rate due to transient effects in the beam when steerer magnets are switched on an off.

In fig. 4.2 the extraction rate is shown as a function of time in the store.

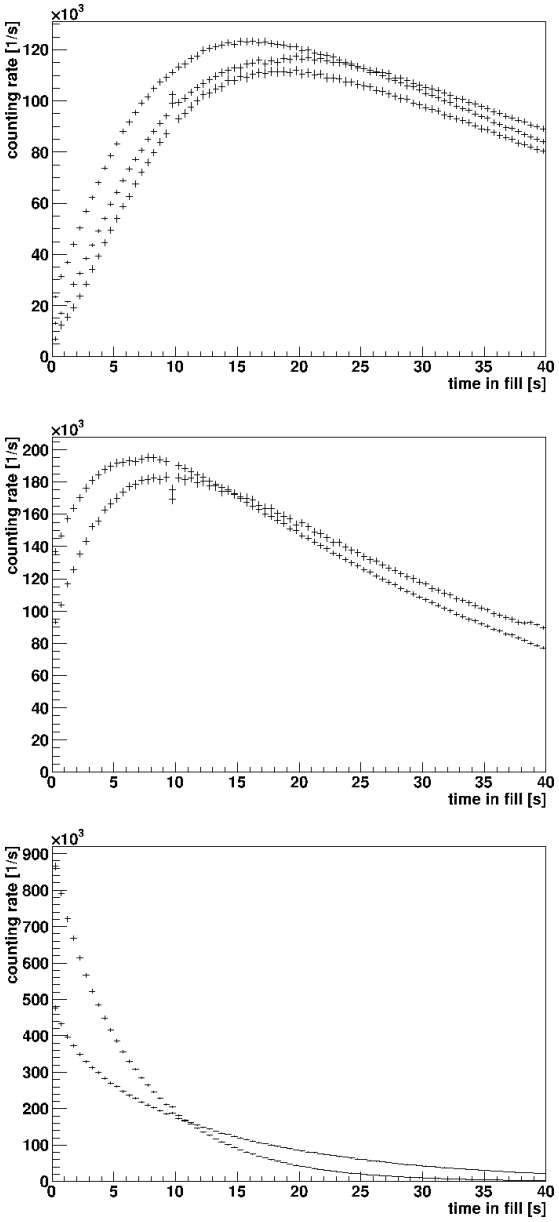

Figure 4.2: Beam extraction rate as a function of the time in store. For a centered beam (top panel), the extraction rate is at first linear. After reaching a maximum rate between 15 and 20 seconds it starts to decrease. Three different beam displacements are shown: -1, 1 and 2 mm. For a beam closer to the side of the target (middle panel) the extraction happens faster, reaching the maximum rate between 5 and 10 seconds. Two different beam displacements are represented: -2 and 4 mm. For a beam very close to the edge of the target (bottom panel) the extraction starts immediately and decreases exponentially. Two different beam displacements are depicted: -4 and 6 mm.

For a beam near the center of the target (displacement -1 to +2 mm) the extraction rate initially grows linearly. It reaches a maximum rate of 120 kHz near 15 to 20 seconds and then starts to decline. Displacing the beam further to the sides (displacement -2 and +4 mm) leads to a faster extraction. The maximum is reached between 5 to 10 seconds. The maximum extraction rate (200 kHz) is correspondingly higher. Moving the beam very close to the edge of the target (displacement -4 and +6 mm) leads to an instantaneous start of the extraction at an initial rate of 500 ($\Delta x = +6$ mm) to 900 kHz ($\Delta x = -4$ mm). The extraction rate falls off exponentially with a lifetime of 6.9 s or 14 s (with an error below 10 ms) for Δx of -4 and +6 mm, respectively. In tab. 4.1 all results are collected. These results support the earlier conclusion that the beam is small and does not fill the aperture at injection time.

4.2 Analyzer Target

The choice of the analyzer target is focused on three aspects: location in the ring; geometry; material composition.

4.2.1 Location

As described in the previous section, beam extraction is to take place by emittance growth, leading to the eventual interception of a particle by the analyzer target. The target should be placed at a location in the storage ring where the envelope of the betatron oscillations is large. At this location the effect of the angle kick provided by either the gas target or stochastic kicker is maximally visible in the displacement of a particle. In this way it becomes easier to make the analyzer target the defining aperture.
In the final dEDM experiment the location of the analyzer target should be optimized. For this detailed beam dynamics simulations of the final storage ring layout are necessary. This is beyond the scope of this work.
For our extraction and detector studies at COSY (see above and next chapters) we used the EDDA detector. Hence the target location was fixed by the existing facilities. At this location the beam has a waist, i.e. it has maximal divergence

and a (local) minimum in the betatron oscillation envelope. Nevertheless, the analyzer target was still the limiting aperture of the storage ring. This was shown by finding the maximum beam excursion at the location of the target for which no noticeable beam losses occurred with and without the analyzer target. With the target in place, the beam can be moved horizontally by approximately $\pm 5\,\mathrm{mm}$ and $\pm 3.5\,\mathrm{mm}$ before losses occur. Without target no losses could be observed over twice that range. This range was limited by the magnet power supplies used to create local displacements.

4.2.2 Geometry

The original concept contained a tube shaped target as depicted in figure 4. Particles that hit the target would undergo large angle nuclear scattering. Those that do not and emerge at the back end of the target are sufficiently perturbed due to, e.g., multiple Coulomb scattering and energy loss, that they can no longer be stored and are lost elsewhere in the ring. All the particles that go through the hole remain in the ring for the next measurement.

Optimization of the target geometry concerns mostly the thickness of the target along the beam. The thickness of the target determines the probability for undergoing a nuclear reaction useful for measuring the beam polarization. It thus directly affects the efficiency of the polarimeter. To first order the probability for undergoing a rare reaction is proportional to the thickness of the target. However, because of energy loss and other reactions, optimization becomes a highly non-linear problem. It will be discussed in detail in the next chapter.

In ultra slow extraction the displacement of the particles from the beam center will grow very slowly. As a consequence the particles will hit the front face of the target very close to its inner edge. The distance to the edge cannot exceed the increase in betatron amplitude *per turn*. Maximum depth is obtained by those particles that graze the inner surface in the last few turns prior to the one in which it hits the target. An order of magnitude estimate of the step size per turn δx can be made from the time needed to reach maximum extraction (see table 4.1). As long as there is no significant extraction the *variance* in x of the injected

beam will grow linearly with time as $\sigma = \sqrt{n}\delta x$. From this,

$$\delta x = \frac{\Delta x}{\sqrt{f_{\mathrm{COSY}} T_{max}}} \simeq 1\,\mu\mathrm{m} \tag{4.1}$$

with $f_{\mathrm{COSY}} = 880\,\mathrm{kHz}$ the revolution frequency of the deuteron beam in COSY. Scattering will thus take place from the inner $1\,\mu$m thick layer of the target. The interaction vertex is thus very well defined. Most importantly it does not depend on the beam and is fully determined by the mechanical properties of the target. In each dimension only one of the two edges (left or right, top or bottom) can be reached. This is because the particles oscillate about the equilibrium orbit of the storage ring. The *minimum* distance of the beam center to either side determines the *maximum* oscillation amplitude. The oscillation frequency in COSY is about 3.5 times the revolution frequency. It thus takes only a few turns to reach both the maximum left and right (or top and bottom) deviation. In these few turns, the increase of the oscillation amplitude is insufficient to cover typical misalignments of the beam with respect to the target. An "L" shaped target would thus suffice. Keeping a tube has the advantage that by shifting the beam position extraction on either side can be selected without changing any hardware.

4.2.3 Material

The dEDM polarimeter concept relies on the spin dependence of nuclear scattering. Hence the target material must be selected based on the reaction cross section and the analyzing powers. In the next chapter the choice of target material is discussed in detail.

This selection cannot be made without considering the acceptance of the detecting system. Several engineering constraints should be considered as well. As shown above the penetration depth of the particles hitting the target is only of the order of $1\,\mu$m. This means that the target material must be solid under normal operating conditions. Liquid or gaseous materials would need a container. The wall of this container would have to be substantially thinner than the typical penetration depth, which is practically impossible.

The target is placed directly into the storage ring. This means that it must be vacuum compatible. It may not evaporate nor show excessive out-gassing.

A final condition is imposed by the experimental method. The spin precession rate of the particle in the ring is extremely sensitive to perturbations in the electric and magnetic field. It should thus be avoided that the target charges up and creates a local electric field. Practically this means that the target should be made out of conducting material and be grounded.

4.3 Detector

The ideal detector fully reconstructs all the (nuclear) reactions occurring at the analyzer target. This includes the reconstruction of the four momentum of the incoming and scattered particles as well as the interaction vertex. Impressive examples of detectors capable of this can be found for example at RHIC (Relativistic Heavy Ion Collider) at Brookhaven National Laboratory, LEP (Large Electron-Positron collider) at CERN Geneva and SLAC (Standford Linear Accelerator Center). Such complex devices are not feasible for the dEDM experiment.
The minimal functionality of a polarimeter based on nuclear scattering is the reconstruction of the azimuthal angle. The polarization of the incoming beam manifests itself as a variation of the scattering rate with this angle (see section 3.2). For a point target such a variation would be detectable using a detector segmented along the azimuth placed at some distance from the target. In our case an extended target is used. This implies that the detector should be placed at a distance from the target which is large compared to the target dimensions. The IBP at KVI (see section 3.3.2) is an example of such a configuration.
Reaction cross sections and analyzing powers strongly depend on the scattering angle θ. The θ acceptance and segmentation of the detector can be used to optimize the performance of the detector. Scattering angles with high cross section and low analyzing power can for example be excluded by limited the acceptance. By segmenting the detector data for angles with large but opposite analyzing powers do not have to be combined avoiding lower analyzing power. Alternatively tracking devices such as wire chambers could be used. In POMME (see section 3.3.1) wire chambers were placed before and after the scattering target to measure the azimuthal and scattering angles.

In a similar way the energy acceptance and resolution can be used to include or exclude specific reaction channels. A detector capable of particle identification would make it possible to further optimize the selection of contributing reactions. For example, the iron absorber in POMME limits the energy acceptance and the phoswitch construction in the IBP makes particle identification possible.
In the projected dEDM experiment the polarimeter will have to endure a very high counting rate. It is projected that around 10^{13} particles will be stored in the ring. The majority of these particles will be extracted over 1000 s which amounts to an instantaneous rate of the order of 10^{10}particles/s at the analyzer target. The goal is to reach a polarimeter efficiency of the order of one percent. The detector rate may than be as high as 10^{8}particles/second. This places limitations on the technology that can be employed and the amount of information that can be recorded. Consequently, the detector may have to act as a *black box* detector, in the sense that it integrates or averages over some of the possible observables, retaining a minimum of information.
Three different detector types are being studied for use in the dEDM experiment. For the work described in this thesis a segmented scintillator detector was used. Other detector studies are focused on the use of tracking detectors based on Multigap Resistive Plate Chambers (MRPC) [89] and Micro Pattern Gaseous Detectors (MICROMEGAS) [90].

Chapter 5

Polarimeter Sensitivity

There are three quantities of importance for the optimization of a polarimeter.

1. The efficiency η of the polarimeter is defined as the ratio between the number of particles used for the analysis and the total number of particles in the experiment.

2. The effective analyzing powers that must be known with sufficient accuracy to obtain the absolute polarization and that must be large enough to reduce sensitivity to systematic effects.

3. The figure-of-merit FOM that establishes the statistical precision with which the polarization can be measured.

In this chapter the optimization of the statistical sensitivity and the efficiency is discussed. The sensitivity to systematic uncertainties is discussed in the next chapter.

5.1 Signal Definition

The elastic scattering cross section for a polarized spin-1 particle such as the deuteron of an unpolarized target was introduced as (see equation 3.25 and figure

3.1)

$$\begin{aligned}\frac{d\sigma}{d\Omega}(\theta,\phi,\beta) = \frac{d\sigma_{unp}}{d\Omega}(\theta)\,[1 \quad & + 2\frac{\sqrt{3}2}{p}_V \sin\beta\,\sin\phi\, iT_{11}(\theta) \\ & + \frac{1}{2\sqrt{2}}\,p_T\,(3\cos^2\beta - 1)\,T_{20}(\theta) \\ & - 2\sqrt{\frac{3}{2}}\,p_T\,\sin\beta\,\cos\beta\,\cos\phi\,T_{21}(\theta) \\ & + 2\frac{\sqrt{3}}{4}\,p_T\,\sin^2\beta\,\sin 2\phi\,T_{22}(\theta)\Big]\end{aligned} \tag{5.1}$$

where p_V and p_T stand, respectively, for the vector and tensor polarizations and iT_{11} and T_{2m} the corresponding analyzing powers. $d\sigma_{unp}/d\Omega$ represents the cross section for unpolarized scattering.

We assume a purely vector polarized ($p_T = 0$) incoming beam with I particles per second impinging on a thin target with thickness ρ nuclei per unit area. The resulting counting rate $N^{(i)}$ of a detector element i with solid angle $\Omega^{(i)}$ is given by

$$\begin{aligned} N^{(i)} &= I\rho \textstyle\int_{\Omega^{(i)}} \frac{d\sigma}{d\Omega}(\theta,\phi,\beta)d\Omega \\ &= I\rho \int\limits_{\Omega^{(i)}} \frac{d\sigma_{unp}}{d\Omega}(\theta)d\Omega + \sqrt{3}p_V \sin\beta \int\limits_{\Omega^{(i)}} \left(\frac{d\sigma_{unp}}{d\Omega}(\theta) iT_{11}(\theta)\sin\phi\right) d\Omega \\ &= N_0^{(i)}\left[1 + \sqrt{3}p_V \sin\beta A_0^{(i)}\right], \end{aligned} \tag{5.2}$$

The variables $N_0^{(i)}$ and $A_0^{(i)}$ are defined as

$$N_0^{(i)} = I\rho \int\limits_{\Omega^{(i)}} \frac{d\sigma_{unp}}{d\Omega}(\theta)\sin\theta d\theta d\phi \tag{5.3}$$

$$A_0^{(i)} = \frac{1}{N_0}\int\limits_{\Omega^{(i)}} \left(\frac{d\sigma_{unp}}{d\Omega}(\theta) iT_{11}(\theta)\sin\phi\right)\sin\theta d\theta d\phi \tag{5.4}$$

Different analysis techniques have been employed to extract polarizations and their associated analyzing powers from the measured rates. This includes taking linear asymmetries, the cross ratio methods, fitting harmonics and the method of moments . These methods mainly differ in their robustness against systematic effects. In this section we only consider the most frequently applied linear asymmetry method because the statistical powers of these methods are all similar. In the dEDM experiment a beam of longitudinally vector polarized deuterons will be injected into the storage ring. For such a beam $\beta = 0$, $p_T = 0$ and $|p_V|$ is as large as possible. A non-zero EDM leads to the precession of the spin out of the plane of the storage ring and a slow growth of β (see Chapter 2).

The rates for two similar detectors at identical scattering angle θ but centered at $\phi = -\pi/2$ and $\phi = \pi/2$, i.e. left and right of the beam at the $\hat{x}$-axis, will be affected in a different way. The detector centered at $\phi = \pi/2$ has $\sin\phi \simeq 1$, so that

$$N\left(\phi = \frac{\pi}{2}\right) = N_0\left[1 + \sqrt{3}p_V \sin\beta A_0\right], \tag{5.5}$$

whereas the detector at $\phi = -\pi/2$ has $\sin\phi \simeq -1$, and thus

$$N\left(\phi = -\frac{\pi}{2}\right) = N_0\left[1 - \sqrt{3}p_V \sin\beta A_0\right]. \tag{5.6}$$

The relative asymmetry $\mathcal{A}$ in these two rates is a measure of $p_V A_0$ and of p_V for the case when A_0 is known,

$$\mathcal{A} \equiv \frac{N(\frac{\pi}{2}) - N(-\frac{\pi}{2})}{N(\frac{\pi}{2}) + N(-\frac{\pi}{2})} = \sqrt{3}p_V A_0 \sin\beta. \tag{5.7}$$

The scattering frame and the laboratory frame do not necessarily coincide. Usually the z-axes, defined by the incoming beam, are aligned. The orientation of the spin, which defines the y axis in the scattering frame, then defines a rotation about the z-axis of the scattering plane with respect to the laboratory frame. The azimuthal angle ϕ of a detector in the *laboratory frame* is then shifted by $\Delta\phi$ compared to the corresponding angle in the *scattering plane*. $\Delta\phi$ is the enclosed angle between the spin plane and the laboratory $y - z$ plane.

The rate asymmetry $\mathcal{A}_{LR}$ of a pair of detectors placed at $\phi = \pi$ (right) and $\phi = 0$ (left) in the laboratory frame is sensitive to the vertical component (in the laboratory frame) of the vector polarization and its associated analyzing power.

$$\mathcal{A}_{LR} \equiv \frac{L - R}{L + R} = p_V A_0 \sin\beta\cos\Delta\phi \equiv p_V^y\, A_0 \quad \rightarrow \quad p_V^y = \frac{\mathcal{A}_{LR}}{A_0}. \tag{5.8}$$

Here L (R) represents the rate in the left (right) detector. The size of p_V^y will uniformly increase during one store due to the interaction of the EDM with the motional electric field. The growth rate is proportional to the EDM.

Similarly the relative ratio $\mathcal{A}_{DU}$ of the counting rates in a detector pair placed above and below the beam ($\phi = -\pi/2$) and $\phi = \pi/2$) is sensitive to the horizontal polarization component,

$$\mathcal{A}_{DU} \equiv \frac{D - U}{D + U} = \sqrt{3}p_V A_0 \sin\beta\sin\Delta\phi \equiv p_V^x\, A_0 \quad \rightarrow \quad p_V^x = \frac{\mathcal{A}_{DU}}{A_0}, \tag{5.9}$$

where D and U stand of the rates in the "down" and "up" detector, respectively. Expressions 5.8 and 5.9 describe the y and x component of the vector polarization, based on empirical facts.

5.2 Efficiency and Figure-of-merit

The efficiency of a detector element is defined as the ratio between the number of scattered particles used for polarimetry and the number of particle stored in the experiment. For a single detector element the efficiency can be calculated as

$$\eta^{(i)} = \frac{N_0^{(i)}}{I} = \rho \int\limits_{\Omega^{(i)}} \left(\frac{d\sigma}{d\Omega}_{unp} \right) d\Omega. \tag{5.10}$$

The efficiency of a detector composed of many elements is then defined as the sum over all individual efficiencies,

$$\eta = \sum_{i \in \text{elements}} \eta^{(i)} = \rho \int\limits_{\Omega_{total}} \left(\frac{d\sigma}{d\Omega}_{unp} \right) d\Omega \tag{5.11}$$

where $\Omega_{total} = \sum_{i \in \text{elements}} \Omega^{(i)}$. The efficiency is not sufficient to optimize the performance of a polarimeter because not all detector elements have equal sensitivity to the polarization.
The uncertainty in the counting asymmetry is given by

$$\sigma^2_{\mathcal{A}_{LR}} = 4\frac{L^2\sigma_R^2 + R^2\sigma_L^2}{(L+R)^4} = 4\frac{LR}{(L+R)^3} \tag{5.12}$$

Using the rates defined above, this can be written as

$$\sigma^2_{\mathcal{A}_{LR}} = 4\frac{N_0^2\left[1 - 3(p_V^y)^2 A_0^2\right]}{8N_0^3} \simeq \frac{1}{2N_0}. \tag{5.13}$$

This holds for small values of the second term in the numerator as will happen in the dEDM experiment. The uncertainty on p_V^y then becomes

$$\sigma^2_{p_V^y} = \frac{\sigma^2_{\mathcal{A}_{LR}}}{A_0^2} = \frac{1}{2N_0 A_0^2} \tag{5.14}$$

The denominator is referred to as the figure-of-merit. It depends on both the scattering cross section and the detector acceptance.

The detector acceptance is chosen to provide a good statistical basis for the polarization measurement. When choosing the best angular range a balance between the large cross sections at small angles and the large analyzing powers at larger angles must be found. It then becomes a trade-off between higher counting rate and sensitivity to the vector polarization p_V.

5.3 Black Box Detector

So far only elastic scattering from a thin target has been considered. As mentioned in the previous chapter, the closest to ideal polarimeter is one that behaves as a black box, integrating and averaging over some of the possible observables and being inclusive concerning different reaction processes and particle species. The polarimeter concept discussed in chapter 3 is only sensitive to the impact position of charged particles. Hence all reactions with charged particles in the final states should be considered. In the energy range for the dEDM experiment the most important ones are

- Elastic deuteron scattering: $d + \text{nucleus} \rightarrow d + \text{nucleus}$
- Inelastic deuteron scattering to discrete states: $d + \text{nucleus} \rightarrow d + \text{nucleus}^*$
- Inelastic deuteron scattering to continuum states: $d + \text{nucleus} \rightarrow d + \text{debris}$
- Deuteron breakup: $d + \text{nucleus} \rightarrow p + n + \text{nucleus}$.

Not all these reactions are equality suitable for polarimetry. In our configuration the energy and angular acceptance can be used to optimize the figure-of-merit. The dependence of the cross sections and analyzing powers on the energy of the incoming deuteron must be taken into account as well. When using a thick target the deuteron energy gradually decreases. In this case the detector rate cannot be calculated as the product between the beam rate and the target thickness.
The inclusive expression for the differential cross section $\Sigma(\theta, \phi)$ for detecting a single particle in deuteron scattering is given by

$$\Sigma(\theta,\phi) \equiv \sum_{s \in \text{species}} \left[\int_{E^{(s)}_{out,min}}^{E^{(s)}_{out,max}} \frac{1}{d} \int_{x=0}^{d} \frac{d^2\sigma^{(s)}}{d\Omega dE^{(s)}_{out}} (\theta, \phi; E_{in}(x))\, dx \right] . \tag{5.15}$$

Here $E_{in}(x)$ is the energy of the deuteron when it scatters. The depth into the target at which the scattering takes place is given by x. The maximum depth is the target thickness given by d. The energy of the outgoing particle is denoted by $E_{out}^{(s)}$. The minimum and maximum detectable energy for a given species are $E_{out,min}^{(s)}$ and $E_{out,max}^{(s)}$. For inelastic channels double-differential cross sections $d^2\sigma^{(s)}/d\Omega dE_{out}$ must be employed to account for the energy lost to the undetected final state. For the elastic channel or for a fixed energy E_{out} the energy dependence reduces to a delta-function.
After summing over all the possible physical species and integrating over the particle acceptances, the general expression for the effective cross section is still of the form,

$$\Sigma(\theta,\phi) = \hat{\sigma}_{unp}(\theta)\left[1 + 2\ it_{11}\ i\hat{T}_{11}(\theta) + t_{20}\ \hat{T}_{20}(\theta) + 2\ t_{21}\ \hat{T}_{21}(\theta) + 2\ t_{22}\ \hat{T}_{22}(\theta)\right]. \tag{5.16}$$

Here the $\hat{}$ is used to indicate that the cross section and analyzing powers are integrated and averaged quantities. They can be used directly to obtain the efficiency or figure-of-merit as defined above.

5.4 Choice of Target Material

The complexity of equation. 5.15 prohibits straightforward selection of a suitable target nucleus and thickness. Moreover not all cross sections and analyzing powers are known. For the selection of a suitable target material we limited ourselves to the elastic channel.
Comparing elastic scattering for different elements, the most prominent sensitivity to polarization is found for nuclei with atomic number $A < 50$ and center-of-mass scattering angles θ^{CM} larger than about 50° [91]. Large analyzing powers ($A > \frac{1}{2}$) were observed for scattering angles above $\theta^{CM} > 90°$. In figure 5.1 the cross sections and analyzing powers are shown for various target nuclei for an incoming deuteron energy of 56 MeV.

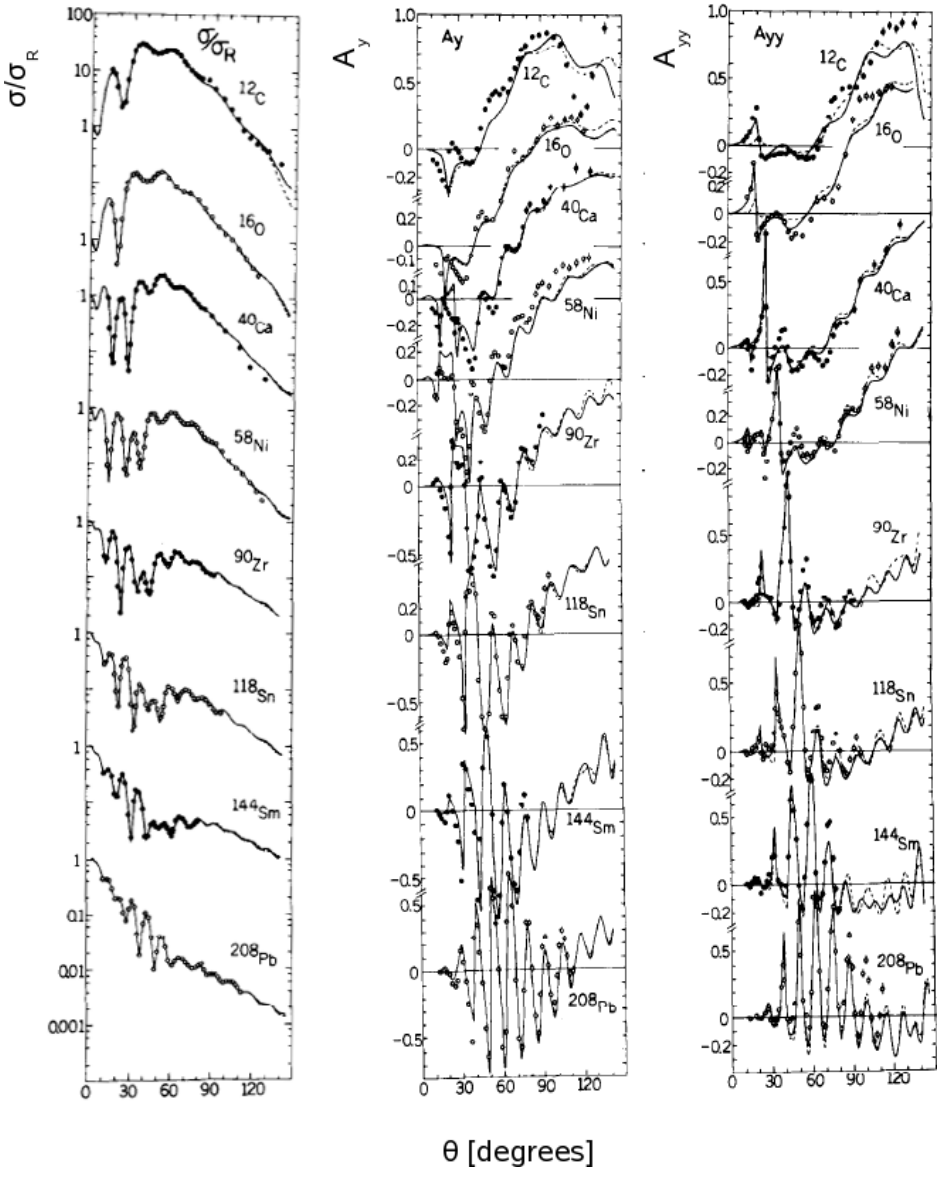

Figure 5.1: Differential cross section σ relative to the Rutherford cross section σ_R (left), vector analyzing power A_y (center) and tensor (right) analyzing power A_{yy} for a variety of target species as a function of the center-of-mass scattering angle for 56 MeV deuterons. The solid and dashed curves represent optical model calculations [91]. Counting rates, vector analyzing powers and figures-of-merit for center-of-mass scattering angles for the data represented here are listed in table 5.1.

Table 5.1: Counting rate, vector analyzing power and figure-of-merit for center-of-mass scattering angles of 60 and 90 degrees for the data shown in figure 5.1. The rate was calculated multiplying the cross section ratio σ/σ_R by $Z^2/sin^4(\theta/2)$ to account for the target and angle dependence in the Rutherford cross section and $\sin\theta$ to account for the phase space integration.

element	Z	$\frac{\sigma}{\sigma_R}Z^2/sin^4(\theta/2)$	Ay	FOM	$\frac{\sigma}{\sigma_R}Z^2/sin^4(\theta/2)$	Ay	FOM
		$\theta^{CM} = 60°$			$\theta^{CM} = 90°$		
^{12}C	6	$1.1 \times 10^{+4}$	0.41	$1.9 \times 10^{+3}$	$6.9 \times 10^{+2}$	0.87	$5.2 \times 10^{+2}$
^{16}O	8	$7.9 \times 10^{+3}$	0.30	$7.2 \times 10^{+2}$	$4.7 \times 10^{+2}$	0.82	$3.2 \times 10^{+2}$
^{40}Ca	20	$7.5 \times 10^{+3}$	0.23	$3.9 \times 10^{+2}$	$6.6 \times 10^{+2}$	0.67	$2.9 \times 10^{+2}$
^{58}Ni	28	$9.1 \times 10^{+3}$	0.08	$6.5 \times 10^{+1}$	$7.2 \times 10^{+2}$	0.70	$3.6 \times 10^{+2}$
^{90}Zr	40	$5.3 \times 10^{+3}$	−0.03	$4.2 \times 10^{+0}$	$7.0 \times 10^{+2}$	0.41	$1.2 \times 10^{+2}$
^{118}Sn	50	$3.1 \times 10^{+3}$	−0.56	$9.5 \times 10^{+2}$	$4.7 \times 10^{+2}$	0.15	$1.1 \times 10^{+1}$
^{144}Sm	62	$1.4 \times 10^{+3}$	0.08	$8.6 \times 10^{+0}$	$6.3 \times 10^{+2}$	0.04	7.8×10^{-1}
^{208}Pb	82	$1.2 \times 10^{+3}$	−0.73	$6.3 \times 10^{+2}$	$2.3 \times 10^{+2}$	0.19	$8.4 \times 10^{+0}$

For heavy nuclei ($A > 40$), the analyzing power varies rapidly with scattering angle, as shown in figure 5.1. Over the extended angular acceptance foreseen for the dEDM polarimeter the average analyzing power would be reduced leading to a lower sensitivity. These rapid variations are further washed out by the deuteron energy spread caused by the use of a thick target. For medium-weight nuclei $A \sim 10 - 40$, the variations with scattering angle are significantly smaller. At larger scattering angles the analyzing powers approach their theoretical maxima.

An advantage for the lower A nuclei is the angular dependence of the cross section. For smaller A the cross section is larger at larger angles, where the vector analyzing power is also larger. The figure of merit will thus be better (see figure 5.1). From these observations it was concluded that a light target ($A < 10$) would be the most suitable one.
Besides an optimal figure-of-merit, also construction requirements need to be taken into account (see chapter 3). This includes mechanical stability, machinability, electrical conductivity and vacuum compatibility. Of the different mate-

rials graphite (carbon) meets most of the requirements. The cross section and analyzing powers for scattering polarized deuterons of carbon are also favorable. It is thus concluded that carbon is the best suited material for the analyzer target.

5.5 Deuteron Induced Scattering Database

Further optimization of the polarimeter requires a description of the scattering cross sections and analyzing powers contained in equation. 5.15. An important part of the development of the deuteron EDM polarimeter is the construction of data-driven models.

5.5.1 Elastic Scattering

Several polarized elastic deuteron scattering experiments have been performed in the energy range of operation of the deuteron EDM polarimeter (250 MeV and below). Table 5.2 lists the available data sets.

Table 5.2: Beam energy and covered scattering angle range for deuteron on carbon elastic scattering available in literature.

Kinetic energy	$\theta[^\circ]$	Reference
45 MeV	31 - 68	Osaka [92]
49 MeV	34 - 68	Osaka [92]
56 MeV	26 - 75	Osaka [92]
65 MeV	34 - 72	Osaka [92]
70 MeV	34 - 73	Osaka [92]
80 MeV	24 - 64	KVI [93]
110 MeV	15 - 58	KVI [93]
133 MeV	15 - 40	KVI [93]
200 MeV	4 - 30	Osaka [94]
270 MeV	4 - 37	RIKEN [95]

In figure 5.2 the cross sections are shown as a function of scattering angle. The corresponding vector analyzing powers are shown in figure 5.3. The data sets

at 80, 110 and 133 MeV were collected at KVI using the In-Beam Polarimeter (IBP),[73] and Big Bite Spectrometer BBS [96] detectors. The BBS setup is described extensively elsewhere[96]. The experimental setup used with the IBP is described in the next chapter.

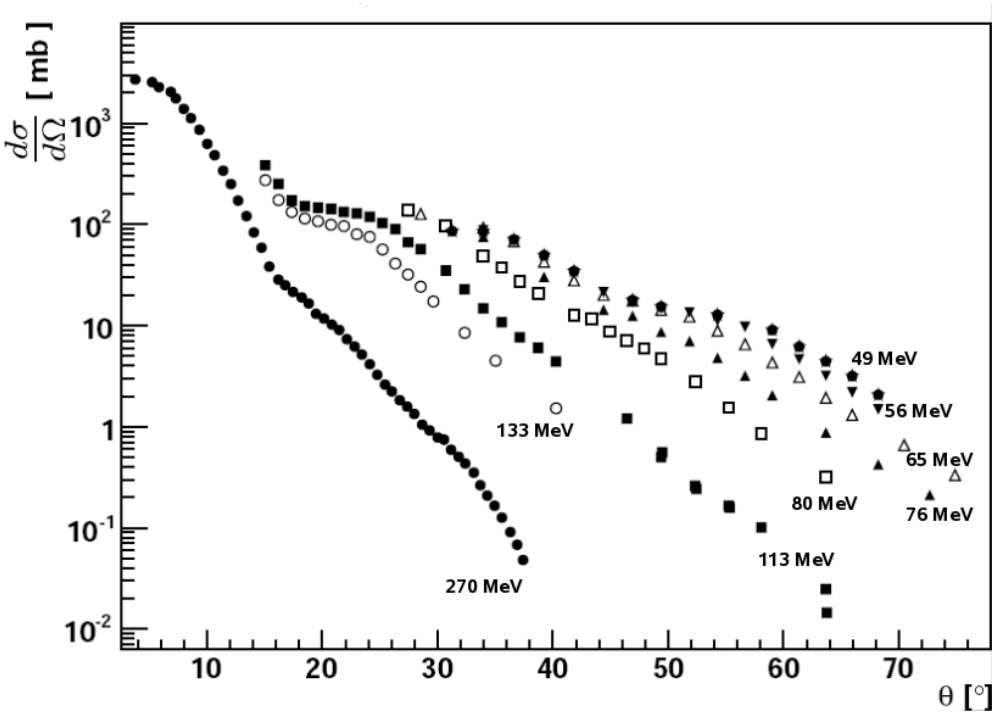

Figure 5.2: Available cross section data for deuteron on carbon scattering as a function of laboratory scattering angle.

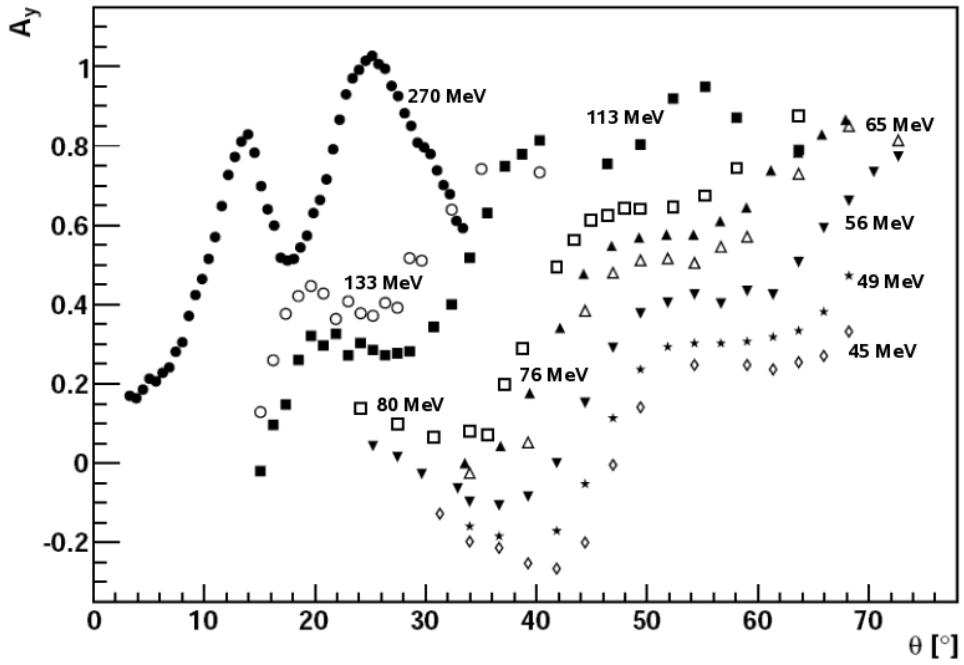

Figure 5.3: Available analyzing power data for deuteron on carbon scattering as a function of laboratory scattering angle .

5.5.2 Inelastic Scattering and Deuteron Breakup

In the literature very little data is available for deuteron induced in-elastic scattering and transfer and pick-up reactions. Only a single data set was found for proton production on carbon for a beam energy of 100 MeV [97].
To fill the gap between 80 and 200 MeV, experiments have been carried out at KVI-Groningen using the local In-Beam Polarimeter (IBP) [73]. The cross sections and analyzing powers for deuteron on carbon scattering were measured for an incoming deuteron energy of 76, 113 and 133 MeV. Scattered particles were measured across a broad energy and angle range through the use of a pair of ΔE-E telescopes (consisting of an assembly of scintillator plus NaI) in conjunction with the IBP. The ΔE-E telescopes were placed in the horizontal plane on the left and right sides of the IBP. They replace the usual phoswich detectors, which were not thick enough to stop the highest energy protons.

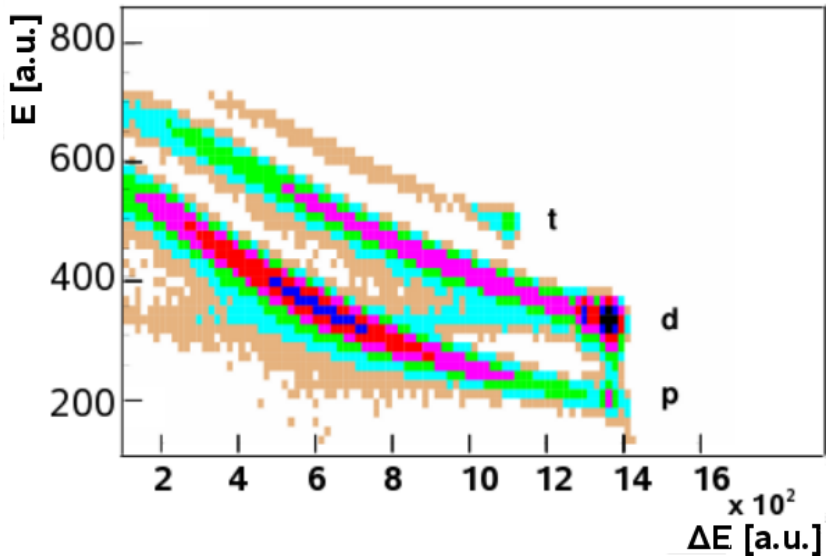

Figure 5.4: Particle identification through E-ΔE with xyz identification. The different bands correspond to protons (p), deuterons (d) and tritons (t). The most intense feature is the deuteron elastic scattering. The plot represents data taken at 113 MeV and a scattering angle of 27 degrees.

The telescopes were moved to scattering angles between 18° and 68°. They were placed symmetrically for the measurements of the vector analyzing power through

a left-right asymmetry. A carbon target with a thickness of 10 mg/cm^2 was used. The polarization of the beam was obtained independently from elastic deuteron-proton scattering using a CH_2 target. For this the IBP 45 degrees detector arms were used.
The use of a 5 mm thick scintillator in front of the NaI crystal made it possible to distinguish deuterons from protons and other charged particles in the final state (see figure 5.4).

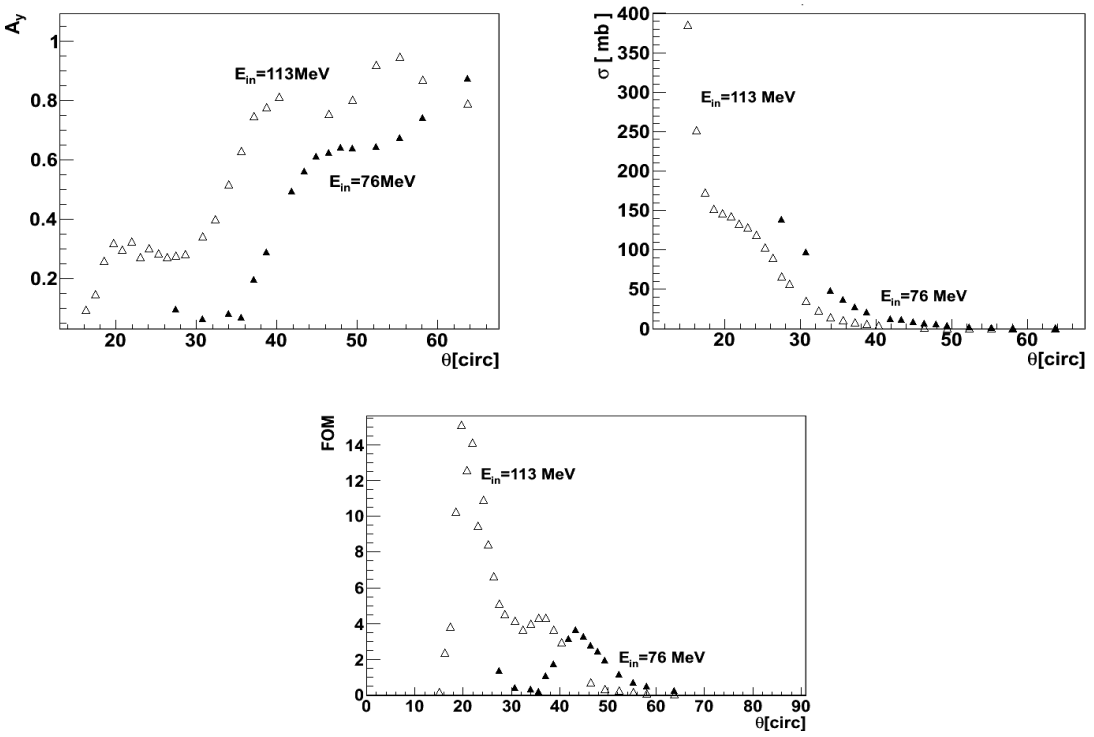

Figure 5.5: Angular distributions of the analyzing power, cross section and figure-of-merit for deuteron elastic scattering from carbon at 76 and 113 MeV.

From the energy deposit in the NaI the particle energy was reconstructed. In figure 5.5 the angular distribution of the cross section, vector analyzing power and figure of merit is shown for deuteron beam energies of 76 and 113 MeV. The cross section was integrated over 5 MeV bins in excitation energy E_x. The energy resolution of the NaI was sufficient to distinguish elastic scattering from inelastic scattering to the two lowest lying excited states in ^{12}C at 4.44 and 10 MeV.
The measurement was also extended into the continuum range. In figure 5.6 a selection of the results is shown. Not only the elastic channel has a significant analyzing power and cross section, but also the inelastic ones to discrete channels. The continuum cross sections are integrated over 5 MeV wide energy bins.

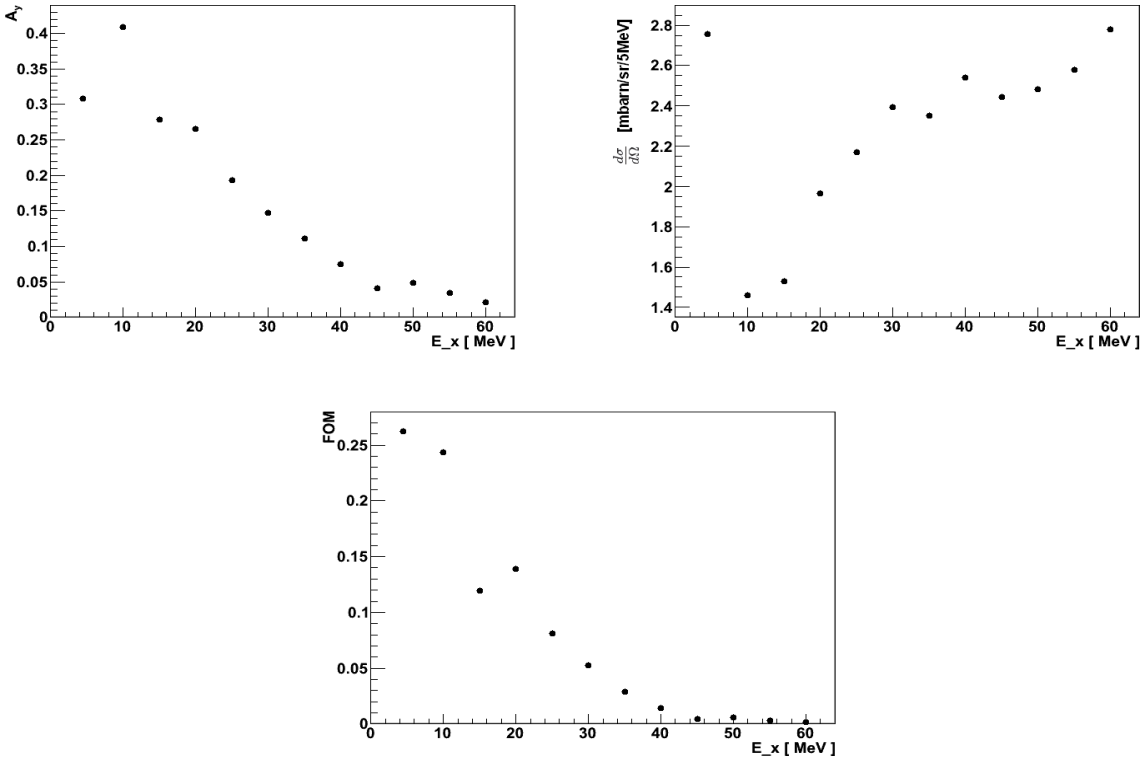

Figure 5.6: Analyzing power A_y, differential cross section $\frac{d\sigma}{d\Omega}$ and figure-of-merit FOM for deuteron on carbon scattering at 133 MeV for a scattering angle of 33°.

Together with the deuterons the most prominent other detected particles are protons. Most originate from proton breakup although also discrete states in

^{13}C can be discerned. The same procedure as mentioned in terms of excitation energies was applied to the protons. The results are shown in figure 5.7.
The large peak in the cross section originates from deuteron breakup. Deuteron breakup tends to suppress spin dependence as evidenced by the small analyzing powers. It is thus important to make sure that these protons do not fall within the acceptance of the polarimeter. This issue will be addressed at a later stage in this chapter.

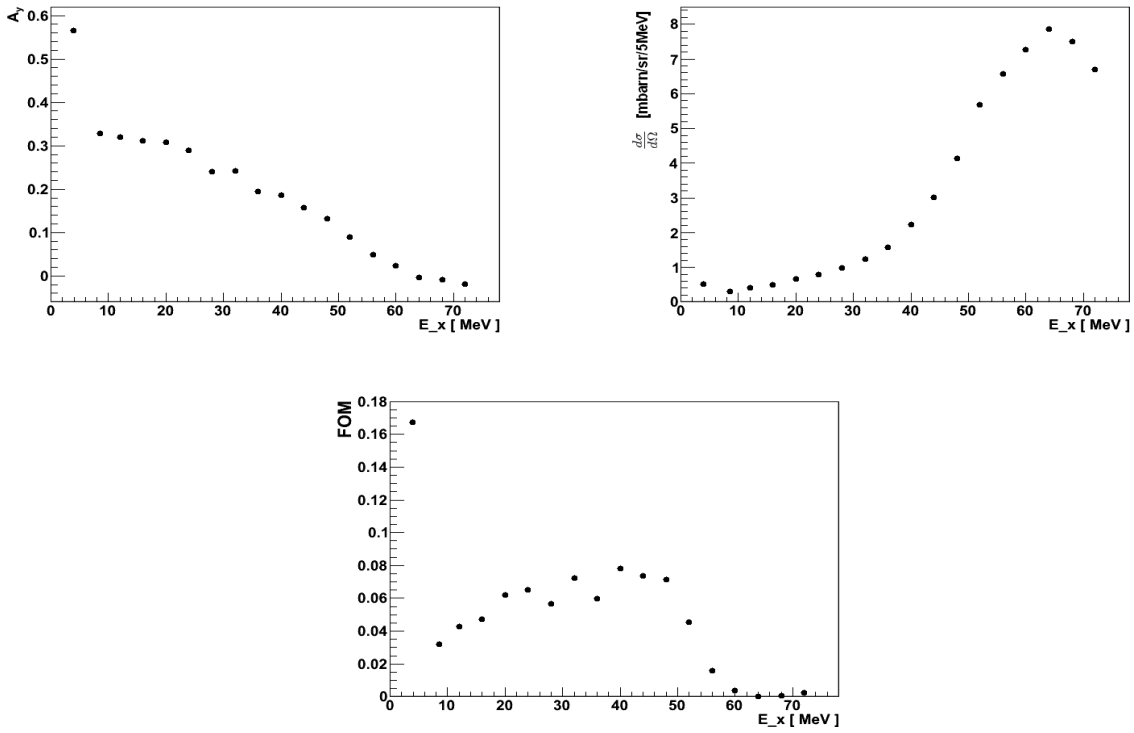

Figure 5.7: Analyzing power A_y, differential cross section $\frac{d\sigma}{d\Omega}$ and figure-of-merit FOM for breakup protons from deuteron on carbon scattering at 133 MeV for a scattering angle of 33°. The cross section was integrated over 5 MeV bins in excitation energy E_x.

5.6 Phenomenological Model

For quantitatively meaningful studies of the figure-of-merit and systematic effects it is important to reproduce all dominant features in the cross section and analyzing powers (see section 1.2). This includes the diffraction pattern visible in the angular dependence of the cross section. This pattern is present at all energies. At higher energies it is more compressed towards small scattering angles, whereas it is more stretched at lower energies. This energy dependence complicates the parametrization. A large part of the energy dependence can be eliminated by plotting the cross section as a function of momentum transfer calculated as

$$q = |\vec{p}_{in} - \vec{p}_{out}|, \tag{5.17}$$

where $\vec{p}_{in}$ and $\vec{p}_{out}$ represent the incoming and outgoing momentum of the deuteron. At all energies a similar pattern is present despite some being more compressed than others (see figure 5.8).
Using this data a smooth 2D cubic spline interpolation was implemented in Geant [98]. In this procedure all the data points are reproduced. Interpolation between them is done with a set of third order polynomials. Near the edge of the data set statistical fluctuations in the data propagate into the splines and lead to instable behavior. Hence splines cannot be used to extrapolate beyond the range of angles and energies covered by the data. In addition this parametrization has discontinuous higher derivatives which become visible in detailed studies. These two drawbacks make the spline interpolation less suitable for our purpose.
A more robust phenomenological model was built. It aims to use smooth analytical functions to describe the dependence of the cross section and analyzing power on the momentum transfer and incoming deuteron energy. This approach guarantees that the data are well reproduced, that there are no discontinuous derivatives and that the cross section and analyzing power can be extrapolated further than in the spline-based model. The three dominant reactions were implemented

1. elastic scattering
2. inelastic scattering
3. proton production

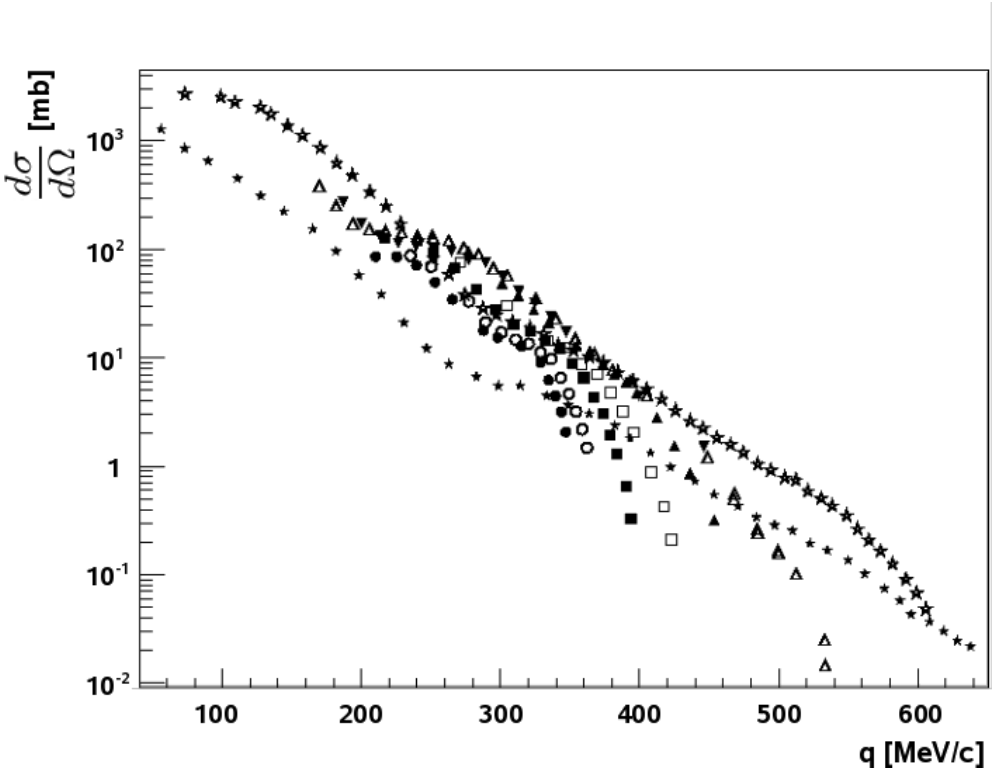

Figure 5.8: Differential cross sections for deuteron on carbon scattering for several energies plotted as a function of momentum transfer. The different symbols represent different deuteron incoming energy. Full circles: 270 MeV, empty circles: 133 MeV, full squares: 113 MeV, empty squares: 80 MeV, full up triangles: 76 MeV, empty triangles: 65 MeV, full down triangles: 56 MeV, full stars: 49 MeV and empty stars: 45 MeV.

5.6.1 Elastic Scattering

The analytical function describing the differential cross section is a function of the momentum transfer and deuteron incoming energy,

$$\frac{d\sigma}{d\Omega}(q, E). \tag{5.18}$$

The dependence on momentum transfer is implemented as a fifth order polynomial, of which the coefficients are second order polynomials as a function of $\ln E$.

$$\frac{d\sigma}{d\Omega}(q, E) = a_0 + a_1 q + a_2 q^2 + a_3 q^3 + a_4 q^4 + a_5 q^5 +$$

$$+ ln(E)\left[b_0 + b_1 q + b_2 q^2 + b_3 q^3 + b_4 q^4 + b_5 q^5\right] + \tag{5.19}$$

$$+ (ln(E))^2\left[c_0 + c_1 q + c_2 q^2 + c_3 q^3 + c_4 q^4 + c_5 q^5\right]. \tag{5.20}$$

Table 5.3: Values for the 18 free parameters of the phenomenological elastic scattering model for the differential cross section of deuteron on carbon scattering obtained by minimizing the least squared difference.

Parameter	Value	Unit
a_0	5.14×10^{1}	Constant
a_1	-2.42×10^{-2}	MeV^{-1}
a_2	-5.93×10^{-4}	MeV^{-2}
a_3	-1.40×10^{-6}	MeV^{-3}
a_4	2.04×10^{-9}	MeV^{-4}
a_5	3.41×10^{-15}	MeV^{-5}
b_0	-4.26×10^{-1}	Constant
b_1	-1.09×10^{1}	MeV^{-1}
b_2	5.45	MeV^{-2}
b_3	-1.34×10^{1}	MeV^{-3}
b_4	-2.11×10^{1}	MeV^{-4}
b_5	1.04×10^{4}	MeV^{-5}
c_0	4.97×10^{-2}	Constant
c_1	1.97	MeV^{-1}
c_2	-1.05	MeV^{-2}
c_3	2.51	MeV^{-3}
c_4	4.01	MeV^{-4}
c_5	-2.02×10^{3}	MeV^{-5}

Optimal values for the parameters are shown in table 5.3 and were found by through least squared difference minimization. Figure 5.9 shows the predictions together with the data available for some of the energies.

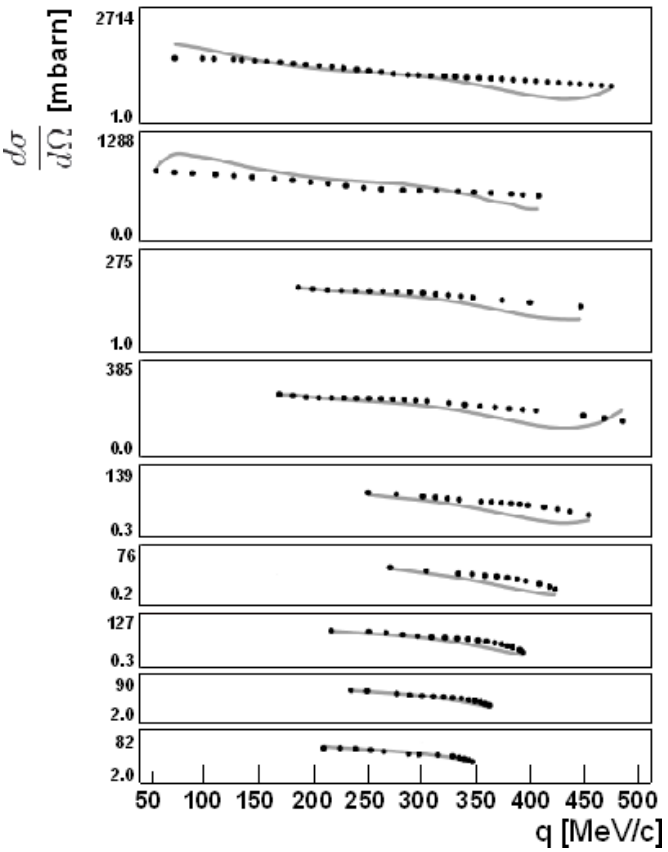

Figure 5.9: Comparison of the phenomenological model of the elastic differential cross section for deuteron on carbon scattering and the experimental data for different energies. The model results are represented by the solid lines and the data by the dots. The data is plotted without error bars. For each consecutive energy, the plots were reduced vertically by multiples of the energy . The energies plotted are 45, 49, 56, 65, 76, 113, 133, 200 and 270 MeV from the bottom to the top of the picture.

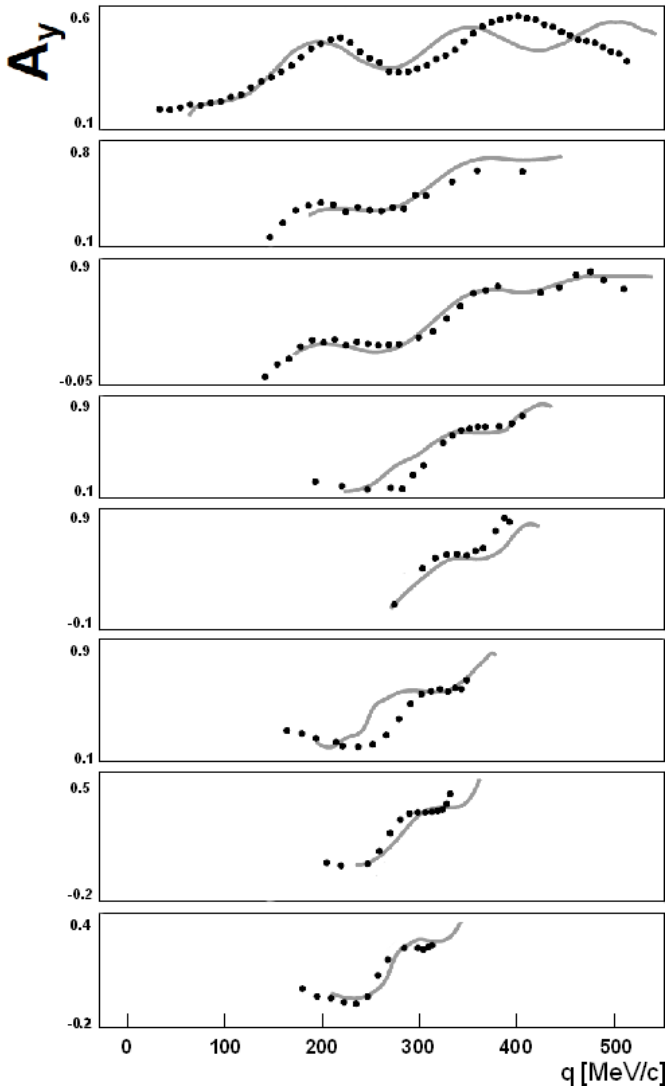

Figure 5.10: Comparison of the phenomenological model of the analyzing power for deuteron on carbon elastic scattering and the experimental data for different energies. The model results are represented by the solid lines and the data by the dots. For each consecutive energy, the plots were raised by multiples of the incoming energy. The energies plotted are 45, 49, 56, 65, 76, 113, 133, and 270 MeV from the bottom to the top of the picture.

Table 5.4: Values for the d coefficients used to parameterize the deuteron on carbon elastic scattering analyzing power in the phenomenological model (see equation 5.22).

d coefficient	Parameter	Value	Unit
d_1	k_0	1.16	Constant
d_1	k_1	7.12 $\times 10^{-3}$	MeV^{-1}
d_1	k_2	1.35×10^{-4}	MeV^{-2}
d_1	k_3	-5.54×10^{-7}	MeV^{-3}
d_2	k_0	16.1	Constant
d_2	k_1	-2.51×10^{-1}	MeV^{-1}
d_2	k_2	8.70×10^{-4}	MeV^{-2}
d_3	k_0	6.83	Constant
d_3	k_1	5.12×10^{-1}	MeV^{-1}
d_3	k_2	6.49×10^{-4}	MeV^{-2}
d_3	k_3	-4.76×10^{-6}	MeV^{-3}
d_4	k_0	9.45×10^{-1}	Constant
d_4	k_1	8.29×10^{-4}	MeV^{-1}
d_4	k_2	-5.40×10^{-6}	MeV^{-2}
d_5	k_0	2.21×10^{-1}	Constant
d_5	k_1	1.39×10^{-4}	MeV^{-1}
d_6	k_0	42.5	Constant
d_6	k_1	-2.55×10^{-1}	MeV^{-1}
d_6	k_2	3.41×10^{-3}	MeV^{-2}
d_7	k_0	58.6	Constant
d_7	k_1	-4.18×10^{-1}	MeV^{-1}
d_8	k_0	25.7	Constant
d_8	k_1	9.12×10^{-2}	MeV^{-1}
d_8	k_2	-1.86×10^{-4}	MeV^{-2}

The analyzing power is a function of the deuteron incoming energy and the scattering angle. It is parametrized as [99]

$$A_y^{pred}(E,\theta) = \frac{1}{1+\frac{900}{\theta^4}}\left[d_4\frac{d_1}{1+e^{\frac{\theta-d_2}{d_3}}} + d_5\left(1-\frac{\theta}{b_6}\right)\sin\left(d_7+d_8\theta\right)\right]. \qquad (5.21)$$

Each of the d coefficients is a polynomial function of energy difference ($\Delta E = E - 150\,MeV$). [99].

$$d_i = k_0 + k_1\Delta E + k_2(\Delta E)^2 + k_3(\Delta E)^3 \qquad (5.22)$$

The values of the k_i parameters are listed in table 5.4. In figure 5.10 this parametrization is compared to the data. Both the cross section and analyzing power parametrizations reproduce the order of magnitude of the data for each of the energies.

5.6.2 Inelastic Scattering

Inelastic cross section and analyzing powers for deuteron on carbon scattering are available from measurements performed at KVI for 76 and 113 MeV. This data shows little structure except for peaks at low excitation energy arising from the first excited states of carbon. The cross section is now parametrized as a function of the momentum transfer q in GeV/c and the excitation energy E_x in MeV.

$$\sigma(q,E_x) = 10^f. \qquad (5.23)$$

The polynomial function f that introduces the dependence on momentum transfer difference $\Delta q = q - 0.25$ MeV and excitation energy is

$$\begin{aligned} f(q,E_x) &= f_0 + f_1E_x + \left[f_2 + f_3E_x + f_4E_x^2\right]\Delta q & (5.24)\\ &+ \left[f_5 + f_6E_x\right](\Delta q)^2. & (5.25)\end{aligned}$$

The parameters f_i are listed in table 5.5. The comparison between the phenomenological model and the data collected at KVI at 113 MeV is displayed in figure 5.11.

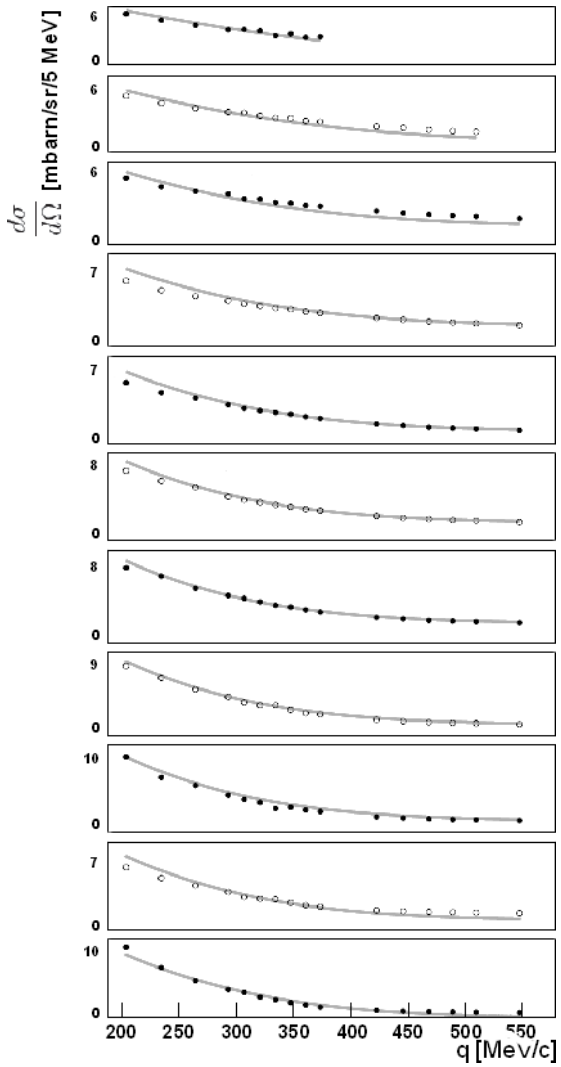

Figure 5.11: Cross section comparison between deuteron on carbon inelastic scattering data (bullets) and the model predictions (lines) for a beam energy of 113 MeV.The different curves are for different excitation energies. From bottom to top : 10, 15, 20, 25, 30, 35, 40, 45, 50, 55 and 60 MeV. The representation for excitation energy of 10 MeV is plotted with its real values. Data for all the other energies have been moved vertically for simultaneous display.

Table 5.5: Values for f_i used to characterize the deuteron on carbon inelastic scattering cross section in the phenomenological model.

f coefficient	Value	Unit
f_0	8.11×10^{-1}	Constant
f_1	-9.21×10^{-4}	MeV^{-1}
f_2	-3.12	GeV/c^{-1}
f_3	6.84×10^{-2}	$\mathrm{GeV}/c^{-1}\mathrm{MeV}^{-1}$
f_4	1.41×10^{-2}	$\mathrm{GeV}/c^{-1}\mathrm{MeV}^{-2}$
f_5	-4.89	GeV/c^{-2}
f_6	2.87×10^{-2}	$\mathrm{GeV}/c^{-2}\mathrm{MeV}^{-1}$

The analyzing power is parametrized as

$$A_y(q, E_x) = a_1 \left[1 - \frac{1}{1 + e^{\left(\frac{q-a_2}{a_3}\right)^{\frac{1}{10}}}} \right], \tag{5.26}$$

where the a_i represent functions of the excitation energy given by

$$a_i = h_0 - h_1 E_x + h_2 E_x^2. \tag{5.27}$$

The parameters h_i are listed in table 5.6. The comparison between the model

Table 5.6: Values for a_i used to characterize the deuteron on carbon inelastic analyzing power in the phenomenological model.

a coefficient	Parameter	Value	Unit
a_1	h_0	8.26×10^{-1}	Constant
a_1	h_1	-1.22×10^{-2}	MeV^{-1}
a_1	h_2	1.23×10^{-4}	MeV^{-2}
a_2	h_0	1.03×10^{-1}	Constant
a_2	h_1	-4.21×10^{-3}	MeV^{-1}
a_3	h_0	1.69×10^{-3}	Constant
a_3	h_1	2.34×10^{-4}	MeV^{-1}

predictions for the inelastic analyzing power and the KVI 113 MeV data is shown

in figure 5.12. In this case the cross sections are generally reproduced within 2%. Analyzing powers are typically reproduced within 3%. Both the cross section and analyzing power parametrizations for deuteron on carbon inelastic scattering reproduce the order of magnitude of the data for each of the excitation energies.

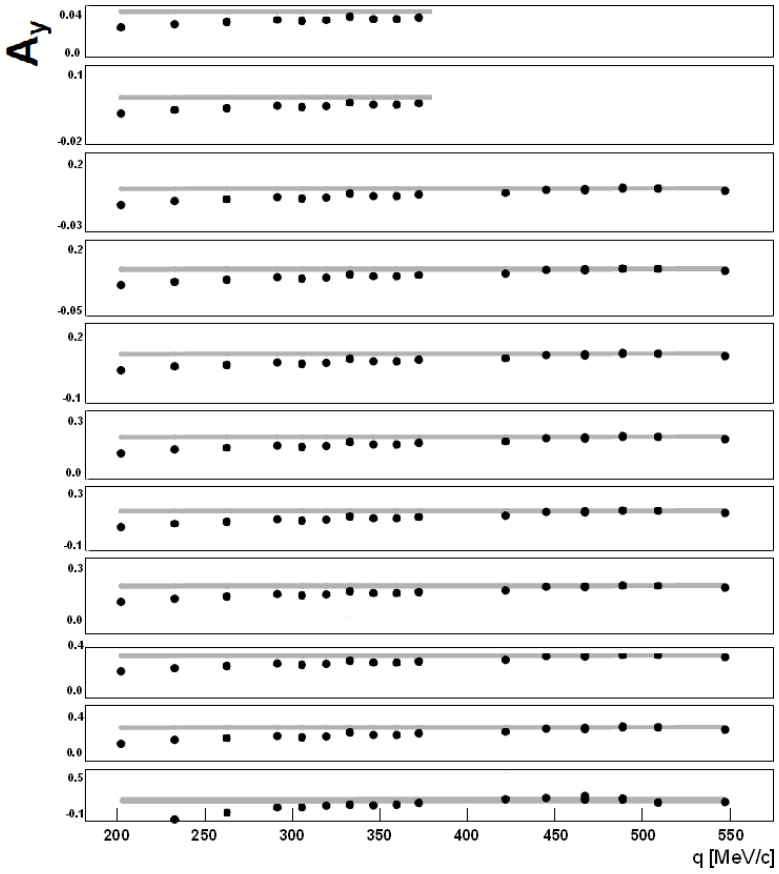

Figure 5.12: Analyzing power comparison between deuteron on carbon inelastic scattering data (bullets) and the model predictions (lines). The data were collected at KVI. The different curves represent different excitation energies. From bottom to top : 10, 15, 20, 25, 30, 35, 40, 45, 50, 55 and 60 MeV. The representation for excitation energy of 10 MeV is plotted with its real values. Data for all the other energies have been moved vertically for simultaneous display.

5.6.3 Deuteron Breakup

Together with the deuterons the other most important particles detected are protons. Deuteron breakup constitutes the most frequent deuteron induced reaction. Data was gathered at KVI for incoming deuteron energies of 76 and 113 MeV. The cross section is parametrized as a function of the momentum transfer q in GeV/c and the excitation energy E_x in MeV.

$$\sigma(q, E_x) = p_0(E_x) + p_1(E_x)q + p_2(E_x)q^2. \tag{5.28}$$

The polynomial functions p_i that introduce the dependence on excitation energy are

$$p_i(E_x) = s_0 + s_1 E_x + s_2 E_x^2 + s_3 E_x^3. \tag{5.29}$$

The parameters s_i are listed in table 5.7 The analyzing power is described as

Table 5.7: Values for p_i used to characterize the deuteron breakup cross section for deuteron on carbon scattering in the phenomenological model.

p coefficient	Parameter	Value	Unit
p_1	s_0	-6.11 $\times 10^{-1}$	Constant
p_1	s_1	1.61 $\times 10^{-1}$	MeV^{-1}
p_1	s_2	1.38$\times 10^{-3}$	MeV^{-2}
p_1	s_3	-3.89$\times 10^{-5}$	MeV^{-3}
p_2	s_0	-6.68$\times 10^{-3}$	Constant
p_2	s_1	-8.79$\times 10^{-4}$	MeV^{-1}
p_2	s_2	6.30$\times 10^{-6}$	MeV^{-2}
p_2	s_3	6.63$\times 10^{-8}$	MeV^{-3}
p_3	s_0	2.67$\times 10^{-5}$	Constant
p_3	s_1	1.39$\times 10^{-6}$	MeV^{-1}
p_3	s_2	1.50$\times 10^{-8}$	MeV^{-2}
p_3	s_3	2.71$\times 10^{-11}$	MeV^{-3}

a function of incoming energy E in MeV, momentum transfer q in GeV/c and excitation energy E_x in MeV.

$$A_y(E, q, E_x) = t_0 + t_1 \left(E_x - \frac{E}{2} \right). \tag{5.30}$$

The polynomial functions t_i introduce the dependence on momentum transfer. They are given by

$$t_i = \frac{u_0}{E^{k_1}} + \frac{1}{E^{k_1}}\left[u_1 + u_2 q + u_3 q^2\right] + u_4 + u_5 q + u_6 q^2 + u_7 q^3. \tag{5.31}$$

The parameters s_i are listed in table 5.8

Table 5.8: Values for t_i used to characterize the deuteron breakup analyzing power for deuteron on carbon scattering in the phenomenological model.

t function	Parameter	Value	Unit
t_1	k_1	2.12	Constant
t_1	k_2	1.04	Constant
t_1	u_0	-1280	$\mathrm{MeV}^{-2.12}$
t_1	u_1	-42.2	Constant
t_1	u_2	4.01×10^{-2}	GeV/c^{-1}
t_1	u_3	3.39×10^{-5}	GeV/c^{-2}
t_2	k_1	1.52	Constant
t_2	k_2	3.01	Constant
t_2	u_0	-7.35	$\mathrm{MeV}^{1.52}$
t_2	u_1	7.48×10^{4}	Constant
t_2	u_2	-1.36×10^{2}	GeV/c^{-1}
t_2	u_3	-2.01×10^{-2}	GeV/c^{-2}
t_2	u_4	-1.71×10^{-1}	Constant
t_2	u_5	1.44×10^{-4}	GeV/c^{-1}
t_2	u_6	-2.47×10^{-7}	GeV/c^{-2}
t_2	u_7	3.78×10^{-9}	GeV/c^{-3}

Both the cross section and analyzing power parametrizations for breakup protons from carbon inelastic scattering reproduce the order of magnitude of the data for each of the excitation energies.

5.7 Optimization of the Polarimeter Operating Point

The phenomenological model presented above can be used to find the optimal polarimeter configuration. Here we consider three parameters: (I) the target thickness; (II) the scattering angle acceptance; and (III) the energy acceptance. The efficiency, the figure-of-merit and the analyzing power are studied as a function of these parameters.
For thin targets the number of detected particles is proportional to the thickness of the target. Hence the figure-of-merit is also proportional to the target thickness. For thicker target the energy loss of the deuteron in the target must be taken into account since both the cross section and analyzing power are energy dependent. Rather than integrating over penetration depth in the target, integration is done over beam energy using the approximation

$$E(x) \simeq E_0 \sqrt{1 - \frac{x}{d(E_0)}}. \tag{5.32}$$

For a situation of a θ segmented detector, as intended for the dEDM experiment, the elastic scattering model was evaluated for different scattering angles and integrated over various target thicknesses. Figures 5.13, 5.14 and 5.15 represent, respectively, the cross section, analyzing power and figure-of-merit for such a case for a deuteron incoming energy of 250 MeV.

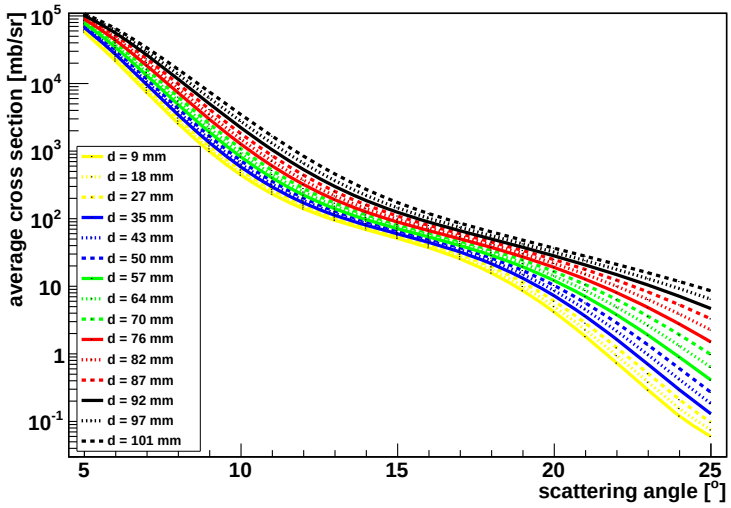

Figure 5.13: Model prediction for the cross section of deuteron on carbon elastic scattering as a function of scattering angle. The integration has been performed over different target thicknesses (represented by the different colors) as introduced in equation 5.15.

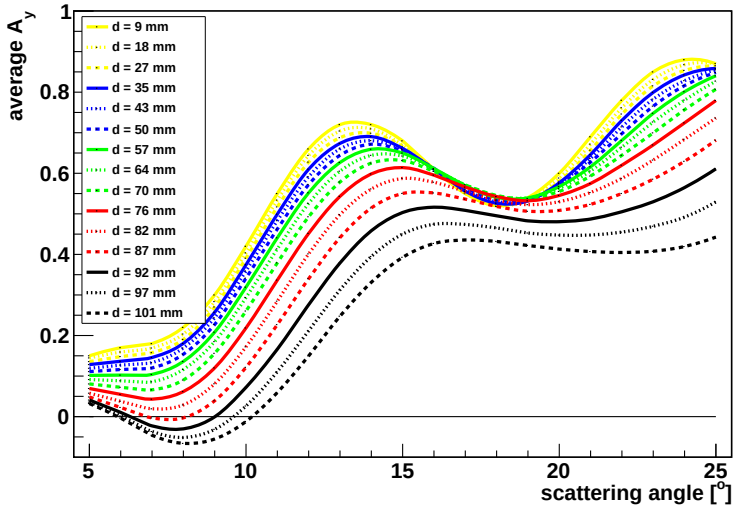

Figure 5.14: Model prediction for the analyzing power of deuteron on carbon elastic scattering as a function of scattering angle. The integration has been performed over different target thicknesses (represented by the different colors) as introduced in equation 5.15.

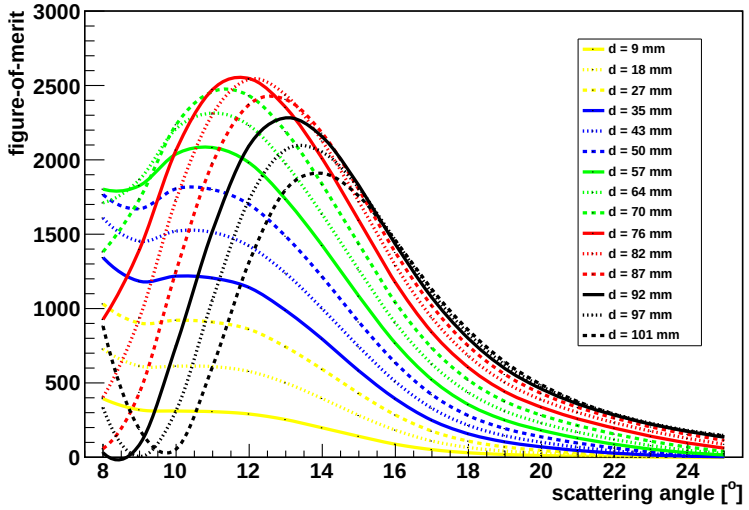

Figure 5.15: Model prediction for the figure-of-merit of deuteron on carbon elastic scattering as a function of scattering angle. The integration has been performed over different target thicknesses (represented by the different colors) as introduced in equation 5.15.

The maximum for the figure-of-merit for any of the target thickness integration domains falls within 5° and 10° in scattering angle. Defining the optimal operation point involves maximizing the figure-of-merit at the same time as choosing a region where the analyzing power is large. For this situation the analyzing power is large between 15° and 10°. This results in an optimal scattering angle range between 5° and 20°. The largest values for the figure-of-merit occur for a thickness between 6 and 8 cm.
Monte Carlo simulations of deuteron on carbon elastic scattering were performed yielding an optimal target thickness of 5 cm [98].
For a non segmented detector, such as the EDDA detector used for the studies at COSY (next section), the integration of the cross section and analyzing powers must be performed both over target thickness and scattering angle. Figures 5.16, 5.17 and 5.18 represent, respectively, the cross section, analyzing power and figure-of-merit for such a case for different outgoing energies.

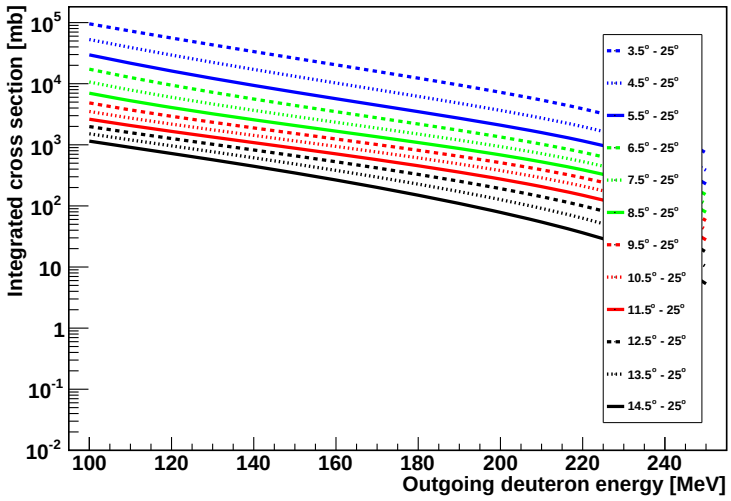

Figure 5.16: Model prediction for the cross section of deuteron on carbon elastic scattering as a function of deuteron outgoing energy. The integration has been performed over different target thicknesses and scattering angles (represented by the different colors) as introduced in 5.15.

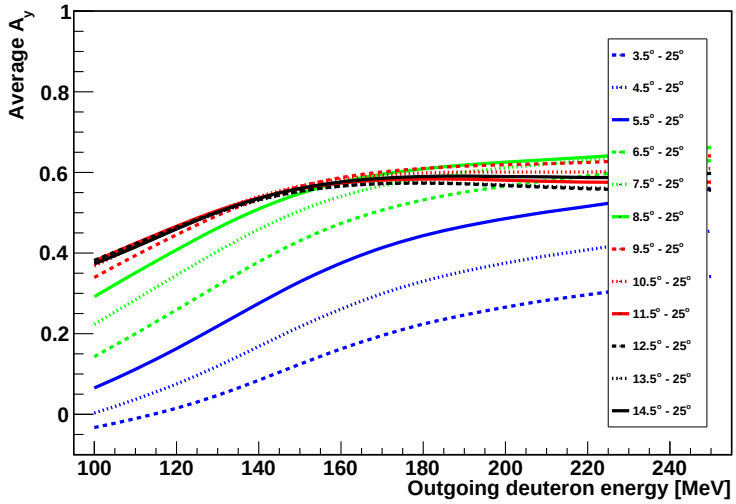

Figure 5.17: Model prediction for the analyzing power of deuteron on carbon elastic scattering as a function of deuteron outgoing energy. The integration has been performed over different target thicknesses and scattering angles (represented by the different colors) as introduced in 5.15.

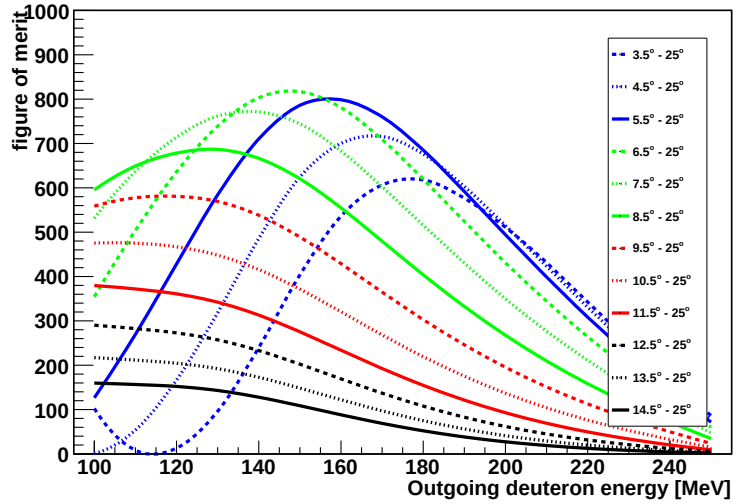

Figure 5.18: Model prediction for the figure-of-merit of deuteron on carbon elastic scattering as a function of deuteron outgoing energy. The integration has been performed over different target thicknesses and scattering angles (represented by the different colors) as introduced in 5.15.

In this case the figure-of-merit has a maximum at an outgoing deuteron energy of 145 MeV for scattering angles between 6.5° and 25°. This outgoing energy corresponds to an optimal target thickness of 6 cm.

5.8 Experimental studies

The feasibility of the polarimeter concept and the predictions of the model were tested experimentally. For this the EDDA detector at COSY-Jülich was used (see Chapter 2). The EDDA detector and COSY storage ring come as closely as possible to the configuration foreseen for the dEDM experiment. Three performance indicators were studied:

- the efficiency
- the analyzing power
- the figure-of-merit

Two different experiments were conducted, one at low energy threshold (Experiment 1) and another at high energy threshold (Experiment 2). In the following sections the general experimental setup used for both experiments is discussed. Details on each of the experiments follow specifying the specific changes made for each experiment regarding the use of the detectors, the electronics used and the experimental methods.

5.8.0.1 Experimental Setup

EDDA is a shared multi-purpose instrument of which the hardware could not be altered. The existing EDDA setup did not meet the experimental needs in two respects. First the target used for polarization measurements is a thin fiber. Secondly the data acquisition electronics and readout do not offer sufficient room for modification. In particular the lack of time resolution and significant dead time at the rates expected in our studies are incompatible with our goals.
Three new targets were constructed at COSY. One in the form of a tube and two in the form of a bar that approaches the beam from either the side or the

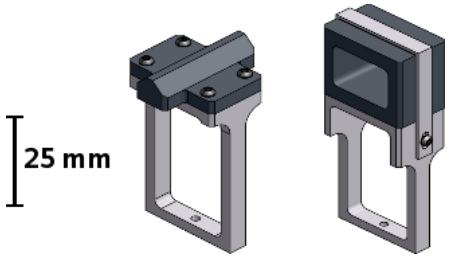

Figure 5.19: Targets used at COSY for polarimeter development measurements. The target on the left is the bottom target. The one on the right is the tube target, used for most measurements.

bottom (see figure 5.19). These targets were placed in the target carousel from where they were inserted into the storage ring vacuum. Because of the size of the feed-through from the carousel to the main COSY vacuum the length of these new targets was limited to 1.5 cm. Reactor grade graphite with a density of $2.22\,\mathrm{g/cm^3}$ was used as scattering material. This material was extensively tested for vacuum compatibility and approved for use in COSY.
A new data acquisition system was setup. To connect the EDDA system to this data acquisition only eight flat cables, containing all the analog signals from the bar and ring detectors, had to be reconnected (see figure 5.20).

Beam and detector

The part of the EDDA detector that was used contains 32 bars that form an azimuthally segmented barrel and 29 C-shaped half rings that form a barrel segmented along the beam direction [100]. Each of the bars is read out by a photomultiplier tube (PMT) on the upstream and downstream end. This yields a total of 64 analog signals. Each of the half-rings is read by a single PMT yielding a further 29 analog signals. The resulting fine segmentation is not needed for the performed studies and unnecessarily increases the number of readout channels.

Functional signal arrangement

To reduce the number of readout channels analog signals were added. In the two experiments that were performed different combinations were used as described below. Addition was done with linear fan-in/fan-out modules (LeCroy 428). The resulting grouped signals were sent to a Programmable Discriminator/Trigger/Amplifier Module (PDTAM) [101]. The sixteen analog input chan-

Figure 5.20: New KVI electronics (on the right) installed in parallel with the original EDDA system (on the left).

nels each have a remote-controlled offset and discriminator level. Trigger formation is done with a CPLD (Complex Programmable Logic Device). Up to eight trigger signals can be defined based on the 16 discriminator signals together with an additional eight logic control signals. Programming was done off-line.

Data taking modes

Control signals included a veto to prohibit output and a signal to switch between *measuring* and *calibration* mode. In calibration mode the OR of any of the 16 discriminator signals was used to generate the gate for a charge-sensitive analog-to-digital converter module (QDC) (Caen V792). This module was fed with the 16 analog outputs of the PDTAM to enable PMT calibration and determinations of offsets and thresholds.

In measuring mode the eight logic output signals were programmed to represent the counting rate in the up, down, left and right sector of EDDA (first experiment). In the second experiment a further selection of upstream and downstream was made. These eight logic signals together with the 16 discriminator signals were counted in a dead-time-free scaler module (Struck 7200-L or SIS3820). For time resolution studies the discriminator signals were also fed to a multi-hit time-to-digital converter module (Caen V1190).
Several additional logic signals were provided by the COSY control system. The most important one identifies that the beam in the storage ring is at flat-top (for data taking) or at injection or dump (no data taking). The spin state was identified by a four bit pattern. Each bit was derived from the state of one of the transition units of the source. A fast counting clock (5.7 MHz) signal was AND-ed with each of these bits and counted in the scaler module to identify the spin state. Finally, a calibrated beam-current transformer (BCT) signal was provided. This signal was fed into a voltage to frequency converter and into the scaler module. In appendix 1 a scheme of the electronics can be found.
The readout electronics was VME based. Besides the scaler, QDC and MTDC, an interrupt generating module (CES RCB 8047 (Corbo)) and a PCI-VME interface (SBS 620 and 810) were used. The setup was configured and read using the Caddie data acquisition program [102]. Three different interrupts and readout configurations were used: (1) Scaler readout at 10 Hz; (2) QDC readout triggered by the QDC module; (3) MTDC readout at 1 kHz. A Root[103] based program was used to collect, analyze and write to disk the data read by Caddie. The original EDDA data acquisition system TDAS was used to set the detector high voltages.
COSY was operated in 12 to 60 s cycles. During this cycle the beam is injected into COSY with an energy of 76 MeV. Then it is accelerated to the requested energy. Further beam manipulation can be made once the beam has reached the required energy, so-called "flat-top". This includes (de)bunching, beam re-centering or switching the noise source. Complicated sequences can be programmed to be executed automatically. This includes cycling through the polarization states, which is done automatically prior to each injection. Measurements were started after completion, typically 5 s after injection. Once most of the beam is extracted,

the remainder of the circulating beam is dumped, in our case 10 to 60 seconds after injection. Data collection is halted several milliseconds before the beam dump.

5.8.0.2 Experiment 1: Low Energy Threshold

Beam and detector

The deuteron beam momentum was chosen to be 1.2 GeV/c. This value was selected to make possible the testing of Multi-Resistive-Plate Chambers[89].
Only the signals from the EDDA bar detectors were used since they constitute the minimum requirement to determine asymmetries. The bars cover scattering angles between 11 and 72°. In this configuration, the detector has a large energy acceptance with a low energy threshold which is determined by the amount of material between the scattering vertex and the detection element.

Functional signal arrangement

The PMT signals from either the upstream or downstream end of the bars were added in groups of four each as represented in figure 5.21. Each group covers a 45° sector in azimuth. This yielded a total of 16 analog signals to the PDTAM. In the *measuring* mode of the PDTAM eight coincidences were defined between the upstream and corresponding downstream signals. These were combined in pairs with a logic OR to yield four output signals corresponding to the up, right, down and left segments of the detector, covering 90° in azimuth each.

Data taking modes

The calibration of the detectors was performed with the PDTAM in *calibration* mode. The high voltage and offset for each bar were calibrated individually based on the recorded QDC spectrum by switching on a single PMT at a time. The typical pulse area spectra did not show any pronounced features. The average pulse area was therefore used as a criterion to set the high voltages.
The spectral shape was a consequence of the choice of beam energy. The beam momentum was too high to stop elastically and nearly elastically scattered deuterons. As a consequence elastically scattered deuterons, which contain the highest analyzing power, produced a relatively low light output.

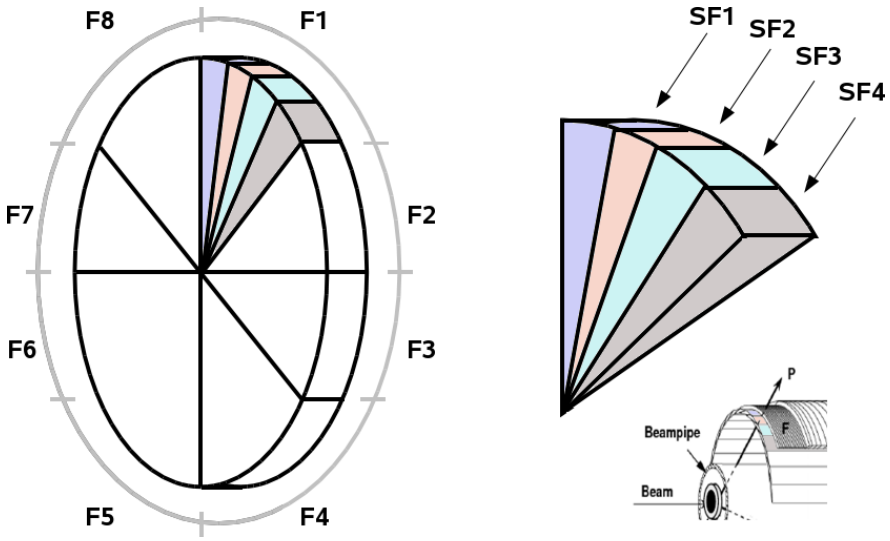

Figure 5.21: Functional arrangements of the EDDA bar detector signals to be fed into the data acquisition system. On the right side a zoomed view of the colored section is shown. The scheme represents the front detectors. Each group F_i is composed of four detectors SF_i with $i = (1, 2, ..., 32.)$ The back detectors are arranged in the exact same way. For these, each group B_i is composed of four detectors SB_i with $i = (1, 2, ..., 32.)$

The thresholds were scanned in the presence of a horizontal beam bump and set by optimizing the efficiency.
The efficiency is defined as the ratio of events over threshold used for a polarization measurement to the number of events lost from the circulating beam. The latter was calculated from the beam current transformer (BCT) signal. The stored beam intensity is defined as

$$N_{stored} = 6.24 \times 10^6 \frac{V_{BCT}[\mathrm{mV}]}{f_C[\mathrm{kHz}]} \tag{5.33}$$

At a momentum of $1.2\,\mathrm{GeV}/c$ the revolution frequency of COSY is $f_C = 881\,\mathrm{kHz}$. The particle loss rate is obtained from the time derivative of the number of stored particles.
In the last 487 COSY fills of the experiment with well defined spin state a total of 8.5×10^{11} particles were lost from the storage ring. Of these 1.3×10^{10} were recorded in EDDA. Poisson statistics determine the uncertainty on the number of

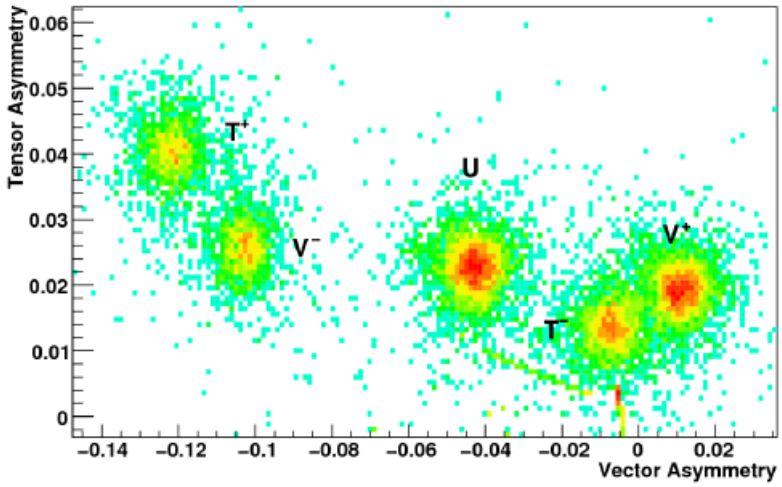

Figure 5.22: Distribution of measured vector and tensor asymmetries for 1 second long measurements. The five spin states used in the experiments are visible as colored blobs. Each blob corresponds to one spin state (p_z, p_{zz}). From left to right: Tensor plus (1,-1), Vector minus (-2/3,0), Unpolarized (0,0), Tensor minus (1/2,-1/2) and Vector plus (2/3,0).

detected particles. The uncertainty on the number of lost particles is determined by the noise on the BCT signal. This uncertainty is estimated from the minimum variance in the difference between the measured number of lost particles per measurement and the number of lost particle predicted from the number of detected particles and the unknown efficiency. From the minimum variance an uncertainty of 1.7×10^9 particles is assigned. This yields on average efficiency of $(1.534 \pm 0.003)\%$.
During these experiments the beam position was varied for systematics studies and the beam polarization was varied over five different states (see figure 5.22). The dependence of the efficiency on these variations was also studied.
The mean efficiency derived from the distribution of the efficiencies calculated per experiment and spin state is $(1.53 \pm 0.02)\%$. The error is calculated from the distribution of efficiencies rather than from the uncertainty in the individual measurements. It thus includes both statistical uncertainty and unaccounted for systematic variations. The reconstructed efficiency depends weakly on the spin

Table 5.9: Average efficiencies per spin state.

nominal spin state (P_V, P_T)	efficiency [%]
$(-2/3, 0)$	1.55 ± 0.02
$(2/3, 0)$	1.60 ± 0.03
$(-1, 1)$	1.46 ± 0.05
$(1/2, 1/2)$	1.50 ± 0.04
$(0, 0)$	1.47 ± 0.02

state (see table 5.9). The χ^2 for a test of a constant efficiency independent of the spin state is 17.3 with four degrees of freedom. A lower efficiency is found when the beam has a tensor polarization. This could point towards an average negative T_{20} analyzing power of approximately 0.09, which is unrealistically large. A second possibility is a rate dependence. The source intensity of the tensor states is approximately 80% of that for the other states. The efficiency is found to be independent of the number of particles lost per fill. This is confirmed with a probability of 39.5% ($\chi^2 = 20.00$ for 19 degrees of freedom) by fitting a constant to the data.

The linear relation between the number of detected and lost particles expected in the absence of rate effects has also been tested for the rate variations during a fill (see figure 5.23). Measurements were made in 1 s intervals. For instantaneous counting rates varying from zero to 300 kHz no statistically significant nonlinearity was observed. Also the center position of the beam has no statistically significant effect on the efficiency. The beam position was varied over a range of 1 cm (see next chapter) while feeding the kicker system with horizontal white noise. The efficiency could be fitted with a constant with a χ^2 of 4 for 6 degrees of freedom.

An efficiency of 1.5% for a target thickness of 1.5 cm corresponds to an integrated average scattering cross section of 90 mb. At 350 MeV the model predicts an elastic scattering cross section from 88 mb/sr for $\theta = 11°$ to 7.15 mb/sr for $\theta = 16°$. The maximum energy loss in the target is 24 MeV. For the corresponding deuteron energy of 326 MeV the cross sections at 11 and 16 degrees are 105 mb/sr and

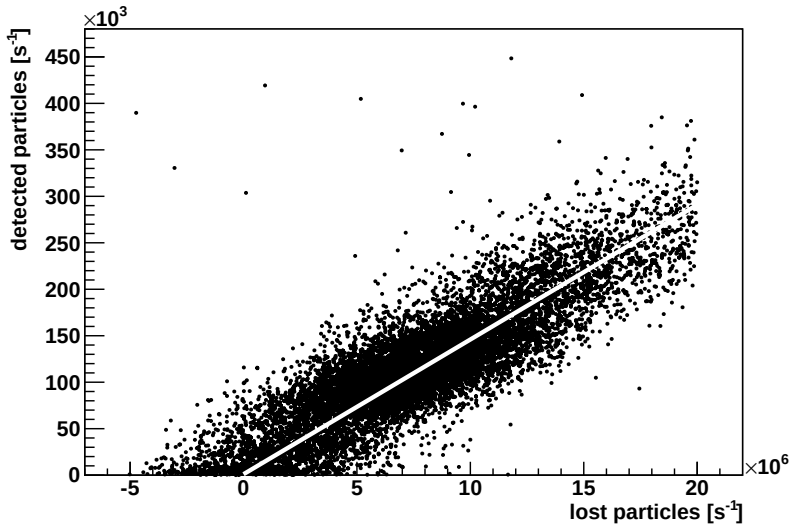

Figure 5.23: Relation between the number of detected and lost particles during a fill. The number of detected particles is, on average and within statistics, proportional to the number of lost particles. This indicated that at the level of sensitivity of this experiment pileup does not play a role. The white line has been added to the figure indicating the seen linear behavior.

11.64 mb/sr, respectively. Integrated over the EDDA acceptance a total average elastic scattering cross section of 5.3 mb is found.
Because of the beam energy of 350 MeV the model must extrapolate the inelastic scattering data. Furthermore the energy acceptance of the setup is not precisely known. Precise predictions are therefore not possible. The cross section of 85 mb is of the expected order of magnitude.
The left-right counting asymmetry is very sensitive to the beam and detector conditions (see next chapter). Therefore the analyzing powers were determined for a subset of the data for which the conditions were stable.five experiments from 6:41 till 10:57 on June 15 For the two purely vector polarized states and the unpolarized state the measured left-right asymmetries $\mathcal{A} = (R - L)/(R + L)$ are

$$\begin{array}{ll} \mathcal{A}_{V^+} & = (8.74 \pm 0.3) \times 10^{-2} \\ \mathcal{A}_0 & = (4.39 \pm 0.02) \times 10^{-2} \\ \mathcal{A}_{V^-} & = (-0.96 \pm 0.01) \times 10^{-2} \end{array} \tag{5.34}$$

The uncertainties are the effects on the mean of 4 or 5 independent measurements. Counting statistics contribute 0.01% to the error. Apparently there is an instrumental asymmetry which leads to a left-right counting asymmetry even for an unpolarized beam. This can be corrected by subtracting the result for the unpolarized beam,

$$\mathcal{A}_{V^+} - \mathcal{A}_0 = (4.4 \pm 0.3) \times 10^{-2} \tag{5.35}$$

$$\mathcal{A}_{V^-} - \mathcal{A}_0 = (-5.35 \pm 0.02) \times 10^{-2} \tag{5.36}$$

From these corrected asymmetries the analyzing powers can be calculated using

$$\mathcal{A}_{LR} = \frac{3}{2} \times 0.9 p \mathcal{A}. \tag{5.37}$$

The factor 0.9 accounts for the 90° azimuthal coverage of the left and right segments. The beam polarizations were measured independently at the beginning of the experiment with the low-energy polarimeter as $p^+ = 0.48 \pm 0.04$ for the V^+ state and $p^- = -0.63 \pm 0.04$ for the V^- state. This yields

$$\begin{array}{ll} A_y^+ & = \dfrac{1}{0.9}\dfrac{2}{3}\dfrac{\mathcal{A}_{V^+}}{p^+} = 0.15 \pm 0.02 \\ A_y^- & = \dfrac{1}{0.9}\dfrac{2}{3}\dfrac{\mathcal{A}_{V^-}}{p^-} = 0.142 \pm 0.009 \end{array} \tag{5.38}$$

for the V^+ state and for the V^- state respectively. These two results are compatible.
The observed asymmetries are of the expected magnitude. The model predicts an average analyzing power of approximately 0.9 for elastically scattered deuterons. The analyzing power of the remaining reactions, expected to be dominated by breakup, is assumed to be zero. From the measured efficiency and the predicted fraction of elastic scattering an average analyzing power of can be calculated,

$$\hat{A}_y = \frac{\sigma_{el}A_{el} + \sigma_{rest}A_{rest}}{\sigma_{total}} = (5 \times 0.9 + 85 \times 0)/90 = 0.05. \tag{5.39}$$

The total values for cross section and analyzing power are $\sigma_{total} = \sigma_{el}+\sigma_{rest}$, where σ_{el} represents the elastic contribution and σ_{rest} the non-elastic contributions. This is of similar size as the observed asymmetry.

5.8.0.3 Experiment 2: High Energy Threshold

After Experiment 1, Monte Carlo simulations of the target and detector were performed to investigate how the performance of EDDA could be improved [104]. Three improvements to the EDDA setup were implemented.

Beam and detector

First the beam momentum was lowered to 0.97 GeV/c corresponding to a kinetic energy of 250 MeV. Second the ring detectors were added so that the highest energy deuterons are stopped. Third the EDDA detector was moved 12.3 cm downstream to reduce the smallest accepted scattering angle to 10°.
At the lowered momentum elastically scattered deuterons are stopped in the second layer of EDDA, composed of ring detectors. The requirement of a hit in the second layer of detectors raises the physical energy threshold of the detector, simulating the effect of placing absorbers in the setup. This also makes possible to effectively use the electronic threshold to tune the performance.

Functional signal arrangement

Both the analog part of the electronics setup and the trigger program of the PDTAM were adapted. The simulations showed that the phenomenological combination of the energy deposit in the bars E_{bar} and the rings E_{ring},

$$E_{sum} = 1.8E_{bar} + E_{ring}, \tag{5.40}$$

could be used to reduce the scattering angle dependence of the energy acceptance. For this experiment only the downstream PMTs of the bars were used. The analog signals of eight bar PMTs were added using linear fan-in/fan-out forming four ϕ-sectors: up, right, down and left covering 90° in azimuth each. Similarly the six signals of the three most forward rings (left and right half) and those of the next four rings were added forming two θ-regions: covering forward (front) and backward (back) scattering angle between 11.19° and 13.66° and 13.66° and 20.15°, respectively. The used rings are represented in figure 5.24 From these six signals eight analog sums were formed by combining each of the ϕ signals with each of the θ signals (see Appendix 1).

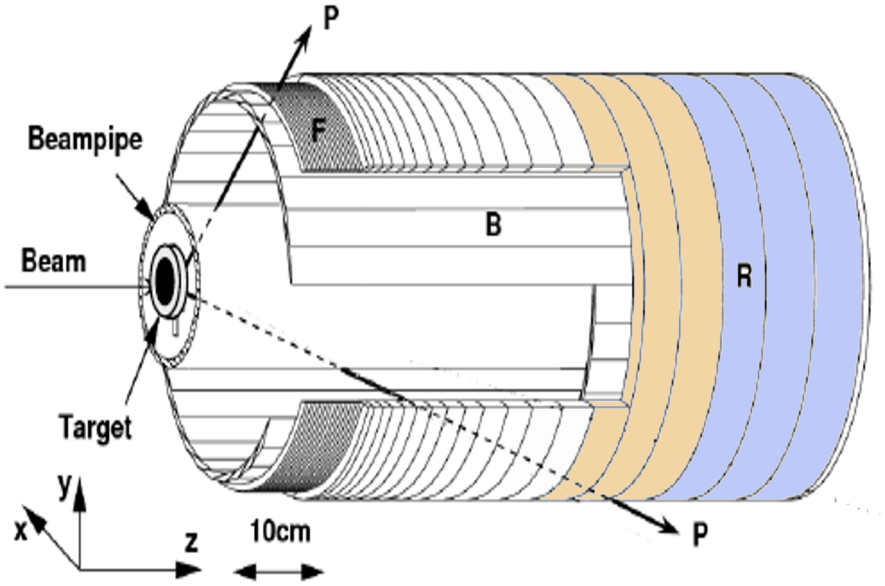

Figure 5.24: Functional arrangements of the EDDA ring detector signals to be fed into the data acquisition system. The rings are divided in front (blue) and (orange) back sections.

Data taking modes

The *calibration* mode of the PDTAM was left unchanged. For the *measurement* mode the PDTAM pattern recognition capability was used to define the outputs. A schematic view of the expected patterns is presented in figure A.1. Each box represents the discriminated signal of one of the eight inputs. When either of the two ring sections has a sufficiently large signal all four inputs containing that

section will generate a hit. Similarly a large signal in a bar section generates two hits. The combined pattern contains five logic 1's and three logic 0's. The outputs of the PDTAM contain the (exclusive) match between each of the eight possible patterns and the input pattern.

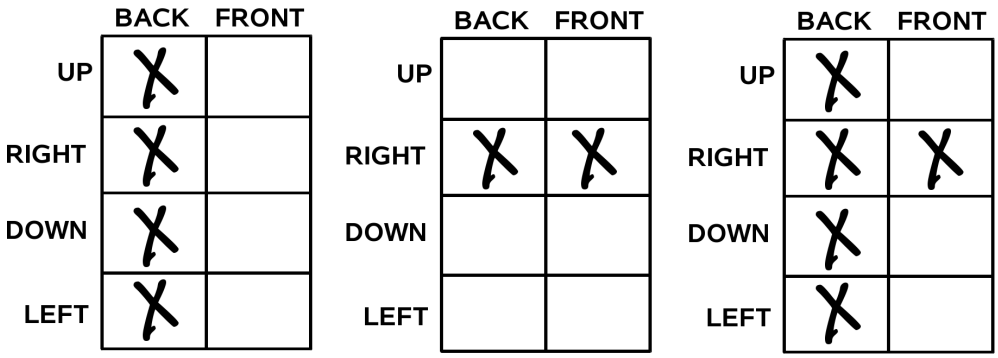

Figure 5.25: Example of one of the hit patterns recognized by the PDTAM. Up, right, down and left represent the functional groups of bar detectors. Front and back stand for the grouping of the ring detectors. A hit in a back ring generates the pattern represented on the left panel. A hit on the right section of the bars generates the pattern in the center panel. The PDTAM trigger is set to recognized a coincident hit in both a bar and a ring detector. Thus, an example of the pattern it recognizes is represented in the right panel.

Both the bar and ring detectors had to be calibrated. The first step was analogous to the calibration in the first experiment in which all the bars were calibrated individually. The second step involved the calibration of the ring detectors such that the factor 1.8 is recovered.
A common threshold on all PDTAM inputs was adjusted to yield an optimal figure-of-merit. The efficiency for the back and the front sections were determined as

$$\begin{aligned} \eta_{front} &= (1.769 \pm 0.015) \times 10^{-3} \\ \eta_{back} &= (0.718 \pm 0.006) \times 10^{-3} \end{aligned} \tag{5.41}$$

For this determination the experiments were used where the sensitivity for horizontal beam displacement with horizontal noise was tested. The efficiency does not depend on the horizontal beam position with a confidence level of 32% (front) or 11% (back).

Table 5.10: Experimental asymmetries, derivative of the asymmetries on the scattering angle, vector polarization and reconstructed vector analyzing power. Uncertainties are statistical only. The listed polarizations were determined at the beginning of the experiment.

state	$\mathcal{A}$	$\mathcal{A}'$	p_V	A_y
		front section		
Vplus	-0.253 ± 0.006	-0.235 ± 0.008	-0.682 ± 0.01	0.574 ± 0.02
Vminus	0.188 ± 0.006	0.206 ± 0.009	0.688 ± 0.01	0.499 ± 0.02
Tensor	-0.328 ± 0.005	-0.310 ± 0.008	-0.957 ± 0.01	0.540 ± 0.01
Unpolarized	-0.018 ± 0.006	0.000 ± 0.008	0.016 ± 0.008	0.000 ± 0.008
		back section		
Vplus	-0.309 ± 0.003	-0.252 ± 0.004	-0.682 ± 0.01	0.616 ± 0.01
Vminus	0.165 ± 0.003	0.222 ± 0.004	0.688 ± 0.01	0.538 ± 0.01
Tensor	-0.382 ± 0.002	-0.325 ± 0.004	-0.957 ± 0.01	0.566 ± 0.01
Unpolarized	-0.056 ± 0.003	0.000 ± 0.008	0.016 ± 0.008	0.000 ± 0.008

A small sensitivity to the vertical beam position was found,

$$\begin{aligned} \frac{d\eta_{front}}{dy} &= (-0.042 \pm 0.009) \times 10^{-3}\text{mm}^{-1} \\ \frac{d\eta_{back}}{dy} &= (0.014 \pm 0.004) \times 10^{-3}\text{mm}^{-1} \end{aligned} \tag{5.42}$$

These dependencies could be explained from small asymmetries in the detector acceptance. The efficiency does not depend on the polarization of the beam at a confidence level of 57% (front segment) or more.

The measured efficiencies correspond to integrated scattering cross sections of 10.6 mb and 4.31 mb for the front and back segment respectively. The model predicts integrated elastic scattering cross sections of 3.31 mb and 1.56 mb. The fraction of elastically scattered deuterons of 31% and 36% respectively is about 5 times higher than in the low energy threshold experiment.

The counting asymmetries and corresponding analyzing powers were determined for four polarization states. The results are listed in table 5.10.

Table 5.11: Model predictions for excitation energy, cross section and analyzing power for deuteron induced reactions for an incoming energy of 350 MeV and a target thickness of 1.5 cm for both the front and back sections of the EDDA detector.

E_x	σ[mb] Front	A_y Front	σ[mb] Back	A_y Back
		Elastic		
	10.6	0.54	4.31	0.573
		Inelastic		
4.44	0.64	0.5	1.05	0.5
< 10	1.29	0.5	2.09	0.5
< 15	1.96	0.5	3.10	0.5
< 20	2.63	0.5	4.10	0.5
		Protons		
8.5	0.06	-0.45	0.04	-0.18
< 12	0.13	-0.44	0.09	-0.18
< 16	0.24	-0.43	0.15	-0.17
< 20	0.38	-0.42	0.23	-0.17
		Total		
	10.6	0.54	4.31	0.57

During this experiment the polarization was more stable than in the first experiment. The (unknown) systematic uncertainty on the calculated analyzing powers is therefore expected to be much smaller. The model predicts average analyzing powers for elastic deuteron scattering of 0.64 and 0.62 for the front and back section respectively. The experimental values are on average 84% and 92% of these predicted values.

5.8.1 Performance Demonstration

5.8.1.1 Continuous Polarization Monitoring

Continuous polarization monitoring in a live environment is a necessity for the dEDM experiment. A demonstration of this capability was performed at COSY

(see figure 5.26)by monitoring a Froissart-Stora [105] sweep using an RF solenoid [106]. In such a sweep, the polarization of the beam is rotated by 180° by ramping the frequency of an RF magnet through an RF-induced spin resonance. The data

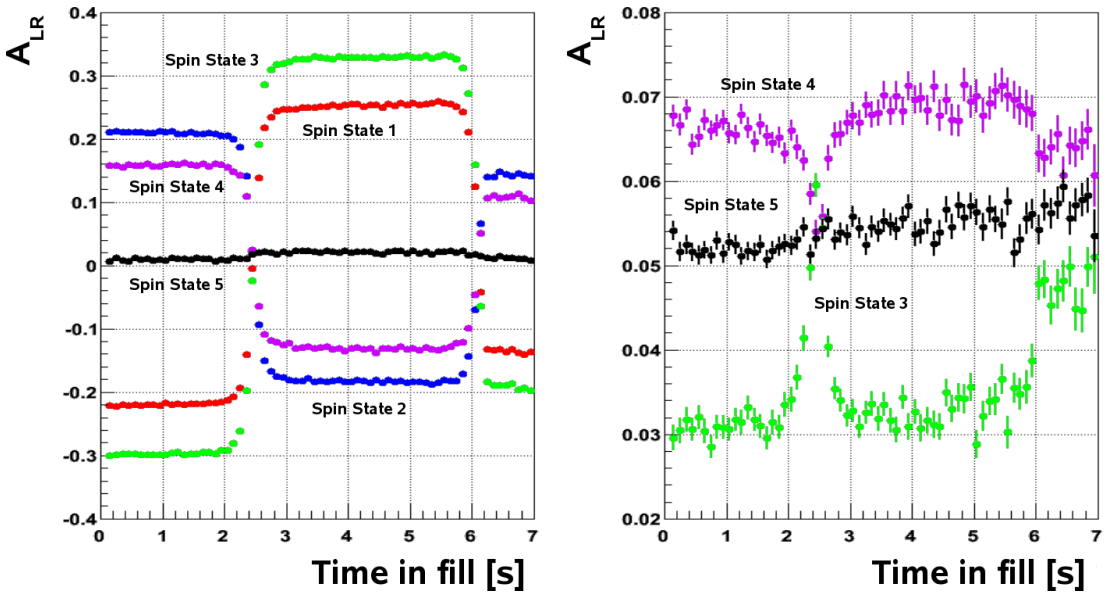

Figure 5.26: Tracking of beam polarization during crossing of depolarizing resonances. The left-right asymmetry $\mathcal{A}_{LR}$ was monitored during a fill of the storage ring for its vector (left panel) and tensor (right panel) components. Spin state 1 represents state (2/3,0). Spin state 2 represents state (-2/3,0). Spin state 3 represents state (1,-1). Spin state 4 represents state (1/2,-1/2). Spin state 5 represents state (0,0). The first transition at around 2.5 s corresponds to the spin resonance. The second (partial) transition at around 6 s is a spin synchrotron resonance.

shown is figure 5.26 was accumulated for 90 minutes. A full spin flip is visible for the vector component of the asymmetry. For the tensor component the *blip* in the asymmetry is caused by the $\cos 2\beta$ term (see figure 3.1). Already for a single ring fill the effect on the vector component of the asymmetry was visible.

5.8.1.2 Beam Bunch Monitoring

Identification of consecutive beam bunches will be needed to correct for systematic effects in the dEDM experiment. The beam bunching pattern, with beam

bunched on the first harmonic (h=1) of the cyclotron frequency, was monitored with the MTDC module. Figure 5.27 shows the pattern for the maximum bunching voltage available at COSY. The MTDC readout must be synchronized to

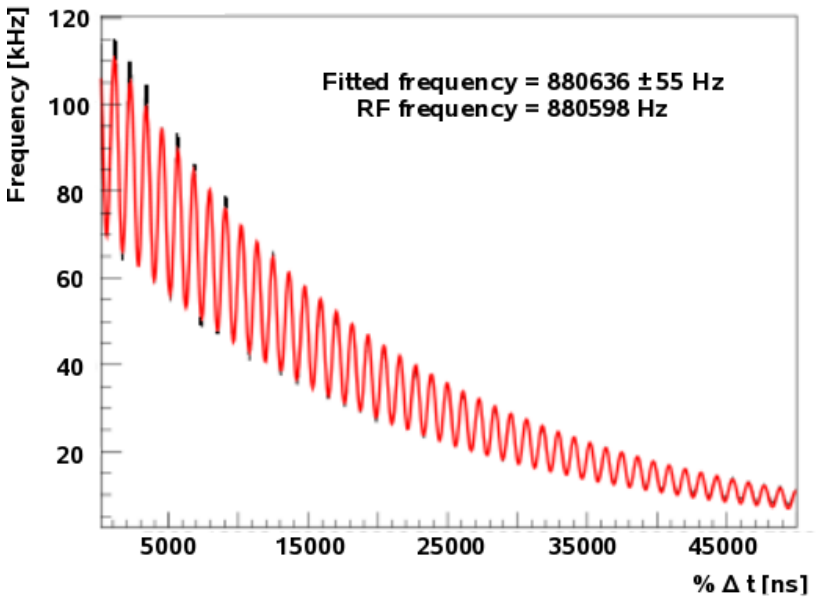

Figure 5.27: Distribution of the differences between consecutive events with beam bunched on the first harmonic. The overall exponential decline represents the distribution of time differences in a random distribution. The red curve is a fit to the original data which is plotted in black.

the bunching RF signal. Without this explicit synchronization no signal can be observed.
This measurements shows the capability of time resolution of the new DAQ necessary for future studies in which individual bunches must be identified.
The fitted pattern takes into considerations the Γ-distribution of the difference between successive hits. From the exponential behavior it can be concluded that no long term artifacts or beam structure are present. A fit to the modulation of the pattern yielded an RF frequency of 880636 ± 55 Hz consistent with the RF frequency which is set to 880598 Hz.

Table 5.12: Experimental results for the efficiency, analyzing power and figure of merit for the three conditions studied at COSY.

condition	η [%]	A_y	$FOM = \eta A_y^2$ [%]
350 MeV, low E-threshold	1.53 ± 0.02	0.14 ± 0.01	$3.00 \times 10^{-2} \pm 0.02$
250 MeV, high E-threshold, front	0.177 ± 0.002	0.58 ± 0.04	$5.10 \times 10^{-2} \pm 0.01$
250 MeV, high E-threshold, back	0.0718 ± 0.0006	0.57 ± 0.04	$2.36 \times 10^{-2} \pm 0.01$

5.9 Conclusion

The deuteron EDM polarimeter development tests performed at COSY have provided confirmation of the model predictions for the optimal polarimeter operating point. The tests have been performed with a 1.5 cm thick tube carbon target for different detector configurations. In table 5.12 the experimental results for the efficiency and the analyzing power are summarized.
These made possible the comparison between different deuteron energies and between setups with and without an absorber. In the first measurement high efficiencies and low analyzing powers were found, indicating a strong presence of breakup protons. At the same time, deuteron breakup suppresses spin dependence leading to the low value for the analyzing power. In the second experiment the incoming deuteron energy was lowered and the outer detector layer of EDDA was included. This resulted in lower efficiencies but higher analyzing power, indicating spin-dependent scattering and thus the presence of mainly deuterons. The figure-of-merit for both measurements is similar: 4.6×10^{-6} for low threshold and 4.8×10^{-6} for high threshold. Measurements made with higher analyzing powers are less sensitive to systematic effects. Hence the high threshold configuration is preferred.

Chapter 6

Polarimeter Selectivity

The EDM signal is a gradual change of the polarization component along the magnetic field. In the previous chapter an efficient method to measure the polarization was presented. This method is based on the azimuthal dependence of the scattering cross section on the polarization and the resulting distribution of the counting rate over the detector. Phenomena that affect the counting rate might thus lead to a signal which is mistaken for an EDM signal.
In this chapter the *selectivity* of the polarimeter concept is discussed. Selectivity is defined as the ability to distinguish the true signal from other signals, in other words the ability to suppress systematic effects.
Two analysis strategies are evaluated. First the linear left-right asymmetry is pointed out. This asymmetry is commonly used to measure the counting rate asymmetry caused by a polarized beam. Afterwards the more robust method based on non-linear cross ratios is introduced and discussed. Two parameters are defined: the first is mostly sensitive to the polarization of the beam whereas the second is mostly sensitive to beam displacements and rotations. The resulting systematic effects of several imperfections are shown.
Beam displacements and rotations are an important source for systematic effects. Their impact is discussed in detail. Next the results of numerical simulations and the results obtained by a dedicated experimental study performed at KVI are presented and the results obtained in studies at COSY are discussed.

6.1 Signal Definition

6.1.1 Linear Combination

Ideally the counting rate in a detector is given by the scattering formula 5.2. A straightforward polarization measurement can be performed through the left-right asymmetry introduced in the previous chapter defined as

$$\mathcal{A}_{LR} = \frac{L - R}{L + R}. \tag{6.1}$$

Here L and R represent the detected rates in the left and right detectors. Both rates depend on the polarization,

$$\begin{aligned} L &= N\left(1 + P_y A\right), \\ R &= N\left(1 - P_y A\right), \end{aligned} \tag{6.2}$$

where P_y stands for the vertical component of the vector polarization, N for the counting rate for an unpolarized beam and A for the analyzing power. The left-right asymmetry becomes

$$\mathcal{A}_{LR} = P_y A \tag{6.3}$$

A change in P_y with time reflects into a time dependence on $\mathcal{A}_{LR}$. Measuring the latter and knowing the analyzing power A is sufficient to determine P_y.
If the left and right count rates and analyzing powers are not the same this simple relation does not hold. Rate modification can be generically parametrized as

$$\begin{aligned} L' &= L + \epsilon_L \\ R' &= R + \epsilon_R. \end{aligned} \tag{6.4}$$

Depending on which mechanism is responsible for the change in count rates ϵ_L and ϵ_R may be related. Introducing these rate modifications into equation 6.1 the left-right asymmetry becomes

$$\mathcal{A'}_{LR} = \frac{L' - R'}{L' + R'} = \frac{L - R + \epsilon_L - \epsilon_R}{L + R + \epsilon_L + \epsilon_R} \tag{6.5}$$

Assuming that ϵ_L and ϵ_R are small compared to $L + R$, the first-order Taylor expansion becomes

$$\mathcal{A'}_{LR} \simeq \mathcal{A}_{LR}\left[1 - \frac{\epsilon_L + \epsilon_R}{L + R}\right] + \frac{\epsilon_L - \epsilon_R}{L + R} + \mathcal{O}(higher). \tag{6.6}$$

The left-right asymmetry thus has a first order dependence on both $(\epsilon_L + \epsilon_R)/N$ and $(\epsilon_L - \epsilon_R)/N$ with $N = \frac{L+R}{2}$.
For the EDM experiment, the interest lies in changes in $\delta\mathcal{A}_{LR}$ at the level of 10^{-7}. This implies that *symmetric* rate changes should be constrained to

$$\mathcal{A}_{LR}\frac{\epsilon_L + \epsilon_R}{2N} < \delta\mathcal{A}_{LR} = 10^{-7} \tag{6.7}$$

Assuming that the injected beam has a non-zero vertical polarization no larger than several %, $\mathcal{A}_{LR}$ might be as large as 10^{-3}. This leads to the constraint that

$$\frac{\epsilon_L + \epsilon_R}{2N} < 10^{-4} \tag{6.8}$$

whereas *asymmetric* rate changes should be constrained to

$$\frac{\epsilon_L - \epsilon_R}{2N} < \delta\mathcal{A}_{LR} = 10^{-7} \tag{6.9}$$

The requirement on asymmetric rate changes is considerably more demanding. The first order dependence on relative rate changes leads to very stringent requirements on experimental parameters. For a precise measurement of the polarization a large sensitivity to systematic effects is undesirable. A more suitable measure of the polarization than the left-right counting rate ratio should be used.

6.1.2 Non-Linear Combinations

6.1.2.1 Cross Ratio

A more robust asymmetry can be calculated from a non-linear combination, referred to as cross ratio. In an analogous way to the linear asymmetry, the counting rates in the left and right detectors for beams with opposite polarization are combined. The relevant rates are given by

$$\begin{aligned} L^+ &= f^+ L_0 \left(1 + A_L P_y^+\right), \\ L^- &= f^- L_0 \left(1 + A_L P_y^-\right), \\ R^+ &= f^+ R_0 \left(1 - A_R P_y^+\right), \\ R^- &= f^- R_0 \left(1 - A_R P_y^-\right), \end{aligned} \tag{6.10}$$

where f^+ and f^- represent the fraction of the integrated beam luminosity for either polarization state and L_0 and R_0 the counts for an unpolarized beam of

the left and right detector, respectively. Furthermore, the analyzing power of the left detector (A_L) and right detector (A_R) are introduced. From these rates, a squared ratio r^2 can be defined as

$$r^2 = \frac{L^- R^+}{L^+ R^-} = \frac{1 + A_L P_y^- - A_R P_y^+ - A_L A_R P_y^- P_y^+}{1 + A_L P_y^+ - A_R P_y^- - A_L A_R P_y^- P_y^+}. \tag{6.11}$$

In this approach, the integrated luminosities (f_+ and f_-), as well as the detector acceptances (L_0 and R_0) drop out identically. For this ratio the asymmetry can be calculated

$$\varepsilon_{LR} = \frac{1 - r}{1 + r}. \tag{6.12}$$

Assuming $P_y^+ = -P_y^- = P_y$ and $A_L = A_R = A$ it takes the form,

$$r^2 = \left[\frac{1 + AP_y}{1 - AP_y}\right]^2. \tag{6.13}$$

so that

$$\varepsilon_{LR} = \frac{(1 - AP_y) - (1 + AP_y)}{(1 - AP_y) + (1 + AP_y)} = AP_y. \tag{6.14}$$

This measure is independent of the detector acceptance (as far as it does not lead to $A_L \neq A_R$) and the integrated beam intensity and thus constitutes a superior method over the left-right asymmetry discussed before.
In the next section the sensitivity to several possible sources of systematic effects is studied in detail. The sensitivity to beam-detector displacement and rotation will be treated in detail. It will be shown that several sources of systematic effects only appear in second order.

6.1.2.2 ζ parameter

As previously mentioned, the development of the dEDM polarimeter focuses on identifying systematic effects and establishing a correction method to eliminate them or reduce them as much as possible. In order to do so, an independent measure of the strength of these systematic effects is crucial. The chosen approach is to define a zeta-parameter ζ in an analogous way to the cross-ratio asymmetry but independent from it,

$$\zeta = \frac{1 - s}{1 + s} \tag{6.15}$$

where s is defined as

$$s = \left[\frac{L^+L^-}{R^-R^+}\right]^{1/2}. \tag{6.16}$$

It will be shown later that ζ can be used effectively to expose beam position shifts and rotations.

6.2 Sensitivity to Detector Acceptance and Beam Polarization

6.2.1 Detector Acceptance

The detector acceptance affects both the average rate and the analyzing powers of a detector. Although the cross ratio asymmetry ε_{LR} is insensitive to the former, it remains sensitive to the latter. In the previous chapter the average analyzing powers was introduced (see page 105). The dependence on the acceptance in scattering angle $\Delta\theta = [\theta_{min}, \theta_{max}]$ and the azimuthal acceptance $\Delta\phi = [\phi_{min}, \phi_{max}]$ follows from

$$A_{ang} = \frac{1}{\Delta\phi}\frac{\int_{\Delta\phi}\sin\phi\, d\phi \int_{\Delta\theta}\frac{d\sigma}{d\Omega}(\theta)A(\theta)d\theta}{\int_{\Delta\theta}\frac{d\sigma}{d\Omega}(\theta)d\theta}, \tag{6.17}$$

where $\Delta\phi$ and $\Delta\theta$ are assumed to be independent.
Here the energy and particle acceptance are included in $d\sigma/d\Omega(\theta)$ and $A(\theta)$,

$$\frac{d\sigma}{d\Omega}(\theta) = \sum_{i\in species}\int_{\Delta E_i}\frac{d^2\sigma_i}{d\Omega dE}(\theta)dE \tag{6.18}$$

and

$$A(\theta) = \left(\frac{d\sigma}{d\Omega}(\theta)\right)^{-1}\sum_{i\in species}\int_{\Delta E_i}\frac{d^2\sigma_i}{d\Omega dE}(\theta)A_i(\theta, E)dE \tag{6.19}$$

Nominally the acceptance of the left and right detector are the same. For independent E, θ and ϕ acceptance the nominal analyzing power is given by

$$A_L^0 = A_R^0 = \frac{\sin\delta/2}{\delta/2}\frac{\int_{\Delta\theta}\frac{d\sigma}{d\Omega}(\theta)A(\theta)d\theta}{\int_{\Delta\theta}\frac{d\sigma}{d\Omega}(\theta)d\theta}. \tag{6.20}$$

A difference in either the energy, scattering angle or azimuthal angle will thus lead to a difference in A_L and A_R.

6.2.1.1 Changes of the Analyzing Power

Assuming that $P_y^+ = -P_y^- = P_y$, the following ratios can be defined,

$$\hat{A} = \frac{A_L + A_R}{2} \tag{6.21}$$

$$dA = \frac{A_L - A_R}{2}. \tag{6.22}$$

For the case of the left-right asymmetry this leads to a change given by

$$\mathcal{A}_{LR} = \mathcal{A}^0_{LR}\left[1 - dAP_y\right] \tag{6.23}$$

where $\mathcal{A}^0_{LR}$ is $\hat{A}P_y$. For the case of the cross ratio the change is given by

$$\varepsilon_{LR} = \varepsilon^0_{LR}\left[1 - (dAP_y)^2\right] \tag{6.24}$$

where ε^0_{LR} is $\hat{A}P_y$. A time dependence of dA or $\hat{A}$ in combination with a non-zero P_y mimics the EDM signal.

In a realistic experiment, the vertical polarization component P_y will be of the order of 10^{-2}. Therefore changes in dA and $\hat{A}$ must be tightly controlled to avoid fake EDM signals. The change in the polarization ΔP_y due to the EDM leads to a change in the left-right cross ratio asymmetry ε_{LR} of $\hat{A}\,\Delta P_y = \mathcal{O}(10^{-7})$. Therefore dA must be smaller than $10^{-3/2}$. If P_y varies sufficiently over the course of the experiment, ε_{LR} can be extrapolated to $P_y = 0$.

It is possible to generate a simultaneous and same-signed change in the analyzing powers of the left and right detectors from, for example, rate related effects or acceptance changes due to a drift in the power of the detector elements or the electronics readout system. Assuming that ε^0_{LR} varies and that $dA(t)$ is always the same, such an effect can be corrected.

6.2.1.2 Rotation of the Detector about the Beam

If the detector is rotated about the beam by an angle ψ the left-right asymmetry is no longer sensitive to P_y. Instead the asymmetry is sensitive to the polarization component

$$P'_y = P_y \cos\psi + P_x \sin\psi \simeq P_y + P_x\psi \tag{6.25}$$

In the frozen spin method the horizontal polarization component P_x is supposed to be constant. A slow drift in P_x can lead to a false EDM signal proportional to $dP_x/dt\psi$. For both $\mathcal{A}_{LR}$ and ε_{LR} the resulting changes are (to first order in ψ)

$$\mathcal{A}_{LR} = \mathcal{A}_{LR} + AP_x\psi \tag{6.26}$$

$$\varepsilon_{LR} = \varepsilon_{LR} + AP_x\psi. \tag{6.27}$$

The rotation of the detector can be established by allowing the spin to precess instead of freezing it. In this case,

$$P_x(t) = P_0 \cos \Omega \mathrm{t} \tag{6.28}$$

with P_0 the magnitude of the polarization. The left-right asymmetry and the cross ratio will then contain a term oscillating at a frequency of Ω. In a full precession cycle, the measured asymmetry reaches its maximum when the spin is oriented perpendicular to the beam axis. This asymmetry is six orders of magnitude larger than the EDM signal and can thus be determined with great precision in a short measurement. To eliminate the small effect due to the tilt of the precession axis caused by the EDM, the sign of Ω can be inverted. This also changes the sign of the oscillating term while leaving the EDM term unchanged. Another approach involves a measurement of the ϕ-distribution over the detector. This distribution reflects the orientation of the beam polarization and will also oscillate when the spin is not completely frozen and a few precession cycles are allowed during the store.
Both $\mathcal{A}_{LR}$ and ε_{LR} have a first order dependence in ψ. The resulting systematic effect can be determined with more than sufficient precision to eliminate it. This is done by letting P_x vary.

6.2.2 Beam Polarization

6.2.2.1 Sensitivity of $\varepsilon_{\mathbf{LR}}$ to a Change in $\mathbf{P_y}$

Not only the presence of an EDM causes P_y to change. If the initial P_y is non-zero, depolarizing effects can also lead to a time dependence of the vertical polarization. If $|P|$ slowly decreases over the course of the fill due to some (de-)polarizing effect, then $|P^+| = |P^-| = P_y^0 - dP$.

The change in the left-right asymmetry can be expressed as

$$\mathcal{A}_{LR}(dP) = A(P_y^0 - dP_y). \tag{6.29}$$

The change in the cross ratio is given by

$$\varepsilon_{LR}(dP) = A(P_y^0 - dP_y) = \varepsilon_{LR}(1 - \frac{dP_y}{P_y^0}), \tag{6.30}$$

where the last equality holds for an initially non-zero vertical polarization.
This means that the depolarization of the beam generates a false EDM signal. When the initial vertical polarization is zero, then also ε_{LR} is zero and equation 6.31 should be used. For a polarization $P_y \sim 10^{-2}$, depolarization of the *vertical* component must be limited to 1:1000.
One physical effect that may lead to a growth of P_y is the Sokolov-Ternov effect, which leads to polarization along the magnetic field in case of highly relativistic electrons. It is proportional to γ^5 [107]. This effect is too weak to produce any noticeable effect for deuterons at 1 GeV/c.
The EDM signal is an actual change in the vertical polarization component of the beam, just like the effect discussed here. They can therefore not be distinguished from each other by the polarimeter and will have to be controlled by the careful design of the storage ring. This is beyond the scope of this thesis.

6.2.2.2 Sensitivity of $\varepsilon_{\mathbf{LR}}$ to a Difference in $\mathbf{P^+}$ and $\mathbf{P^-}$

Whereas the left and right counting rate are simultaneously determined, measurements for P^+ and P^- are made separately using different beams. Even for the best ion sources, a difference between P^+ and P^- is unavoidable.
For a situation where there is a difference between $|P^+|$ and $|P^-|$, defined as $\hat{P} = \frac{|P^+|+|P^-|}{2}$ and $dP = \frac{|P^+|-|P^-|}{2}$, and assuming that $A_L = A_R = A_0$, the change in cross-ratio is given by

$$\varepsilon_{LR}(dP) = \varepsilon_{LR}(1 + A_0^2 dP^2). \tag{6.31}$$

The polarization difference only appears as a second order effect.
Because the effect of the EDM is opposite for opposite polarizations, the EDM signal is amplified just a little. If dP grows linearly in time, then the false EDM signal grows quadratically, which can be used to distinguish it from the true EDM signal which grows linearly in time.

6.2.2.3 Sensitivity to Tensor Polarization

For the development of polarimetry for the deuteron EDM it is necessary to take into account the fact that the deuteron is a spin-1 particle. Although the vector and tensor polarizations can be controlled independently, not all combinations are possible. The phase space defined by both the vector and tensor components can be depicted schematically as shown in figure 6.1.

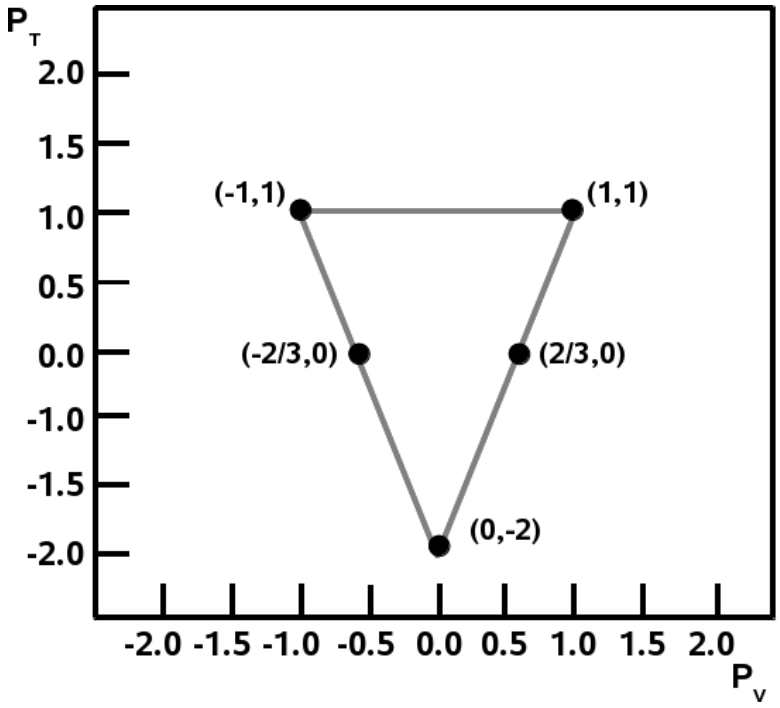

Figure 6.1: Space defined by the magnitude of the vector and tensor polarization components for a deuteron. Only combinations of P_V and P_T in the triangle are possible

For a beam with non-zero tensor polarization, the left and right count rates are given by 3.26

$$L = L_0 \left(1 + A_L P_V + B_L P_T\right) \tag{6.32}$$

$$R = R_0 \left(1 - A_R P_V + B_L P_T\right), \tag{6.33}$$

where $N_{L,R}$ stands for the number of counts in the left and right detector, $A_{L,R}$ for the associated vector analyzing powers, $B_{L,R}$ for the associated tensor analyzing

powers and P_V for the vector polarization and P_T for the tensor polarization. Following the formalism introduced in section 6.1.1, the change in the left-right asymmetry with a non-zero tensor contribution is

$$\mathcal{A}'_{LR} \simeq \mathcal{A}_{\mathcal{LR}} \left[1 - \frac{2B_L P_T}{2N(1 + 2B_L P_T)} \right] + \mathcal{O}(higher), \tag{6.34}$$

where $\mathcal{A}_{\mathcal{LR}}$ is the previously defined original left-right asymmetry for a vector-only polarized beam.

Also the cross ratio asymmetry can be evaluated for the case of the tensor contribution to the beam polarization. When flipping the vector polarization, the tensor polarization remains the same. Hence the count rates previously given in equation 6.10 are modified as

$$\begin{array}{rcl} L^+ & = & f^+ L_0 \left(1 + A_L P^+ + B_L P_T\right), \\ L^- & = & f^- L_0 \left(1 + A_L P^- + B_L P_T\right), \\ R^+ & = & f^+ R_0 \left(1 - A_R P^+ + B_R P_T\right), \\ R^- & = & f^- R_0 \left(1 - A_R P^- + B_R P_T\right). \end{array} \tag{6.35}$$

Assuming that $f^+ = f^- = f$, $L_0 = R_0 = L$, $A_L = A_R = A$ and $B_L = B_R = B$ and using the same approach as for equation 6.13, the cross ratio asymmetry in the presence of a tensor component changes to

$$\varepsilon'_{LR} = \varepsilon_{LR} \frac{1}{1 + BP_T}. \tag{6.36}$$

To mimic an EDM signal ε_{LR} must be non- zero and $B_L P_T$ must be time dependent. It is claimed that scattering spin-one deuterons from residual gas may introduce a t_{20} contribution[108, 109] and hence a time dependent P_T. In the absence of gas no such polarization effect exist. Using a noisy kicker rather than a gas jet might thus be necessary to extract the beam.

6.3 Sensitivity to Beam-Detector Displacement and Rotation

The position and orientation of the detector relative to the beam greatly affects the acceptance of the detector, independent of whether the beam or the detector

changed its position. In particular, the accepted range of scattering angles will be affected. The cross section and analyzing power both strongly depend on the scattering angle θ, as shown in the previous section. Any change in the θ-acceptance has a potentially large effect on the measured signal because the solid angle of a detector element, the observed cross section and the effective analyzing power change simultaneously. To study this dependence an analytical model was developed to describe the sensitivity of the left-right asymmetry, the cross-ratio asymmetry and a new cross-ratio zeta parameter.

6.3.1 Left-Right Asymmetry

To study the sensitivity to changes in the alignment of the detector with respect to the beam the expressions for the cross section and the vector and tensor analyzing powers, A and B respectively, are expanded as second order Taylor series,

$$\sigma(\theta) = \sigma(\theta_0 + d\theta) = \sigma(\theta_0) + \sigma' \cdot d\theta + \sigma'' \cdot (d\theta)^2 \tag{6.37}$$

$$A(\theta) = A(\theta_0 + d\theta) = A(\theta_0) + A' \cdot d\theta + A'' \cdot (d\theta)^2 \tag{6.38}$$

$$B(\theta) = B(\theta_0 + d\theta) = B(\theta_0) + B' \cdot d\theta + B'' \cdot (d\theta)^2. \tag{6.39}$$

with σ' and σ'' the first and second derivative of σ with respect to θ evaluated at $\theta = \theta_0$. A and B have been expanded in the same way.
Nominally the left and right detector probe the same angular range. When the polarimeter is rotated by an angle ψ about the y-axis the central angle of the left and right detector change by ψ and $-\psi$, respectively. Using equations. 6.37 – 6.39 the rates in the left and right detector are given by,

$$\begin{aligned} L(\psi) &= \sigma(\theta + \psi)\left[1 + p_V A(\theta + \psi) + p_T B(\theta + \psi)\right] \\ R(\psi) &= \sigma(\theta - \psi)\left[1 - p_V A(\theta - \psi) + p_T B(\theta - \psi)\right]. \end{aligned} \tag{6.40}$$

Replacing the expressions for $\sigma(\theta)$, $A(\theta)$ and $B(\theta)$, by 6.37, 6.38 and 6.39 the experimental left-right asymmetry can be calculated through

$$\mathcal{A}_{LR} = \frac{L - R}{L + R}. \tag{6.41}$$

Up to second order in ψ this becomes

$$\mathcal{A}_{LR} = \frac{\varepsilon_V}{1 + \varepsilon_T} + \left[\frac{\varepsilon_V^2}{(1 + \varepsilon_T)^2}\left(\frac{\sigma'}{\sigma} + \frac{A'}{A}\right) - \frac{\varepsilon_V}{1 + \varepsilon_T}\frac{B'}{B} - \frac{\sigma'}{\sigma}\right]\psi +$$

$$\frac{\varepsilon_V}{1+\varepsilon_T}\left[\frac{A''}{A}-(\sigma'\sigma)^2+\frac{\varepsilon_T}{1+\varepsilon_T}\left(\left(2\sigma'\sigma+\frac{A'}{A}\right)\frac{B'}{B}+\frac{B''}{B}\right)+\frac{\varepsilon_V^2}{(1+\varepsilon_T)^2}\left(\frac{\sigma'}{\sigma}+\frac{A'}{A}\right)^2\right]\psi^2, \tag{6.42}$$

where ε_V and ε_T represent, respectively, the real left-right asymmetry caused by the presence of the vector and tensor components of the beam. Beam misalign-

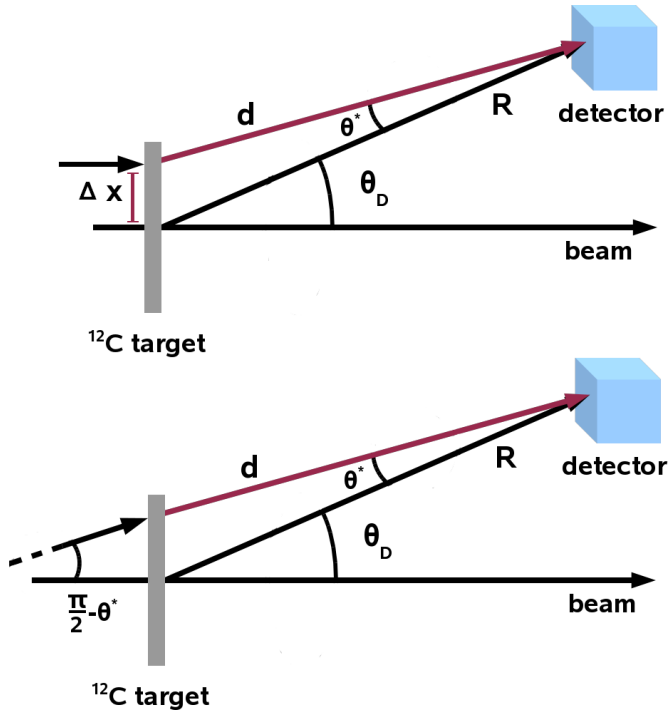

Figure 6.2: Schematic representation of beam misalignment effects. Both the position and angle shift can be parametrized through the same ψ parameter.The black horizontal arrow represents the incoming beam. The diagonal black arrow defines the scattering angle seen by the detector θ_{D} for an optimal configuration. The red arrow identifies the displaced beam. The θ^* angle is the effective angle difference that is introduced in the system. For this parameterization, both effects are treated in the same way.

ments and rotations can be parametrized in a similar way. As shown in figure 6.2 they both lead to a shift in θ .

Effect of beam shifts

Considering a beam shifted to the right as depicted in figure 6.2,

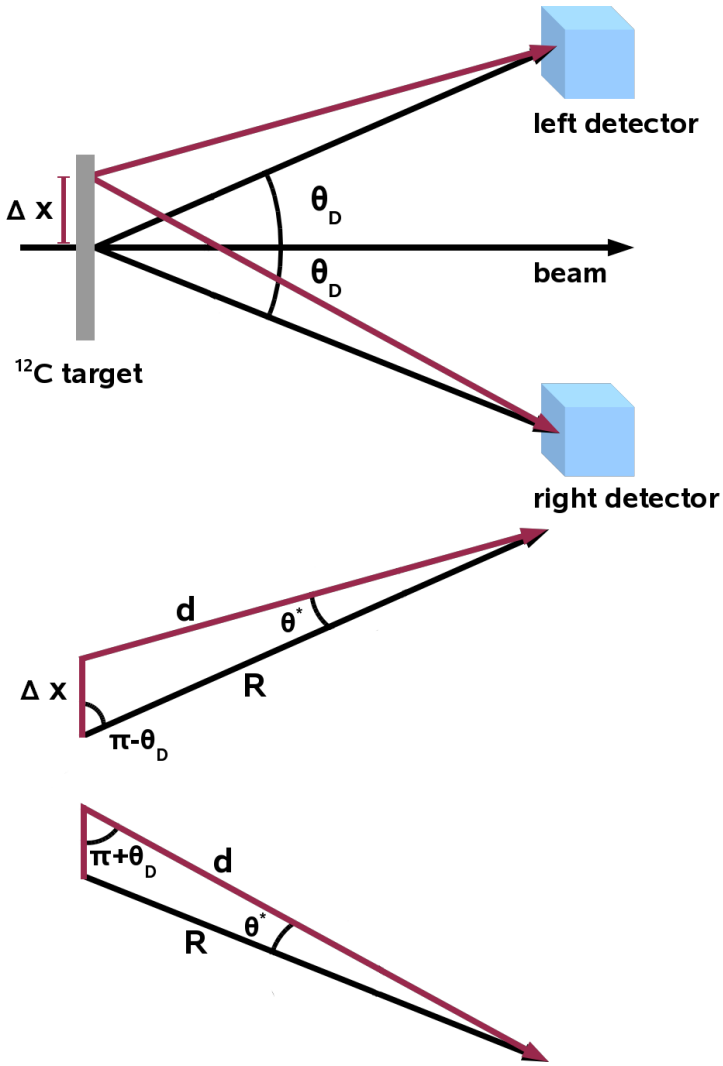

Figure 6.3: Effect introduced by changing the position of the scattering vertex for both the left and the right detectors. The black horizontal arrow represents the incoming beam. The diagonal black arrow defines the scattering angle θ_{D} seen by the detector for an optimal configuration. The red arrow identifies the displaced beam. The θ^* angle is the effective angle difference that is introduced in the system. A beam displaced to the left causes a decrease in the effective scattering angle in the left detector and an increase by the same amount in the right detector. The opposite happens for a beam displaced to the right.

the angle difference introduced in the system can be parametrized as

$$\psi = \frac{x}{R}\cos\theta_{\mathrm{D}}(1 + \frac{x}{R}\sin\theta_{\mathrm{D}}), \tag{6.43}$$

where $\frac{x}{R}$ stands for the ratio between the beam displacement and the distance between the scattering vertex and the detector. θ_D is the nominal angle of the detector. This amount is subtracted from the nominal angle for the left detector and added to that of the right one,

$$\theta_L = \theta_D - \psi \tag{6.44}$$

$$\theta_R = \theta_D + \psi \tag{6.45}$$

Change in solid angle for beam shifts

Using the quantities introduced in figure 6.3, the ratio between the solid angle for the optimal configuration Ω_0 and the beam shifted one Ω_x is given by

$$\frac{\Omega_x}{\Omega_0}\frac{\mathrm{R}^2}{\mathrm{d}^2} = 1 + 2\frac{x}{R}\sin\theta_{\mathrm{D}} - \frac{x}{R}^2(1-4)\sin^2\theta_{\mathrm{D}} \tag{6.46}$$

Calculating the left-asymmetry consists of evaluating the sequence laid out in 6.3.1 for the reaction scattering angles (or effective angles seen by the detector) corrected with ψ. The correction for the effect is done by multiplying the ratio defined in 6.46 by the cross section being evaluated.

The result for the left-right experimental asymmetry yields,

$$\begin{aligned}\mathcal{A}_{LR}\left(\frac{x}{R}\right) = \mathcal{A}^0_{LR} &+ \left\{2(1-\varepsilon^2)\sin\theta_{\mathrm{D}} + \left[\left(\frac{\sigma'}{\sigma} + \frac{A'}{A}\right)\varepsilon^2 - \frac{\sigma'}{\sigma}\right]\cos\theta_{\mathrm{D}}\right\}\frac{x}{R} \\ &+ \left\{-4\sin^2\theta_D + \left(4\frac{\sigma'}{\sigma} - \frac{A'}{A}\right)\sin\theta_D\cos\theta_{\mathrm{D}} + \left(\frac{A''}{A}\right) - \left(\frac{\sigma'}{\sigma}\right)^2\cos^2\theta_D\right\}\varepsilon\left(\frac{x}{R}\right)^2 \\ &+ \left\{4\sin^2\theta_D - 4\left(\frac{\sigma'}{\sigma} - \frac{A'}{A}\right)\sin\theta_D\cos\theta + \left(\frac{\sigma'}{\sigma} + \frac{A'}{A}\right)^2\cos^2\theta\right\}\varepsilon^3\left(\frac{x}{R}\right)^2. \end{aligned} \tag{6.47}$$

where $\mathcal{A}^0_{LR}$ represents the real asymmetry. A shift in the scattering vertex has already an effect at first order. In the dEDM experiment the injected beam will be longitudinally polarized so that $\varepsilon^0 \simeq 0$. The first order term in x/R then becomes

$$\mathcal{A}_{LR} = \mathcal{A}^0_{LR} + \left[2\sin\theta_D - \frac{\sigma'}{\sigma}\cos\theta_D\right]\frac{x}{R}. \tag{6.48}$$

The shift in $\mathcal{A}_{LR}$ thus depends on θ_D. This can be used in the analysis to distinguish the EDM signal from a shift in x. Having verified this linear dependence on the beam displacement it became clear that a more robust method was necessary.

6.3.2 Cross Ratio

The effect of a position shift on the cross ratio can be obtained in a similar fashion. An ideal detector setup is considered meaning $A_L = A_R$. In such a setup acceptance differences and intensity differences between opposite polarized beams do not contribute. Two small systematic effect driving terms are considered. ψ as the angle by which the beam is steered at the target and $u = p^+ + p^-$. With these two parameters the perturbation in the cross ratio becomes

$$\varepsilon_{LR} = \varepsilon^0_{LR} + \frac{1}{1-{\varepsilon^0_{LR}}^2}\left\{{\varepsilon^0_{LR}}^2\frac{A'}{A}\mathrm{u}\psi + \varepsilon^0_{LR}\left[\frac{A''}{A}(1-{\varepsilon^0_{LR}}^2) - \left(\frac{A'}{A}\right)^2{\varepsilon^0_{LR}}^2\right]\psi^2\right\}. \tag{6.49}$$

In this expression, ψ represents either the reaction angle change induced by a beam rotation as defined in equation 6.43 or the amount by which the scattering angle changes when the beam is displaced.
Here it should be noted that the effect is driven only by the analyzing power and its derivatives. For the dEDM experiment with $\varepsilon^0_{LR} \simeq 0$ it becomes

$$\varepsilon_{LR} = \varepsilon^0_{LR} + \varepsilon^0_{LR}\frac{A''}{A}\psi^2 \tag{6.50}$$

6.3.3 Error Parameter

For a beam steered at the target by θ, the measured asymmetry for the ζ parameter can be written as,

$$\zeta = \left[-\frac{\sigma'}{\sigma} + \frac{\varepsilon^2}{1-\varepsilon^2}\frac{A'}{A}\right]\theta. \tag{6.51}$$

Here θ represents either the reaction angle change induced by a beam shift of the amount by which the scattering angle changes when the beam is displaced. Once more the reaction angle change θ is parametrized as $\theta = \frac{\Delta x}{R}\cos\theta$ where $\frac{\Delta x}{R}$ represents the shift displacement.

6.3.4 Simulation Studies for $\mathcal{A}_{LR}$ and ε_{LR}

The sensitivity to beam shifts depends on the cross section and analyzing powers and their derivatives. Their contributions were introduced using the simplified expressions

$$\sigma = \sigma_0 \mathrm{e}^{-b\theta} \tag{6.52}$$

$$\mathrm{A} = A_0 + A_1 \mathrm{e}^{-\left(\frac{\theta-\theta_0}{u}\right)^2}. \tag{6.53}$$

These functions were fitted to the elastic scattering data obtained at 113 MeV at KVI yielding, $\sigma_0 = e^{8.35}$, $b = 0.2189 perdegree$, $\theta_0 = 22.14°$, $A_0 = 2/3$,$A_1 = -0.483$ and $u = 9.97$. From these the various coefficients in 6.47 and 6.49 both the cross section and analyzing power derivatives can be calculated using

$$\frac{\sigma'}{\sigma} = b \tag{6.54}$$

$$\frac{A'}{A}(\theta) = \frac{-2\theta + 2\theta_0}{\frac{A_0}{A_1 \mathrm{e}^{-\left(\frac{\theta-\theta_0}{u}\right)^2}} + 1} \tag{6.55}$$

$$\frac{A''}{A}(\theta) = \frac{-2\mathrm{e}^{-\left(\frac{\theta-\theta_0}{u}\right)^2} + (-2\theta + 2\theta_0)^2}{u^2 \left[\frac{A_0}{A_1} + \mathrm{e}^{-\left(\frac{\theta-\theta_0}{u}\right)^2}\right]}. \tag{6.56}$$

At various angles the resulting sensitivity to Δx was evaluated (see table 6.1) Figure 6.4 shows the predictions of the Monte-Carlo model for different beam-

Table 6.1: Sensitivity to Δx evaluated at different angles for a deuteron incoming energy of 113 MeV.

Angle[°]	σ[mb]	A	σ'/σ	A'/A	A"/A
18	82.253011	0.259885	-0.218900	-0.130383	0.020633
28	9.214700	0.324520	-0.218900	0.124311	0.006556
38	1.032311	0.628186	-0.218900	0.019548	-0.005005
48	0.115648	0.666088	-0.218900	0.000452	-0.000218

detector displacements and for different scattering angles. These predictions depict the left-right asymmetry to first order in misalignments and the cross-ratio asymmetry to second order.

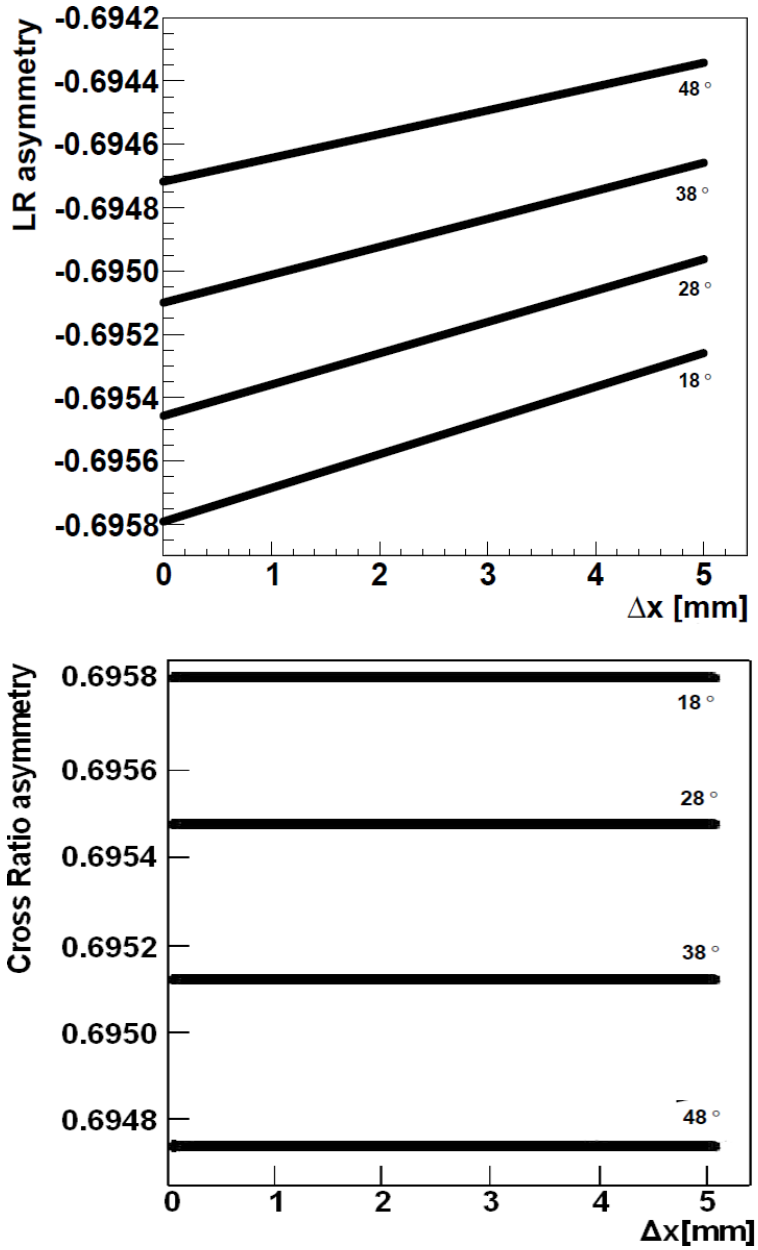

Figure 6.4: Monte-Carlo simulation of the behavior of the left right asymmetry (left panel) and cross ratio asymmetry (right panel) in the presence of beam-detector misalignments. Predictions are shown for 18, 28, 38 and 48 degrees in scattering angle.

6.4 Experimental Studies at KVI

6.4.1 Experimental Setup

Experimental studies to test the feasibility of correcting for beam-detector displacements systematic effects were performed at KVI. The measurements were carried out using the In-Beam Polarimeter [73] described in Chapter 2 of this dissertation.

The detectors at the IBP location were rearranged with 4 detectors in each horizontal and vertical arm at $\theta = 18°$, $28°$, $38°$ and $48°$ as shown in figure 6.4.1. The detectors at $28°$ and $38°$ are used to calibrate the beam polarization measurements through the elastic deuteron-proton reaction. The IBP targets are mounted on a wheel and eight different targets assemblies are possible. The target wheel can be rotated by a stepping motor with a step of 0.024 degrees. One step corresponds to about $30\mu m$ in target movement.

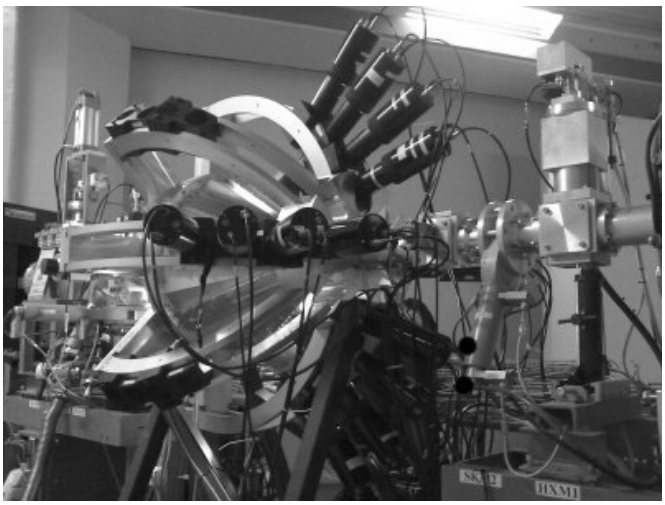

Photograph of the IBP detector at KVI at the time of the experiment. Both the horizontal and vertical arms support 8 PMTs.

Two targets were of interest for these studies. A 9.8 mg/cm^2 polyethylene (CH_2) target was used for the polarization calibration. Sensitivity studies were performed on a 1 mm wide carbon vertical ribbon of thickness 11 mg/cm^2. A narrow strip was used to have a well defined scattering vertex.
To optimize the efficiency of the polarimeter as many protons as possible must be removed. This was done by placing an aluminum absorber in front of the detectors. The thickness of such an absorber can be deduced through the following scaling relation, which relates the range of any nucleus to that of the proton,

$$R_d\left(E_d\right) = \frac{A}{Z} R_p\left(E_d/2\right) = 2R_p\left(E_d/2\right) \tag{6.57}$$

At the beam energy of 113 MeV, the energy of elastically scattered deuterons ranges from 113 MeV at 18° to 80 MeV at 48°. The energies of interest covered the range from 80 to 110 MeV in deuteron outgoing energy. Estimates were made for different absorber thicknesses. Table 6.2 lists these estimates together with the kinetic energies for which protons and deuterons are stopped for each thickness. Using expression 6.57 and the results from table 6.2 it was estimated that a 80 MeV deuteron would be stopped by 5.71 mm thick absorber. For this study 5 mm aluminum absorbers were used.

Table 6.2: Stopping power for protons (E_p) and deuterons (E_d) for various thicknesses of aluminum.

d	E_p	E_d
mm	MeV	MeV
0.10	3.61	5.22
0.23	5.58	7.66
0.51	8.87	11.93
1.14	14.12	18.98
2.56	22.35	30.19
5.77	35.28	47.78
12.97	55.62	75.38
29.19	87.84	118.85

6.4.1.1 Beam Setup

The experiment was conducted at a nominal beam energy of 110 MeV and a beam current of 1 nA. At this current the maximum rate per detector, per mbarn and per nA was about 8.7 Hz.
The measurements were performed with five polarization states, with nominally (P_z, P_{zz}) = (0,0), (-2/3,0), (2/3,0), (-2/3,0) and (-1/2,1/2), delivered by the polarized ion source POLIS [110]. The actual polarizations were slightly different and are represented in table 6.3.

Table 6.3: Polarization values for each of the spin polarized states.

State	p_z	p_{zz}
(-2/3,0)	-0.5573±0.0001	0.0106±0.0001
(2/3,0)	0.5408±0.0001	0.1760±0.0003
(0,-2)	-0.0206±0.0001	-1.3932±0.0002
(-1/2,1/2)	0.3862±0.0001	-0.1481±0.0003

To study the effect of systematic effects affecting the polarimetry performance three different perturbations were introduced to the measurements: transversal displacements of the beam and target, rotation of the beam and a combination of both. These perturbations were introduced using several magnets combinations upstream of the IBP (see Appendix 2).

- Magnet B3 situated immediately before the IBP at the intersection between the L and the M beamlines enables manipulations of the beam in the horizontal plane.
- Magnet BHOR was used for vertical bending.
- Magnet B5 was used to bring the beam to the right position due to a difference in heights of the two consecutive rooms.
- Magnet BUP situated immediately after the wall, enables horizontal bending.

- Magnet B2, together with B1, was used for manipulations of the beam in order to study rotation effects.

The beamline was carefully tuned to yield a waist at the location of the IBP. For this the beam profile monitors (harps) along the beamline were used. These harps were also used to calibrate the beam shifts and rotations and to monitor the beam emittance.

6.4.1.2 Procedure to Displace and Rotate the Beam

The procedure to measure the effect of a displacement was:

- Optimize count rate at the ribbon target for optimal settings (non- displaced and non-rotated beam) by slowly moving the beam onto the target until a maximum count rate was detected.
- Move the ribbon target to a specific displaced position.
- Steer the beam with B2 and B3 in a fixed combination so that the target is found and the count rate is again optimized.

In this way the displacement is determined by the position of the ribbon target which is known to 30 μm. The range of movement was -6 to 6 mm.
To study beam rotation effects a different procedure was performed:

- Change the position of the target with the target wheel procedure
- Move the beam so that it finds the target at optimal count rate (until now same as for displacements)
- Move the target back to original position
- Manipulating B1 and B2 find the target once more.

The distance between the B3 magnet (3.7 m upstream of the IBP) together with the displacement of the ribbon determine the beam angle at the target. Because of the layout of the beamline, rotation angles were limited to a range between -2 and 2 mrad.

6.4.2 Results

The data taken at KVI in 2007 were the result of a very well calibrated beam misalignment application. Deliberate changes were introduced to the beam position enabling the correlation between the observed effects with a shift of the scattering vertex. The left-right asymmetry was calculated.

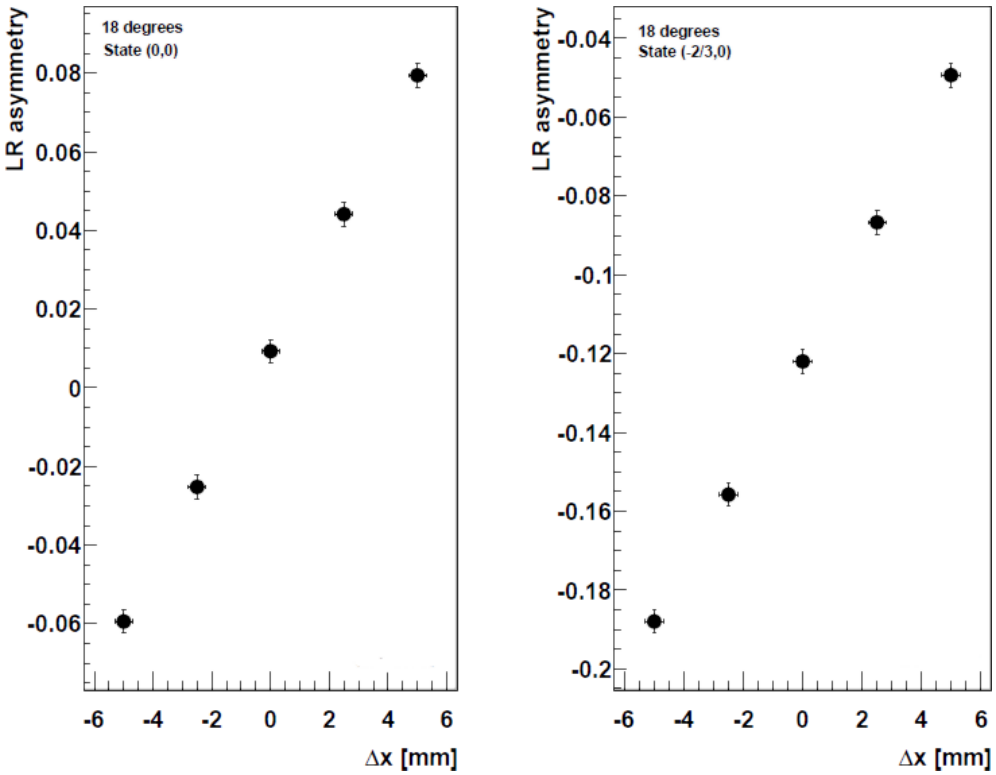

Figure 6.5: Left right asymmetry for the IBP 2007 measurements at the KVI for θ =18°. Deliberate displacements were inflicted on the beam and the effect measured. Here the data for unpolarized beam and state (-2/3,0) are presented. The error bars were multiplied by 100 to be visible in the plot.

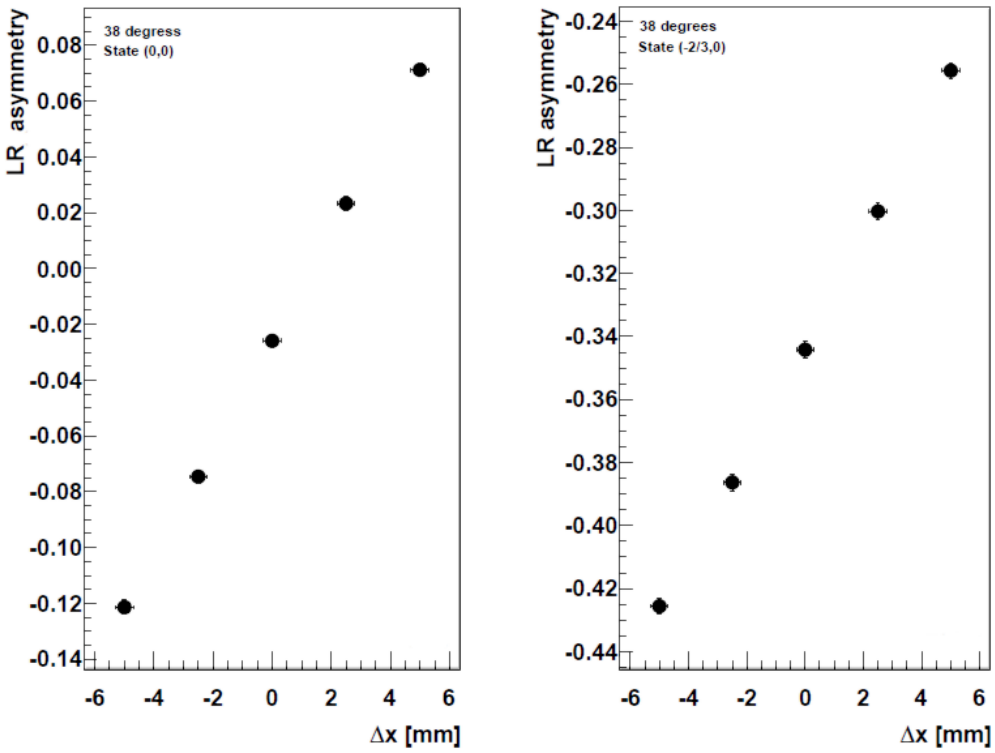

Figure 6.6: Left right asymmetry for the IBP 2007 measurements at the KVI for θ =38°. Deliberate displacements were inflicted on the beam and the effect measured. Here the data for unpolarized beam and state (-2/3,0) are presented. The error bars were multiplied by 100 to be visible in the plot.

Comparing the results in figures 6.5 and 6.6 with the analytical model expectation, it is verified that for a left-right, single-state asymmetry the dominant term is linear in $\frac{x}{R}$ as expected . The results, presented in table 6.4 [111] are the same to within about 1% independent of being determined from the unpolarized state or the two vector polarized states. As the asymmetry grows, the effect of a beam

Table 6.4: Derivatives of the cross section estimated from the data and from a scattering model [99].

Angle [°]	$\frac{\sigma'}{\sigma}$data	$\frac{\sigma'}{\sigma}$model
18	0.1158	0.1051
28	0.2050	0.2082
38	0.1630	0.1239
48	0.0998	0.0775

shift variation gets smaller as $1-{\mathcal{A}_{LR}}^2$. This effect starts to be visible already at 38°. The derivative of these slopes are presented in the second column of table 6.4 and have been calculated using a phenomenological elastic scattering model [111] similar to the one introduced in chapter 4. Such a treatment did not take into account the imposition of an additional hardware threshold on the events that would be allowed to get to the scalers, which would lower these estimates. For this reason, the threshold was adjusted empirically to see if fitting the prediction to the data was possible.

At 28°,the data and the prediction were close enough not to require further adjustment of the energy threshold. Both 38° and 48° were given a 17 and 9 MeV threshold respectively, with the results on the slope given in the last column. For 18°, the slope was rather insensitive to the choice of threshold.

Having verified the linear dependence of $\mathcal{A}_{LR}$ the cross ratio method was also applied. The left-right cross ratio ε_{LR} was evaluated by combining data for the (2/3,0) and (-2/3,0) polarized states. In figures 6.7 and 6.8 the results for 18° and 28° are shown. The dependence of ε_{LR} on Δx was fitted with an expression of the form

$$\varepsilon_{LR} = A + B\Delta x + C\Delta x^2. \tag{6.58}$$

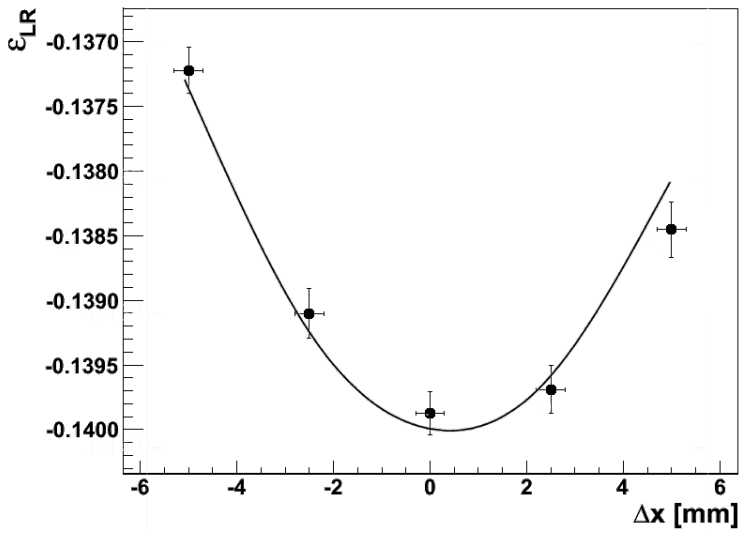

Figure 6.7: Cross Ratio asymmetry for the IBP 2007 measurements at the KVI for 18°. Deliberate displacements were inflicted on the beam and the effect measured. The solid curve shows the model prediction.

From these results, the values for the asymmetry A and its derivatives A'/A and A''/A can be determined using equation 6.49 and the relation between x/R and θ given in equation 6.43. The same parameters were also predicted using the scattering model introduced in chapter 4. The various predictions are presented in table 6.5.

Table 6.5: Predictions of the values for A'/A and A"/A obtained from a fit to the data and from the scattering model introduced in chapter 4.

Angle [°]	A'/Amodel	A'/Adata	A''/Amodel	A''/Adata
18	0.2514	0.25371(2)	0.0486	−0.018142(8)
28	0.0843	0.06084(1)	0.0139	0.001492(4)
38	0.0239	−0.00887(3)	0.0093	−0.00214(1)
48	0.0085	−0.00031(3)	0.0037	0.004827(9)

The shift in the minimum of ε_{LR} visible in figure 6.7 comes from the $u\theta$ term

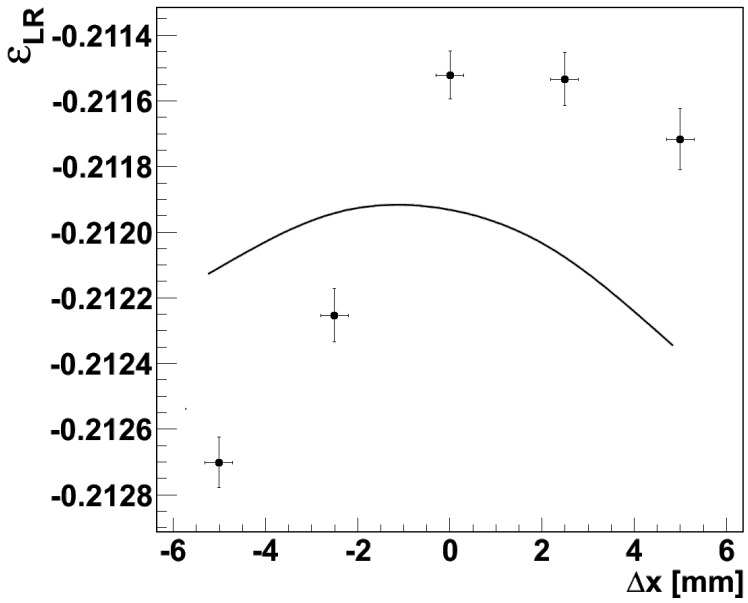

Figure 6.8: Cross Ratio asymmetry for the IBP 2007 measurements at the KVI for 28°. Deliberate displacements were inflicted on the beam and the effect measured. The solid curve shows the model prediction.

and the curvature from the θ^2 term. For each case, the average asymmetry was adjusted to best reproduce the data. Both the linear dependence on Δx of $\mathcal{A}_{LR}$ and the quadratic dependence of ε_{LR} could be predicted quantitatively to within 10%. As previously mentioned, the development of the dEDM polarimeter focuses on identifying these effects and establish a correction method to eliminate them or reduce them as much as possible. The use of the cross-ratio method strongly reduces the sensitivity to shifts/rotations of the scattering vertex. To reduce the sensitivity of systematic effects even more an independent measure of their strength is crucial. The ζ parameter introduced in equation 6.15 was calculated for the 2007 KVI data. The result for a scattering angle of 18 ° is shown in figure 6.9.

A clear correlation between the horizontal displacement of the beam and the zeta-parameter is visible. The zeta parameter can thus be used as a measure of the displacement. This is of particular interest in the final dEDM experiment

because knowing the precise beam location with sufficient precision will not be possible by other means. Instead the correlation between $\mathcal{A}_{LR}$, ε_{LR} and ζ can be used. An example of this is shown in figure 6.10. In practice, a set of relations

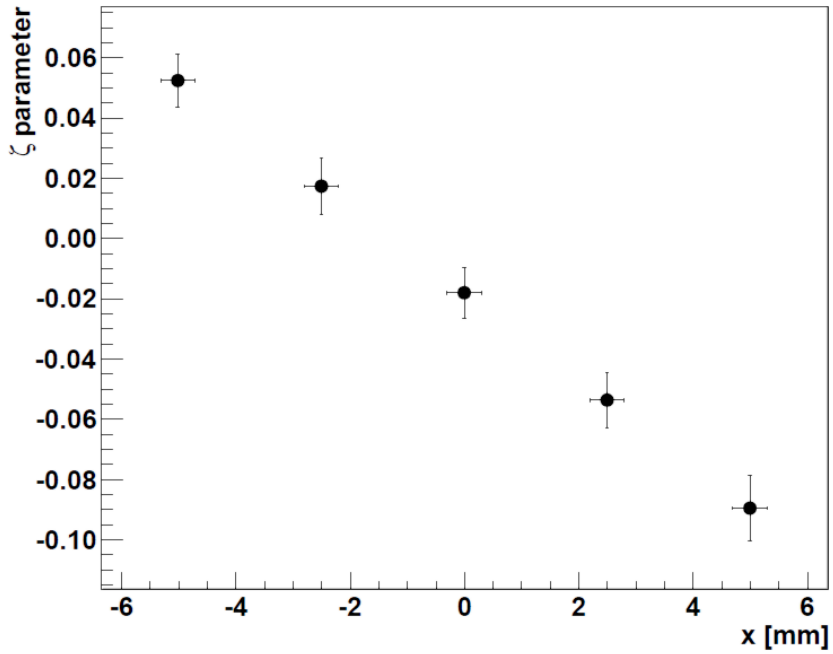

Figure 6.9: Error-parameter ζ for the IBP 2007 measurements at the KVI for θ =18°. Deliberate displacements were inflicted on the beam and the effect measured.

between ε_{LR} and ζ measured for this or the EDM polarimeter could be used in real time with the index ζ to calculate a correction to the measured cross ratio. This could take out such systematic effects, even if the dependence on ζ is higher than second-order.

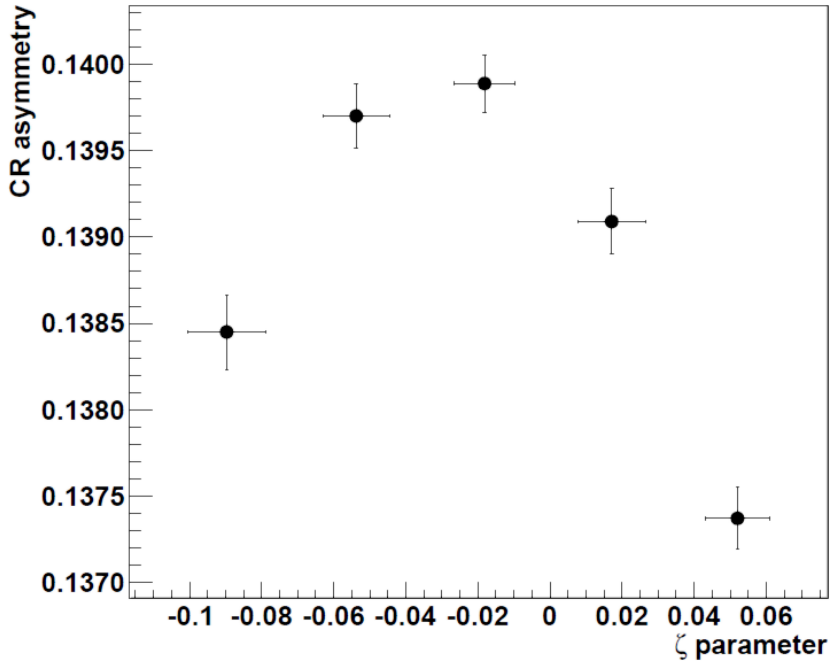

Figure 6.10: Cross Ratio versus ζ-parameter for the IBP 2007 measurements at the KVI for θ =18°. Deliberate displacements were inflicted on the beam and the effect measured. The error bars are multiplied by a factor 10 to be visible.

6.5 Experimental Studies at COSY

Also in the experiments at COSY the sensitivity for beam positions shifts and beam rotation was investigated. The equilibrium orbit of the beam at the EDDA location was modified by a combination of four dipole magnets. In this way the position and rotation of the beam could be set independently. The position and angle shifts where calibrated using beam position monitors (BPMs). The BPMs have a relative position uncertainty of 0.1 mm and an absolute position uncertainty of approximately 0.5 mm.
In all cases the square carbon aperture was used. The beam was extracted either on the horizontal or vertical edge by applying the appropriate noise. Systematic effect studies were hampered by an instability in the beam polarization which originated from an instability at the source. The effect from fluctuations in the polarization of the beam were larger than the expected effects in ϵ_{LR}. Therefore only results for A_{LR} are shown.

6.5.1 The role of Betatron Oscillations

A first observation involves the role of betatron oscillations. Beam particles exhibit betatron oscillations about the equilibrium orbit. For a system where no heating mechanism is imposed, the amplitude of these oscillations are limited by the acceptance of the carbon target. The *maximum* amplitude of the beam is given by the *minimum* distance between the beam equilibrium position and either the left and right edge of the target or the top and bottom edge for horizontal or vertical extraction, respectively. If the equilibrium orbit is displaced from the center of the target to either side the maximum betatron amplitude will in both cases be reduced.
When a heating mechanism is imposed on the beam, the average amplitude of the betatron oscillation about the equilibrium orbit grows slowly. The displacement of a particle at the location of the target as a function of time t is then given by

$$x(t) = x_\Delta + (A_0 + \Delta A(t)) \sin \omega t \tag{6.59}$$

with x_Δ the displacement of the equilibrium orbit, A_0 the initial betatron amplitude, $\Delta A(t)$ the time dependent change in the betatron amplitude and ω the

betatron oscillation frequency. The involved quantities still need to fulfill the requirement

$$|x_\Delta| + |A_0| + |\Delta A(t)| < D/2 \tag{6.60}$$

with D the distance between the two edges. This means that for a displacement x_Δ, the maximum betatron amplitude is given by

$$A_0 + \Delta A(t) < D - |x_\Delta|. \tag{6.61}$$

For a fixed x_Δ the particle will always be extracted on the side closest to the equilibrium orbit of the beam and never make it to the other side of the target. If the equilibrium orbit is the same for all beam particles they are always extracted on the target edge closest to the beam center. As a consequence the position of the scattering vertex will show a discontinuity when sweeping the beam from one side of the aperture to the other. If the equilibrium orbit exhibits dispersion or chromaticity or non-linear effects in the betatron motion this discontinuity will smooth out. An illustration of this effect is shown in figure 6.11 where the ζ parameter is plotted against the beam displacement. A horizontal scan of the beam was performed with horizontal white noise extraction. It can been seen that the extraction starts on one of the sides and then gradually shifts towards the other side. A more pronounced step is visible for vertical displacements when extracting the beam on the top or bottom of the target (see figure 6.11). The slope of ζ with respect to Δx is maximal for $\Delta x = 0$. Centering the beam with respect to a double sided target thus maximizes the sensitivity to beam displacements. To eliminate this sensitivity a single sided target should be used or the beam should be centered considerably closer to one side than to the other.

6.5.2 Sensitivity of $\mathcal{A}_{LR}$ to Beam Shifts and Rotations

In figure 6.12 the vector asymmetry $\mathcal{A}_{LR}$ and the tensor asymmetry $\mathcal{A}_T$ are shown for eight different beam displacements ranging from -4 to +4 mm. Each entry corresponds to a single measurement of 100 ms. The five different polarization states of the beam are clearly recognizable. These states were calibrated using the low energy polarimeter. The observed pattern persists independent of the displacement of the beam. For these measurements the beam was extracted on

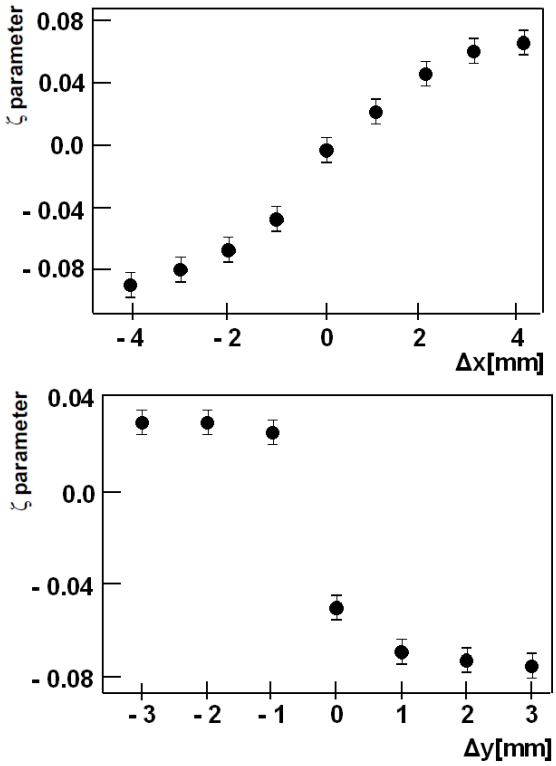

Figure 6.11: Error parameter ζ as a function of horizontal (top panel) and vertical (bottom) beam displacements. Horizontal (top panel) and vertical (bottom panel) white noise was applied to extract the beam.

the top and bottom edge of the target by applying vertical white noise. For each fill of COSY the polarization state is known so that the corresponding vector asymmetry can be calculated. In figure 6.13 a summary of the vector asymmetry $\mathcal{A}_{LR}$ is shown for each of the five polarization states for a beam displacement of -4 and +4 mm and five beam angles ranging from -5 to +5 mrad. In particular for the V^+ and T^+ states large deviations from an otherwise smooth trend are visible. These are caused by the instability of the source. A predominantly linear dependence of $\mathcal{A}_{LR}$ on the beam angle is visible. This dependence is similar for all five polarization states (see Appendix 3). This confirms the model prediction that the systematic effect is mainly driven by the derivative of the cross section.

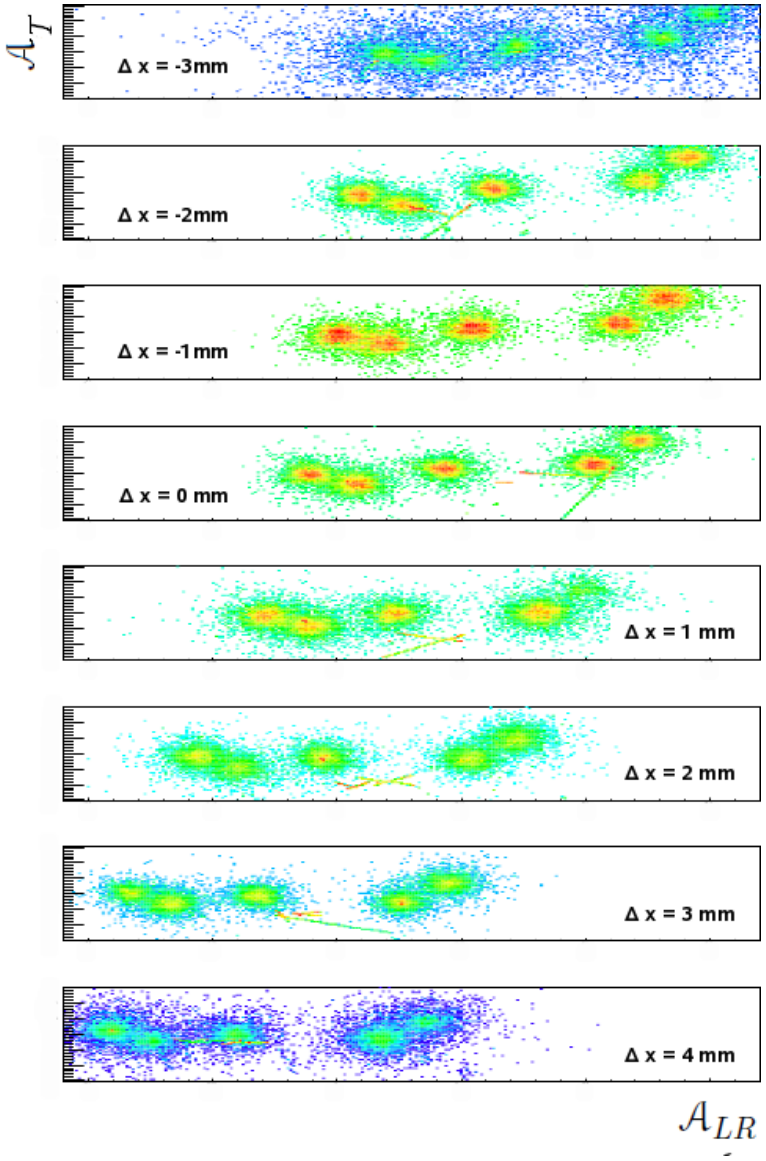

Figure 6.12: Each individual plot shows the distribution of measured vector and tensor asymmetries for 100 ms long measurements. The five spin states used in the experiments are visible as colored blobs. Each blob corresponds to one spin state (p_z, p_{zz}). From left to right: tensor plus (1,-1), vector minus (-2/3,0), unpolarized (0,0), tensor minus (1/2,-1/2) and vector plus (2/3,0). From top to bottom the beam was displaced horizontally by -3, -2, -1, 0, 1, 2, 3 and 4 mm. For different beam offsets a visible difference in vector asymmetry occurs, whereas the tensor one remains unchanged.

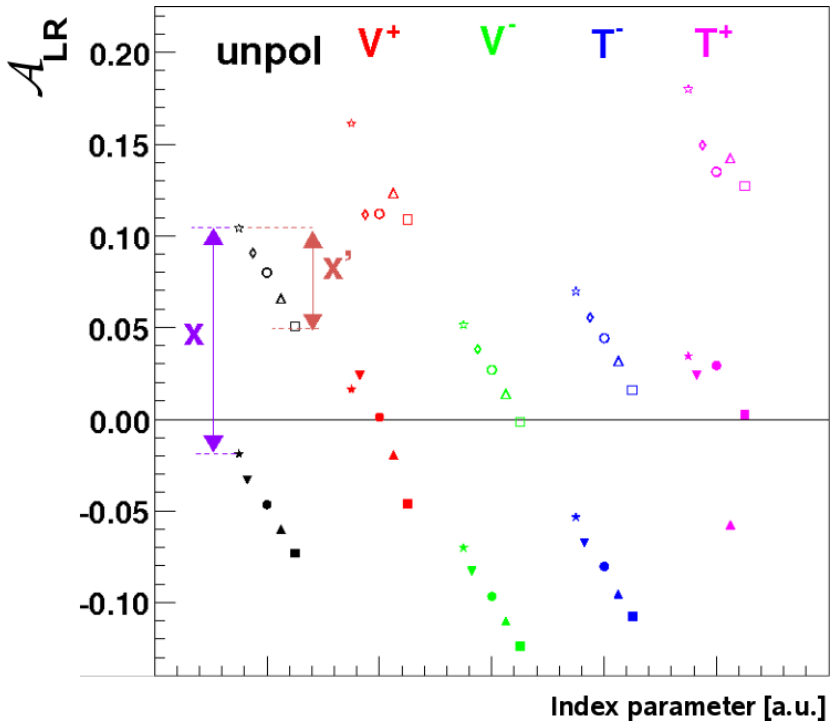

Figure 6.13: Left-right asymmetry for the different polarization states for both displacements and rotations. Open and closed symbols represent horizontal displacements for extraction on the right side of the target (closed) and right side of the target (opened). The different symbols represent different rotations between -5 (star) and 5 mrad (square). The index parameter represents different sets of measurements.

6.6 Results on the Selectivity Studies

The selectivity of the polarimeter, or in other words, its resistance against systematic effects was addressed. Traditionally the asymmetry in the counting rates observed in two detectors placed to the left and the right of the beam $\mathcal{A}_{LR}$ constitutes the signal for the vector polarization of the beam. Of particular interest is the resistance against variations of the position of the scattering vertex. Studies in which the location of the scattering target was systematically displaced have shown that this asymmetry has a predominantly linear dependence on displacements of the scattering vertex.
An improvement to the left-right counting rate asymmetry $\mathcal{A}_{LR}$ is the Cross Ratio method. In this method the rates for the left and right detectors are combined for two oppositely (vector-)polarized beams to form the cross ratio ϵ_{LR}. Its robustness lies in the fact that it eliminates the dependence on solid angle and luminosity and that the first order dependence on many other systematic effects are canceled. Measurements performed at KVI confirmed the expected presence of a quadratic dependence of ϵ_{LR} on scattering vertex displacements.
An improved analysis strategy was formulated by introducing the ζ-parameter. It combines the same data used for ϵ_{LR} such that it has little sensitivity to beam polarization while amplifying its sensitivity to beam perturbations. This parameter thus provides an independent measure of such perturbations. After calibration it can be used to correct systematic effects.
An analytical model was developed that parameterizes the left-right asymmetry $\mathcal{A}_{LR}$, the cross ratio ϵ_{LR} and the ζ-parameter as functions of scattering vertex displacements or rotations. This model predicts that systematic effects in $\mathcal{A}_{LR}$ are mainly determined by the θ-derivative of the cross section, whereas ϵ_{LR} is mainly determined by the θ-derivative of the analyzing power.
For quantitative predictions the scattering cross section and analyzing power are needed. For the studies performed at KVI such data were available. Using these data the observed results for ϵ_{LR} could be confirmed to within 10%. Similar studies were performed at COSY. For the energy used at COSY the scattering cross section and analyzing power are not sufficiently well known to make detailed predictions. The effects seen at KVI were therefore only qualitatively confirmed in

a storage ring environment. These studies also showed that the centroid position of the beam is not sufficient to describe the observed systematic shift in ϵ_{LR}. Also the motion about the equilibrium orbit must be taken into account.

Chapter 7

Conclusion and Outlook

The search for a permanent Electric Dipole Moment (EDM) on the deuteron provides an unique way to investigate new sources of CP and, assuming CPT symmetry, T violation. In particular the role of possible CP violating nucleon-nucleon interactions can be probed. In the framework of certain models beyond the Standard Model the deuteron might be more sensitive than the neutron [56]. The proposal to search for an EDM on the deuteron at a level of 10^{-29} e.cm using an electro-magnetic storage ring was brought forward by the deuteron EDM Storage Ring Collaboration. Such an experiment relies on the interaction between the EDM of the deuteron and the radial motional electric field a relativistic particle experiences in a magnetic field. Such fields can be up to a thousand times higher than those reachable in a laboratory with standard high voltage (high electric field) techniques. This interaction causes an additional precession around the radius vector of the orbital plane. This additional precession is an unique signal of an non-zero EDM. It can be measured by continuously monitoring the polarization of the stored particles and identifying a change in its vertical component.

The precision with which this change can be detected determines the sensitivity to an EDM. A highly efficient polarimeter capable of identifying a change in polarization at the level of 10^{-7} means the possibility of detecting an EDM on the deuteron at the level of 10^{-29} e.cm.

The suitability of a proposed deuteron EDM polarimeter concept was investigated through simulation studies and exploratory experiments. This concept is based

on spin dependent nuclear scattering. It consists of three distinct functional components:

- A **slow extraction mechanism** to direct the particles to a polarization analyzing target,
- a **thick analyzer target** in which polarization dependent nuclear scattering takes place, and
- a **position/angle sensitive detector** of the scattered particles.

The best suited slow extraction method identified is through beam emittance growth. Two approaches were explored: extraction via gas interaction and stochastic slow extraction. For the exploratory studies discussed here, the latter proved to be better due to the insufficient target density available for extraction via gas interaction. The target material of choice was identified to be ^{12}C. The selection of the right target thickness requires a detailed a scattering model. Therefore, a data-driven deuteron-induced scattering model was constructed. A reliable model requires data for a wide range of energies, scattering angles and a variety of deuteron-induced reactions. In the literature many high quality data sets are available for deuteron on carbon elastic scattering. Precise data for other reactions in the energy range of interest were not available. This was addressed by gathering new cross section and analyzing power data in particular for inelastic and deuteron breakup reactions. To improve the predictive power of the model, more data over a wider energy range are desirable. Based on this model and a figure of merit, defined as the statistical sensitivity per extracted particle, the performance of the system was studied and optimized as a function of target and detector geometry. Significant improvement in the performance over typical polarimeters in storage ring environments has been predicted. For the optimal configuration the figure-of-merit is 3 to 4 orders larger than then for the typical polarimeters.
The EDDA detector at COSY closely resembles the envisioned dEDM polarimeter. Therefore the feasibility of using such a setup as the dEDM polarimeter was studied experimentally. It was shown that the key features of this concept (slow extraction, thick target and an integrating detector system) led to a highly

efficient device. Quantitatively , the performance of the polarimeter matched the predictions from model simulations within one order of magnitude. Efficiency, figure-of-merit and analyzing power were determined for two different setup configurations with respect to the energy of the detected particles:

- A low threshold configuration yielded high detection efficiencies $\eta = 1.5 \times 10^{-2}$, low analyzing powers $A_y = 0.048$ and a figure-of-merit of 4.6×10^{-6}.
- A high threshold configuration yielded low detection efficiencies $\eta = 10^{-3}$, large analyzing powers $A_y = 0.22$ and a figure-of-merit of 4.8×10^{-6}.

The similar figures-of-merit indicate that the reachable statistical precision is equivalent. The lower efficiency and corresponding lower rates for the high energy threshold enables a simpler data acquisition system. The larger analyzing powers reduce the sensitivity to systematic effects.
Several sources of systematic effects have been investigated. An analytical model parameterizing the effects of beam displacements and rotations was created. This model describes the change in three experimental asymmetries:

- The **left-right asymmetry** $\mathcal{A}_{LR}$ of the number of detected particles in the left and right detectors.
- The **Cross Ratio** ε_{LR}: a polarization sensitive asymmetry calculated from the number of particles in the left and right detectors for two beams with opposite vector polarization.
- **The Zeta parameter** ζ: a polarization insensitive asymmetry calculated from the number of particles in the left and right detectors for two beams with opposite vector polarization.

The model predictions indicate a large first order sensitivity of $\mathcal{A}_{LR}$ on beam displacements and rotations. The magnitude of this is mainly affected by the derivative of the cross section with respect to the scattering angle.
The sensitivity of ε_{LR} was found to be second order in beam displacements and rotations. In this case, the magnitude of the sensitivity is mainly affected by the derivative of the analyzing power with respect to the scattering angle, without compromising the sensitivity to the polarization, compared to $\mathcal{A}_{LR}$.

The opposite is true for the ζ parameter. It has a large first order dependence on beam displacements and rotations. Its magnitude is mainly affected by the derivative of the cross section with respect to the scattering angle. Its sensitivity to the polarization is absent to first order. This parameter provides an independent measure of the beam perturbations and can thus be used to further improve the robustness against systematic effects. In this work these effects were also studied experimentally. The behavior and magnitude of $\mathcal{A}_{LR}$, ε_{LR} and ζ have been confirmed.

This work demonstrated the ability to predict the sensitivity to polarization and systematic effects and warrants further development of this concept for final use in the dEDM experiment. It shows that with existing beams and polarimetry concepts a deuteron EDM experiment at the level of 10^{-29} e.cm is feasible and realistic. At this level of sensitivity stringent bounds on new Physics can be set or new Physics can be found. Based on the success of the preparatory studies for a deuteron EDM experiment the German Research Institute in Jülich is considering to host and set up a definitive experiment [112].

Further refinements beyond the work reported here are in progress. The goal is to arrive at an even more optimized and efficient experimental configuration. This includes the construction of an analytical model including both rate and geometry induced effects. The need for a more complete model was motivated by rate effects observed during subsequent experiments at COSY (not contained in this thesis). The analysis of already taken data is underway to verify the ability to detected signals within one order of magnitude of the projected dEDM signal. A potential experiment to search for a proton EDM has emerged in the course of the work presented here. All the studies presented in this thesis are qualitatively valid also for the proton. The polarimeter is one of the key elements of any modern and sensitive EDM experiment. The investigated concept was proven to posses the desired high efficiency and robustness against the dominant systematic effects. This evens the road to a highly precise EDM search on the proton and the deuteron with even higher sensitivity to new Physics and with expected high significance of future model building beyond the Standard Model.

Appendix A

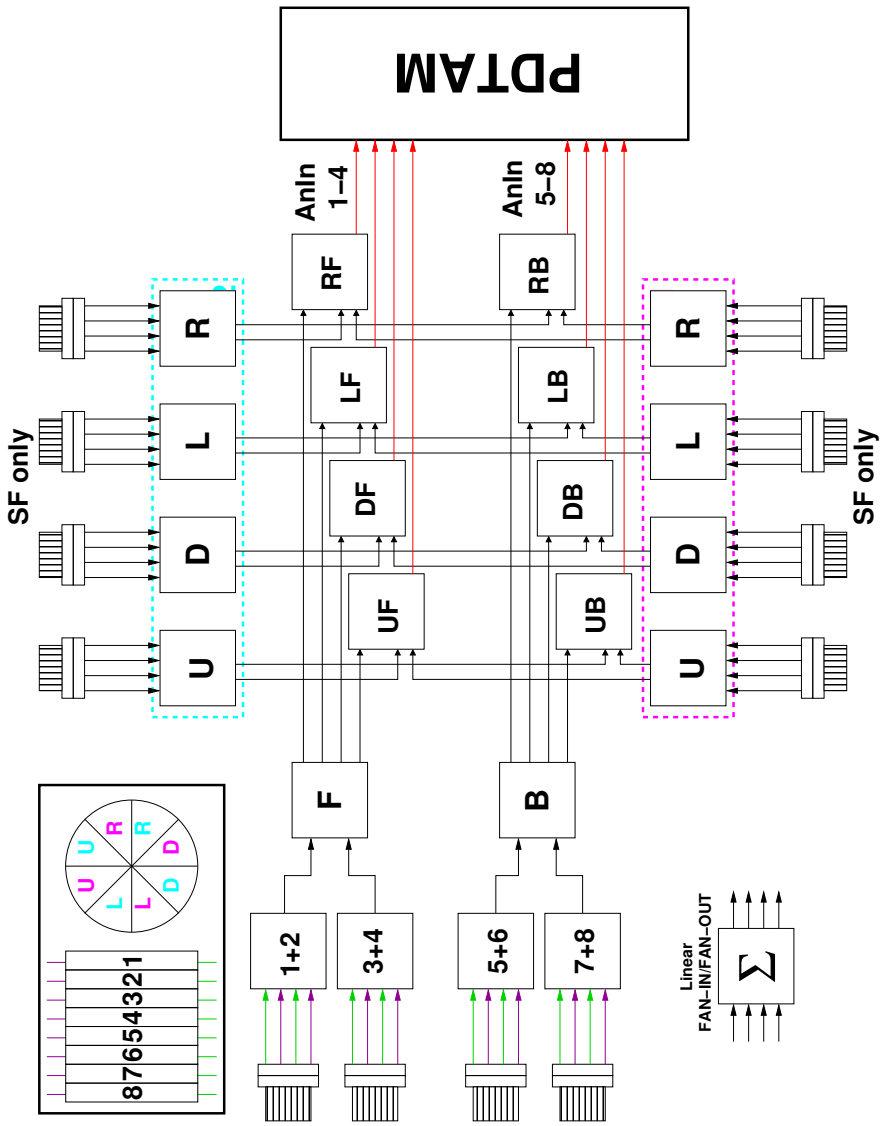

Figure A.1: Cabling scheme for the analog part of the data acquisition system used for the high threshold mesurement. The lables F and B represent the front and back rings, respectively. U, D, L and R represent the up, down, left and right detector sections given by the bar detectors. The PDTAM is a Programmable Discriminator/Trigger/Amplifier Module.

Appendix B

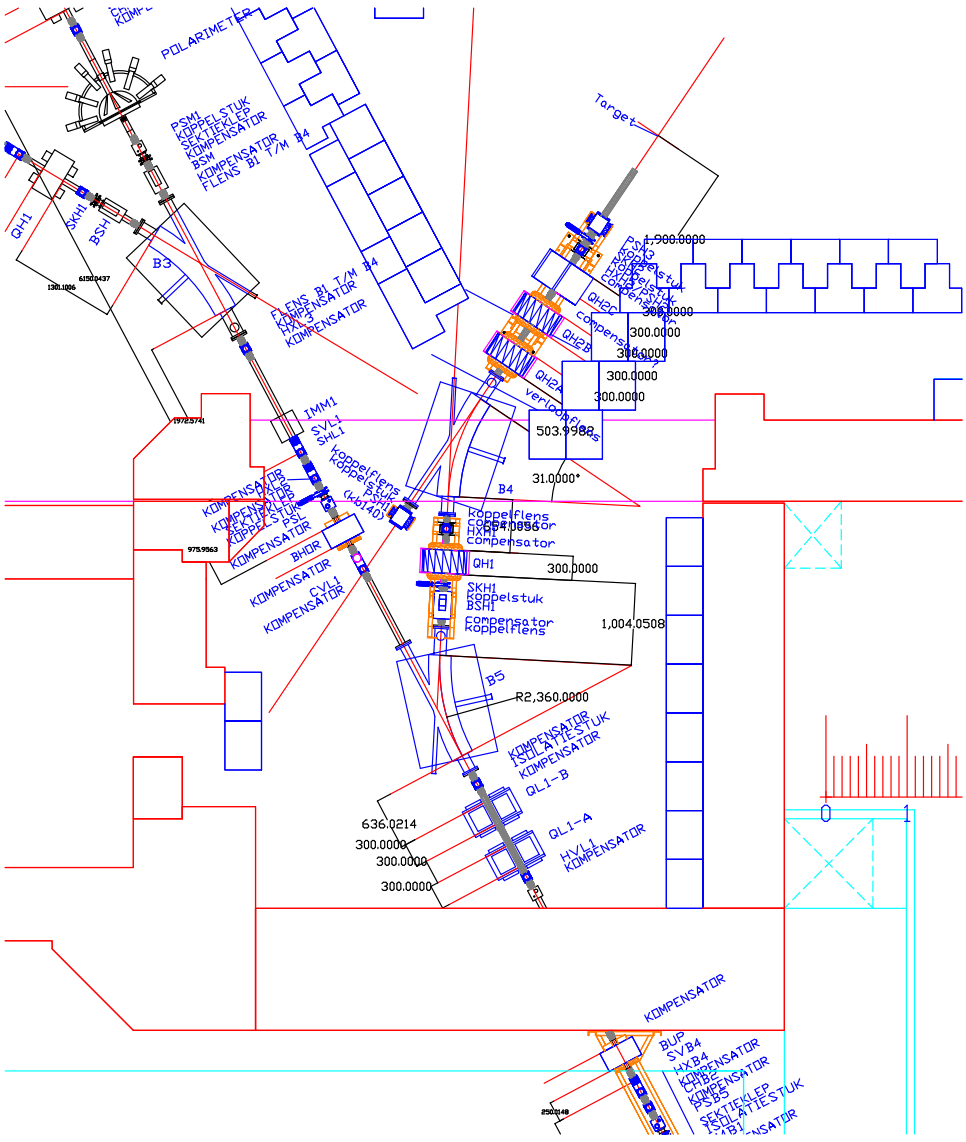

Figure B.1: Layout of the IBP beamline and all magets that were used to induce systematic effects.

Appendix C

Δx[mm]	$\Delta x'$[mm]	State (-2/3,0)	State (2/3,0)
-4	0	0.0947 ± 0.0039	0.0079 ± 0.0027
-2	0	0.0921 ± 0.0068	-0.0016 ± 0.0025
2	0	0.0872 ± 0.0023	-0.0200 ± 0.0046
4	0	0.0629 ± 0.0072	-0.0307 ± 0.0028

Δx[mm]	$\Delta x'$[mm]	State (-1,1)	State (1/2,1/2)	State (0,0)
-4	0	0.0253 ± 0.0017	0.0822 ± 0.0052	0.0615 ± 0.0043
-2	0	0.0164 ± 0.0024	0.0770 ± 0.0068	0.0516 ± 0.0064
2	0	-0.0028 ± -0.0026	0.0788 ± 0.0034	0.0331 ± 0.0003
4	0	-0.0127 ± 0.0030	0.0842 ± 0.0094	0.0231 ± 0.0056

Δx[mm]	$\Delta x'$[mm]	State (-2/3,0)	State (2/3,0)
0	-4	0.1229 ± 0.0119	0.0191 ± 0.0065
0	-1	0.1044 ± 0.0080	0.0010 ± 0.0017
0	-2	0.1230 ± 0.0087	0.0090 ± 0.0029
0	1	0.0698 ± 0.0047	-0.0286 ± -0.0007
0	4	0.0127 ± 0.0042	-0.0834 ± -0.0080

Δx[mm]	$\Delta x'$[mm]	State (-1,1)	State (1/2,1/2)	State (0,0)
0	-4	0.0367 ± 0.0073	0.1348 ± 0.0129	0.0726 ± 0.0094
0	-1	0.0195 ± 0.0023	0.1322 ± 0.0091	0.0547 ± 0.0041
0	-2	0.0272 ± 0.0045	0.1410 ± 0.0115	0.0631 ± 0.0063
0	1	-0.0116 ± 0.0003	0.1006 ± 0.0067	0.0238 ± 0.0025
0	4	-0.0662 ± -0.0083	0.0206 ± -0.0025	-0.0317 ± -0.0056

Figure C.1: Values for the left-right asymmetry$\mathcal{A}_{LR}$ for the different polarizations states for various beam displacements. Δx and $\Delta x'$ represent beam displacements and beam rotations, respectively.

Summary

The quest for new Physics constitutes one of the main endeavors in physics research. Searches for permanent Electric Dipole Moments (EDMs) in fundamental systems have a wide window to discover Physics beyond the Standard Model.

A proposal exists that promises a sensitivity to an EDM of the deuteron at a level of 10^{-29} e.cm. The experiment relies on the interaction between the EDM of the deuteron and the radial motional electric field a relativistic particle experiences in the field of a magnetic storage ring, which would cause the spin of the particle to precess. A non-zero EDM manifests itself by a change in the polarization component along the magnetic field. To monitor this signal, a novel highly efficient polarimeter concept has been investigated. In addition, this polarimeter must be robust against systematic errors and able to continuously monitor the beam polarization, guaranteeing optimal sensitivity.

Detailed studies on systematic error control were carried out at KVI, in addition to the measurement of cross sections and analyzing powers necessary for precise simulations. Measurements conducted at COSY-Jülich in Germany yielded the predicted high efficiencies. With these efficiencies and the developed understanding of systematic effects it was possible to track changes in polarization at the level of a few hundred parts-per-million. The developed polarimeter concept is appropriate for reaching the aimed sensitivity of a deuteron EDM experiment.

Samenvatting

De zoektocht naar nieuwe fysica is een van de belangrijkste inspanningen in natuurkundig onderzoek. Het zoeken naar permanente elektrische dipool momenten (EDMen) in fundamentele systemen opent een wijd venster om niet-Standaard Model fysica te ontdekken.

Er bestaat een voorstel om met een gevoeligheid van 10^{-29} e.cm naar een deuteron EDM te zoeken. Het experiment is gebaseerd op de interactie tussen het EDM en het radiële elektrisch veld dat een relativistisch deeltje ervaart in het veld van een magnetische opslagring. Deze interactie zou leiden tot precessie van de spin van het deeltje. Een EDM ongelijk nul manifesteert zich door een verandering in de polarisatie component langs het magnetisch veld. Voor het observeren van dit signaal is een nieuw concept voor een uiterst efficiënte polarimeter onderzocht. Naast efficient moet de polarimeter ook robuust zijn tegen systematische fouten en in staat om voortdurend de bundel polarisatie te observeren, zodat een optimale gevoeligheid bereikt wordt.

Uitvoerige studies naar de beheersing en correctie van systematische fouten werden uitgevoerd op het KVI, naast metingen van het analyzerend vermogen en de botsingsdoorsneden die noodzakelijk zijn voor nauwkeurige simulaties. Het voorspelde hoge rendement werd bevestigd in metingen uitgevoerd bij COSY-Jülich in Duitsland. Met deze efficiëntie en het ontwikkelde begrip van systematische effecten was het mogelijk om veranderingen in de polarisatie te volgen op het niveau van een paar honderd delen per miljoen. Het ontwikkelde polarimeter concept is geschikt voor het bereiken van de beoogde gevoeligheid van een deuteron EDM-experiment.

Acknowledgements

Throughout the last four years of development of this project several people were involved. I would like to acknowledge all of them and say thank you.

A special word to Klaus Jungman for his continuous support and enthusiasm. To all the people at KVI that have been part of this work my deepest appreciation for all your support and suggestions.

All the people at COSY, that have welcome us as part of their team and played an essential role in this project, you have made COSY feel like home everytime. Thank you very much. A particular word to Andreas Lehrach, Bernd Lorentz, Ralf Gebel, Olaf Felden, Hans Stockhorst and Dieter Prasuhn.

To everyone part of the Storage Ring EDM Collaboration a big big thank you. It was a pleasure to be part of your collaboration and to work with such wonderful people.

To Ed Stephenson, Yannis Semertzidis, Astrid Imig and Bill Morse my deepest gratitude. Your dedication and knowledge impelled us further and further.

For having accepted to act as members of my reading committee and for their valuable suggestions and comments a warm thank you to Prof. dr. O. Naviliat-Cuncic, Prof. dr. Y. Kuno and Prof. dr. B.L. Roberts.

A very special word to Prof. Joao Lima and Prof. Paulo Gali. Thank you for all your support and help. It would have not been possible without you. Obrigada!

To all the colleagues, lunch buddies and cinema mates, thanks. It would not have been the same without you.

To all of my friends (you know who you are :)) thanks for making it such a special time. You have made it unforgettable.

To Siva and Andrija, thanks so much guys!

Para a minha familia, muito muito obrigada por tudo! Voces estao por tras de tudo o que eu faco. Obrigada bixus!!

And my biggest thank you of all is to my supervisor Gerco Onderwater. You were the reason I came to KVI and the reason I stayed. Your full support and assistance made all this work possible. It was a huge pleasure to work with you. Not only you are an amazing researcher, you are a wonderful person. Thank you very very much!

References

[1] T. Aliev, N. K. Pak, and M. Serin, editors. *The Standard Model and Beyond, Proceedings of the Second International Summer School in High Energy Physics in Muğla, Turkey, in September 2006*. 2007. 1

[2] I. B. Khriplovich and S. K. Lamoreaux. *CP Violation Without Strangeness - Electric Dipoles Moments of Particles, Atoms, ans Molecules*. 1997. 1, 13, 17

[3] J. H. Christenson, J. W. Cronin, V. L. Fitch, and R. Turlay. Evidence for the 2π decay of the K2 Meson. *Physical Review Letters*, 13:138–140, 1964. 4, 5

[4] T. D. Lee and C. N. Yang. Question of Parity Conservation in Weak Interactions. *Physical Review*, 104:254, 1956. 5

[5] C. S. Wu, E. Ambler, R. W. Hayward, D. D. Hoppes, and R.P. Hudson. Experimental test of parity conservation in beta decay. *Physical Review*, 105:1413, 1957. 4, 5

[6] G. Luders. Proof of the TCP theorem. *Annals of Physics*, 2:1–15, 1957. 4

[7] J. Schwinger. The theory of quantized fields II. *Physical Review*, 91:713–728, Aug 1953. 4

[8] M. Pospelov and Ritz A. Electric dipole moments as probes of New Physics. *Annals of Physics*, 318:119–169, 2005. 4, 6

[9] M. Kobayashi and T. Maskawa. CP-Violation in the Renormalizable Theory of Weak Interaction. *Progress of Theoretical Physics*, 49:652, 1973. 5, 7

[10] J. E. Kim. Natural embedding of Peccei-Quinn symmetry in flavor grand unification. *Physical Review D*, 26(11):3221–3224, Dec 1982. 6

[11] B. Aubert et al. Observation of CP Violation in the B^0 Meson System. *Physical Review Letters*, 87:091801, 2001. 7

[12] K. Abe et al. Observation of Large CP Violation in the Neutral B Meson System. *Physical Review Letters*, 87:091801, 2001. 7

[13] A. D. Sakharov. Violation of CP Invariance, C Asymmetry, and Baryon Asymmetry of the Universe. *Pisma v Zhurnal Eksperimentalnoi i Teoreticheskoi Fiziki*, 5:32, 1967. 7

[14] K. Jungmann. *Private Communication*, 2006. 11

[15] R. Timmermans. EDMs in Atoms, Molecules, and Fundamental Particles. *9th Conference on the Intersections of Particle and Nuclear Physics*, 2006. 8

[16] C. A. Baker et al. An Improved Experimental Limit on the Electric Dipole Moment of the Neutron. *Physical Review Letters*, 97:131801, 2006. 12, 14

[17] W. C. Griffith et al. Improved limit on the permanent electric dipole moment of ^{199}Hg. *Physical Review Letters*, 102:101601, 2009. 12, 15, 18

[18] B. C. Regan et al. New Limit on the Electron Electric Dipole Moment. *Physical Review Letters*, 88:071805, 2002. 12

[19] E. M. Purcell and N. F. Ramsey. On the Possibility of Electric Dipole Moments for Elementary Particles and Nuclei. *Physical Review*, 78(6):807, Jun 1950. 13, 14

[20] J. H. Smith, E. M. Purcell, and N. F. Ramsey. Experimental Limit to the Electric Dipole Moment of the Neutron. *Physical Review*, 108:120–122, Oct 1957. 13

[21] Norman F. Ramsey. Experiments with Separated Oscillatory Fields and Hydrogen Masers. *Nobel Lectures, Physics 1981-1990*, 1993. 14

[22] I. Altarev et al. Towards a new measurement of the neutron electric dipole moment. *Nuclear Instruments and Methods in Physics Research Section A: Accelerators, Spectrometers, Detectors and Associated Equipment*, 611:133 – 136, 2009. 14

[23] K. Kirch for the UCN collaboration. An ultracold neutron facility at PSI. *International Nuclear Physics Conference*, 2001. 14

[24] T. M. Ito. Plans for a Neutron EDM Experiment at SNS. *Journal of Physics: Conference Series*, 012037, 2007. 14

[25] V. V. Flambaum and J. S. M. Ginges. Nuclear Schiff moment and time-invariance violation in atoms. *Phys. Rev. A*, 65:032113, 2002. 15

[26] P. G. H. Sandars. Measurability of the Proton Electric Dipole Moment. *Physical Review Letters*, 19:1396–1398, 1967. 16

[27] N. Auerbach, V. V. Flambaum, and V. Spevak. Collective T- and P-Odd Electromagnetic Moments in Nuclei with Octupole Deformations. *Physical Review Letters*, 76(23):4316–4319, 1996. 16

[28] P.D. Shidling et al. Production of short lived radioactive beams of radium. *Nuclear Instruments and Methods in Physics Research Section A: Accelerators, Spectrometers, Detectors and Associated Equipment*, 606(3):305 – 309, 2009. 16

[29] K. Jungmann. TRIμ P - a New Facility to Investigate Fundamental Interactions with Optically Trapped Radioactive Atoms. *Acta Physica Polonica B*, 33:2049, 2002.

[30] U. Dammalapati, S. De, K. Jungmann, and L. Willmann. Isotope shifts of $6s5d^3d$-$6s6p^1p_1$ transitions in neutral barium. *European Physical Journal D*, 53, 2009. 16

[31] P.G.H. Sandars. Enhancement factor for the electric dipole moment of the valence electron in an alkali atom. *Physics Letters*, 22:290, 1966. 16, 17

[32] J. S. M. Ginges and V. V. Flambaum. Violations of fundamental symmetries in atoms and tests of unification theories of elementary particles. *Physics Reports*, 397:63–154, 2004.

[33] P. G. H. Sandars. The electric dipole moment of an atom. *Physics Letters*, 14:192, 1965.

[34] Z. W. Liu and H. P. Kelly. Analysis of atomic electric dipole moment in thallium by all-order calculations in many-body perturbation theory. *Physical Review A*, 45:R4210–R4213, 1992. 16, 17

[35] B. C. Regan, Eugene D. Commins, Christian J. Schmidt, and David DeMille. New limit on the electron electric dipole moment. *Physical Review Letters*, 88:071805, 2002. 16

[36] J. J. Hudson, B. E. Sauer, M. R. Tarbutt, and E. A. Hinds. Measurement of the Electron Electric Dipole Moment Using YbF Molecules. *Physical Review Letters*, 89:023003, 2002. 17

[37] L. I. Schiff. Measurability of Nuclear Electric Dipole Moments. *Physical Review*, 132(5):2194–2200, 1963.

[38] D. et al. DeMille. Investigation of PbO as a system for measuring the electric dipole moment of the electron. *Physical Review A*, 61(5):052507, 2000. 17

[39] E. D. Commins, S. B. Ross, D. DeMille, and B. C. Regan. Improved experimental limit on the electric dipole moment of the electron. *Physical Review A*, 50:2960–2977, Oct 1994. 19

[40] G. W. et al. Bennett. Final report of the E821 muon anomalous magnetic moment measurement at BNL. *Physical Review D, year = 2006, volume = 73, pages = 072003.* 20

[41] G. W. et al. Bennett. Improved limit on the muon electric dipole moment. *Physical Review D*, 80(5):052008, 2009. 20

[42] E. D. Commins. Electric Dipole Moments of Elementary Particles, Nuclei, Atoms and Molecules. *Journal of the Physical Society of Japan*, 76:111010, 2007. 21

[43] K. S. Babu, S. M. Barr, and Ilja Dorsner. Scaling of lepton dipole moments with lepton mass. *Physical Review D*, 64:053009, 2001. 21

[44] K. S. Babu, B. Dutta, and R. N. Mohapatra. Enhanced electric dipole moment of the muon in the presence of large neutrino mixing. *Phys. Rev. Lett.*, 85(24):5064–5067, Dec 2000. doi: 10.1103/PhysRevLett.85.5064. 21

[45] A. Adelman and K.Kirch. Search for the muon electric dipole moment using a compact storage ring, 2006. 21

[46] J. D. Jackson. *Classical electrodynamics; 3rd ed.* Wiley, New York, NY, 1999. 22

[47] A. J. Silenko. Equation of spin motion in storage rings in the cylindrical coordinate system. *Physical Review Special Topics - Accelerators and Beams*, 9:034003, 2006. 22

[48] F. J. M. Farley et al. A new method of measuring electric dipole moments in storage rings. *Physical Review Letters*, 93:052001, 2004. 23

[49] Yuri F. Orlov, William M. Morse, and Yannis K. Semertzidis. Resonance Method of Electric-Dipole-Moment Measurements in Storage Rings. *Physical Review Letters*, 96:214802, 2006. 25

[50] R. M. Carey et al. The New (g-2) Experiment: A proposal to measure the muon anomalous magnetic moment to ±0.14 ppm precision. *FERMILAB-PROPOSAL-0989*. 26

[51] C.J.G. Onderwater. Edm of a positron. *Private Communication*, 2008. 26

[52] A. Adelmann, K. Kirch, C. J. G. Onderwater, and T. Schietinger. Compact storage ring to search for the muon electric dipole moment. 2006. URL `http://www.scientificcommons.org/21778708`. 26

[53] Y. K. Semertzidis for the EDM Collaboration. A New Method For A Sensitive Deuteron EDM Experiment. *Intersections of Particle and Nuclear Physcis: 8th Conference CIPANP2003*, 698:200–204, 2004. 26

[54] URL `http://www3.bnl.gov/muonedm/Deuteron_EDM/Proton_RD/`. 26

[55] I. B. Khriplovich. Feasibility of search for nuclear electric dipole moments at ion storage rings. *Physics Letters B*, 444:98 – 102, 1998. 26

[56] C. P. Liu and R. G. E. Timmermans. P and T odd two-nucleon interaction and the electric dipole moment. *Physical Review*, C70:055501, 2004. 26, 27, 28, 155

[57] I. B. Khriplovich and R. V. Korkin. P and T odd electromagnetic moments of deuteron in chiral limit. *Nuclear Physics A*, 665:365–373, 2000. 26

[58] O. Lebedev, K. A. Olive, M. Pospelov, and A. Ritz. Probing CP violation with the deuteron electric dipole moment. *Physical Review D*, 70:016003, 2004. 26, 27, 28

[59] M. Pospelov and A. Ritz. Theta-Induced Electric Dipole Moment of the Neutron via QCD Sum Rules. *Physical Review Letters*, 83:2526–2529, 1999. 27

[60] dEDM collaboration. Search for a permanent electric dipole moment of the deuteron nucleus at the 10^{29} e.cm level. *AGS Proposal BNL*, 2008. 28, 29

[61] A. G. Drentje, H. R. Kremers, J. Mulder, and J. Sijbring. Ion sources at the kvi (abstract). *Review of Scientific Instruments*, 69:728–728, 1998. 29

[62] J. Alessi et al. Performance of a hight intensity polarized H^- source on the Brookhaven 200 MeV Linac. *LINAC Gyeingju*, 2002. 29

[63] dEDM Collaboration. AGS Proposal: Search for a permanent electric dipole moment of the deuteron nucleus at the 10^{-29} ecm level. URL `=http://www3.bnl.gov/muonedm/Deuteron_EDM/EDM_BNL_PRO/deuteron_proposal_080405_1.pdf`. 29

[64] B. Bonin et al. POMME: A medium energy deuteron polarimeter based on semi-inclusive α-carbon scattering. *Nuclear Instruments and Methods in Physics Research Section A*, 288:389–398, 1990. 29, 37, 40

[65] B. Khazin. *Private comunication*, 2005. 30

[66] G. G. Ohlsen. Polarization transfer and spin correlation experiments in nuclear physics. *Reports on Progress in Physics*, 35:717, 1972. 31, 32

[67] G. G. Ohlsen and P. W. Keaton, Jr. Techniques for measurement of spin-$\frac{1}{2}$ and spin-1 polarization tensors. *Nuclear Instruments and Methods*, 109:41, 1973. 33, 34

[68] K. A. et al. Gridnev. Deuteron ground state properties and low energy P-N scattering $^1S_0$ and $^3S_1^3D_1$ channels. *European Physical Journal A*, 6:21–27, 1999. 33

[69] K. Krane. *Introductory Nuclear Physics*. "John Wiley and Sons", 1988. 34

[70] D. T. Khoa, W. von Oertzen, H. G. Bohlen, and S. Ohkubo. Nuclear rainbow scattering and nucleus-nucleus potential. *Journal of Physics G: Nuclear and Particle Physics*, 34:R111–R164, 2007. 36

[71] H. Huang et al. A p-carbon cni polarimeter for rhic. *Particle Accelerator Conference New York*, 1999. 36

[72] N. et al. E. Cheung. Calibration of the polarimeter POMME at proton energies between 1.05 and 2.4 GeV. *Nuclear Instruments and Methods in Physics Research A*, 363:561–567, 1995. 37

[73] R. Bieber et al. Performance of the KVI in-beam polarimeter. *Nuclear Instruments and Methods in Physics Research*, A457:12–21, 2001. 38, 43, 69, 71, 135

[74] Mohammad Eslami-Kalantari. *Three nucleon force effects in proton-deuteron breakup studied with BINA at 135 MeV*. PhD thesis, Kernfysisch Versneller Instituut, 2009. 43

[75] H. Stockhorst. Polarized proton and deuteron beams at cosy, 2004. URL `http://www.citebase.org/abstract?id=oai:arXiv.org:physics/0411148`. 43

[76] V. S. et al. Morozov. Spin manipulating stored 1.85 GeV/c vector and tensor polarized spin-1 bosons. *Physical Review Special Topics - Accelerators and Beams*, 8:061001, 2005. 43

[77] A. Lehrach. Cosy facts sheet. *Private Communication*, 2007. 44

[78] E. J. Stephenson and C. J. G. Onderwater. Polarized deuteron beam and polarization measurement for the Storage Ring EDM search. *Private Communication.* 53

[79] G. et al. Luijckx. Polarized electrons in the AmPS storage ring. *APS Meeting Abstracts*, 1997. 48

[80] H.Stockhorst et al. Progress and Developments at the Cooler Synchrotron COSY. *EPAC*, 2002. 48, 49

[81] J. Dietrich et al. Beam Profile Measurements Based On Light Radiation of Atoms Excited by the Particle Beam. *Care Report- HIPPI*, 2007. 48

[82] C. et al. Ekstrom. Hydrogen pellet targets for circulating particle beams. *Nuclear Instruments and Methods in Physics Research A*, 371:572–574, 1996. 49, 50

[83] N. van Sen et al. Elastic scattering of polarised deuterons from 160 to 200, 400 and 700 mev. *Nuclear Physics A*, 464:717 – 739, 1987. 49

[84] W. Morse. Beam Dynamics and the Polarimeter Target. *Private Communication*, 2008. 49

[85] S. van der Meer. Stochastic Cooling and the accumulation of antiprotons. *Nobel Lectures, Physics 1981-1990*, 1984. 50

[86] Beam Extraction at the Cooler Synchrotron COSY. *Accelerator Conferences*, 2006. 50

[87] Beam tests of a stochastic slow extreaction system prototype in the U70. *RuPAC*, 2006. 50

[88] P.Brittner et al. The stochastic-cooling system of COSY. 51

[89] D. Babusci et al. Proposal for the dEDM polarimeter based on MRPC technology. *Private Communication*, 2008. 59, 101

[90] J. P. Robert G. Charpak Y. Giomataris, Ph. Rebourgeard. MICROMEGAS: high-granularity position-sensitive gaseous detector for high particle-flux environments. *Nuclear Instruments and Methods in Physics Research A*, 376:29–35, 1996. 59

[91] N. Matsuoka et al. Optical model and folding model potentials for elastic scattering of 56 MeV polarized deuterons. *Nuclear Physics A*, 455:413 – 433, 1986. 65, 66

[92] S. Kato et al. Analyzing power measurements for d-12C elastic scattering between 35-70 MeV. *Nuclear Instruments and Methods in Physics Research Section A: Accelerators, Spectrometers, Detectors and Associated Equipment*, 238:453 – 462, 1985. 68

[93] E. J. Stephenson. Private communication. 2007. 68

[94] T. et al. Kawabata. Isovector and isoscalar spin-flip $m1$ strengths in $b11$. *Physical Review C*, 70:034318, 2004. 68

[95] Y. Satou et al. Three-body dN interaction in the analysis of the 12C reaction at 270 MeV. *Physics Letters B*, 549:307 – 313, 2002. 68

[96] A. M. van den Berg. The Big-Bite spectrometer for AGOR. *Nuclear Instruments and Methods in Physics Research Section B: Beam Interactions with Materials and Atoms*, 99:637 – 640, 1995. 69

[97] D. et al. Ridikas. Inclusive proton production cross sections in (d, xp) reactions induced by 100 MeV deuterons. *Physical Review C*, 63:014610, 2000. 71

[98] K. Brantjes. Elastic scattering modeling for a deuteron edm polarimeter. *Master Thesis*, 2008. 76, 93

[99] E. J. Stephenson. Deuteron Induced Reactions Model. 2008. 83, 142

[100] M. Altmeier et al. A helical scintillating fiber hodoscope. *Nuclear Instruments and Methods in Physics Research Section A*, 431:428–436, 1999. 98

[101] T. Poelman. Programmable discriminator/trigger/amplifier module (pdtam). *PhD Thesis*. 99

[102] F.Schwartz. Private communication. *Bachelor Thesis*, 2008. 100

[103] URL `http://root.cern.ch/`. 100

[104] V. Dzordzhadze. Monte carlo simulations for the edda target and detector system. *Private Communication*, 2008. 105

[105] M. Froissart and R. Stora. Depolarisation d'un faisceau de protons polarises dans un synchrotron. *Nuclear Instruments and Methods*, 7(3):297 – 305, 1960. 109

[106] V. S. Morozov et al. Experimental Verification of Predicted Beam-Polarization Oscillations near a Spin Resonance. *Physical Review Letters*, 100:054801, 2008. 109

[107] E. T. Akhmedov and D. Singleton. On the relation between Unruh and Sokolov-Ternov effects. *International Journal of Modern Physics A*, 22: 4797–4823, 2007. 125

[108] V. G. Baryshevsky and A. A. Gurinovich. Spin rotation and birefringence effect for a particle in a high energy storage ring and measurement of the real part of the coherent elastic zero-angle scattering amplitude, electric and magnetic polarizabilities, 2005. URL `oai:arXiv.org:hep-ph/0506135`. 127

[109] V. G. Baryshevsky. Spin rotation of polarized beams in high energy storage ring, 2006. URL `oai:arXiv.org:hep-ph/0603191`. 127

[110] H. R. Kremers and A. G. Drentje. Performance of the polarized ion source polis used at the agor accelerator facility. *The seventh international workshop on polarized gas targets and polarized beams*, 421(1):507–508, 1998. 137

[111] E. J. Stephenson and M.S. Silva. Analysis of the 2007 IBP data. *Private Communication*, 2007. 142

[112] Hans Ströher. Private communication, 2009. 158